UCRL 9390

UNIVERSITY OF CALIFORNIA

Ernest O. Lawrence

Radiation Laboratory

ELECTRON TRIPLET PRODUCTION BY HIGH-ENERGY PHOTONS IN HYDROGEN

TWO-WEEK LOAN COPY

This is a Library Circulating Copy which may be borrowed for two weeks. For a personal retention copy, call Tech. Info. Division, Ext. 5545

DISCLAIMER

This document was prepared as an account of work sponsored by the United States Government. While this document is believed to contain correct information, neither the United States Government nor any agency thereof, nor the Regents of the University of California, nor any of their employees, makes any warranty, express or implied, or assumes any legal responsibility for the accuracy, completeness, or usefulness of any information, apparatus, product, or process disclosed, or represents that its use would not infringe privately owned rights. Reference herein to any specific commercial product, process, or service by its trade name, trademark, manufacturer, or otherwise, does not necessarily constitute or imply its endorsement, recommendation, or favoring by the United States Government or any agency thereof, or the Regents of the University of California. The views and opinions of authors expressed herein do not necessarily state or reflect those of the United States Government or any agency thereof or the Regents of the University of California.

Printed in USA. Price $2.25. Available from the
Office of Technical Services
U. S. Department of Commerce
Washington 25, D.C.

ELECTRON TRIPLET PRODUCTION BY HIGH-ENERGY PHOTONS IN HYDROGEN

Contents

Abstract 5

I. Introduction

A. Electron Pair Production by a Photon in the Field of an Electron

1. Background 6

2. Theoretical Cross Sections 7

B. Previous Experimental Work

1. Total Cross Section 11

2. Differential Cross Section 13

C. Purpose of this Investigation 13

D. Choice of Experimental Technique

1. Necessity of Photographic Method 14

2. Desirability of Hydrogen 14

3. Need for Magnetic Field 14

4. Availability of Bubble Chamber 14

II. Apparatus and Procedure

A. Geometry of Experiment 16

B. Collimation and Shielding 16

C. Lithium Hydride Beam Hardener 19

D. Sweep Magnets 19

E. Synchrotron 20

F. Liquid Hydrogen Bubble Chamber

1. Description

a. General 21

b. Thin Windows 23

c. Magnetic Field 23

d. Chamber Alignment 23

e. Photography 25

2. Operation 25

Contents

G. Beam Monitors
1. General 26
2. Cornell-Type Thick-Wall Ionization Chamber . . 29
3. Nunan Thin-Wall Ionization Chamber 30
4. Scintillation Coincidence Counter 30
III. Pair-Spectrometer Measurements
A. Introduction 33
B. Apparatus and Procedure
1. Experimental Arrangement 33
2. The Pair Spectrometer 33
3. Procedure 35
C. Bremsstrahlung Quantum Limit Energy . . . . .
D. Spectral Transmission of the Beam Hardener . . . 37
IV. Measurement of Photographic Tracks
A. Method 42
B. Apparatus
1. Stereoscopic Viewer 42
2. Projection Table 42
C. Reconstruction of Event from Stereo Measurements
1. Bubble Chamber Optics 45
2. Track Reconstruction 49
D. Procedure
1. Scanning
a. Types of Events Recorded 50
b. Criteria for Acceptance of Events 51
c. Checking Procedure 52
2. Method of Measurement
a. Curvature 52
b. Range 53
c. Angle 53
d. Location 54
e. Magnification 54

Contents

V. Analysis of Data
A. Spectrum
1. Schiff Spectrum 55
2. Modifications due to the Target and Collimators 55
3. Incident Spectrum 59
B. Kinematics of Triplet Production 60
C. Cross-Section Calculations 62
D. Scanning Efficiency 65
1. Human Detection Efficiency 65
2. Spurious Events 67
3. Effective Path Length 70
E. Accuracy of Measurement 71
F. Density of Hydrogen 72
G. Monitor Results 72
VI. Results and Discussion
A. Cross Section for Visible Recoils
1. Relative Cross Section 74
2. Absolute Cross Section 74
B. Total Cross Sections
1. Pair-plus-Triplet Cross Section 78
2. Triplet Cross Section 80
C. Partition Function 83
D. Recoil Momentum Distribution 87
E. Recoil Angular Distribution 105
F. Multiple Pair Production 109
G. Summary 109
Acknowledgments 111
References 112

ELECTRON TRIPLET PRODUCTION BY HIGH-ENERGY PHOTONS IN HYDROGEN

Duane Charles Gates

Lawrence Radiation Laboratory
University of California
Berkeley, California

September 1, 1960

ABSTRACT

The 323-Mev bremsstrahlung beam from the Berkeley synchrotron was used to produce electron pairs and triplets in the Alvarez 4-inch-diameter liquid hydrogen bubble chamber. The Compton electron background in the chamber was reduced by the use of 1.36 radiation lengths of lithium hydride in the beam path. The photon flux was monitored with a Cornell-type thick-wall ionization chamber. Of the 24,000 events photographed, 5417 triplets and 4019 pairs were analyzed. The following results were obtained: (a) The ratio of apparent triplets to apparent pairs was equal to 0.291 ± 0.0097. (b) The apparent triplet cross section (detectable recoils) rises logarithmically with photon energy to 100 Mev, then levels off. (c) The total triplet cross section agrees with that of Borsellino. (d) The positron energy distribution agrees with that of Wheeler and Lamb. (e) The recoil momentum distribution agrees substantially with that of Suh and Bethe, however, their result is slightly too large in the region of large recoil momenta. (f) The recoil angular distribution was measured. Recoils with momenta greater than 1 Mev/c predominate on the small-angle side of a peak at 50 degrees. (g) Approximately one event due to multiple pair production was expected. None was found.

I. INTRODUCTION

A. Electron Pair Production by a Photon in the Field of an Electron

1. Background

Electron pair production by a photon in the field of an electron, commonly called triplet production, is one of the major electromagnetic processes contributing to the absorption of energetic photons in light elements. For this reason, it might at first seem surprising that detailed experimental and theoretical descriptions of the process have lagged behind the corresponding description of pair production in the nuclear field. But several important differences between pair production and triplet production complicate the latter case. These are discussed below.

Bethe and Heitler[1] originally developed the theory of pair production in the Born approximation, taking into account atomic screening by use of the Fermi-Thomas model of the atom. Their method considered only the static nuclear field and thereby neglected the effect of retardation (due to recoil), which for the nuclear case is negligible.

Perrin[2] was the first to point out the possibility of triplet production. He showed that in the laboratory system the threshold energy is $k = 4\ mc^2$, twice that for pair production, and estimated the cross section to be the same as that for a nucleus with $Z = 1$.

Wheeler and Lamb[3] developed triplet theory for high-energy photons along the lines of the Bethe-Heitler pair theory, properly taking into account the difference in atomic screening between the two cases. For hydrogen they calculated the pair and triplet cross sections, using exact atomic wave functions for the screening effect, and their result supersedes that of Bethe and Heitler for that case. They neglected (in the triplet theory) the effect of retardation, the γ-e interaction, and the exchange effect. But since these effects are important only for large recoils where screening is unimportant, the Wheeler-Lamb screening correction can be applied to later unscreened results which treat the large recoils properly.

Borsellino[4] was the first to consider the effect of retardation on the cross section. Retardation effects are a result of the motion of the recoiling electron, and become important at relativistic velocities. In the high-energy limit his result approaches the unscreened Bethe-Heitler cross section. Although he neglected the γ-e interaction and exchange effect, his retardation correction to the Bethe-Heitler result is of the same order as these effects (estimated by Joseph and Rohrlich), and suggests that they are probably negligible in the extreme relativistic limit also. His work served as the basis for a later calculation of the recoil distribution by Suh and Bethe.[5]

Votruba[6] was the first to formulate the theory exactly (in Born approximation; no screening). However, owing to the complexity of the equations he was forced, at high energies, to make an approximation which limits the validity of his results to the region of small recoils. Later, Joseph and Rohrlich[7] improved the accuracy of Votruba's results and showed that the cross section for small recoils is the same as that for pair production.

Unfortunately, no one as yet has calculated the recoil angular distribution, or made a quantitative estimate of the effect of the γ-e interaction and exchange effect on the large recoil part of the differential and total cross sections for the energy range of this experiment.

2. Theoretical Cross Sections

The lowest-order Feynman diagrams for triplet production are the four diagrams shown in Fig. 1 plus four additional diagrams which are the same except for exchange of the two negatons in the final state.

In the notation of Jauch and Rohrlich[8] the differential cross section may be expressed as

$$d\sigma = (2\pi)^2 \frac{\omega\epsilon}{|p.k|} \int d^3p'\, d^3p''\, d^3p_+\, \delta(p'+p''+p_+-p-k) \sum_{\text{spins}} \left|(p'p''p_+ \left|M^{(3)}\right| pke)\right|^2$$

$$= \frac{\alpha}{(2\pi)^2}\, r_0^2\, \frac{\beta'\beta''\epsilon'\epsilon''d\epsilon'}{|p.k|\,\epsilon_+} \cdot \frac{d\epsilon''}{d(\epsilon'+\epsilon''+\epsilon_+)} \times d\Omega'\, d\Omega'', \qquad (1)$$

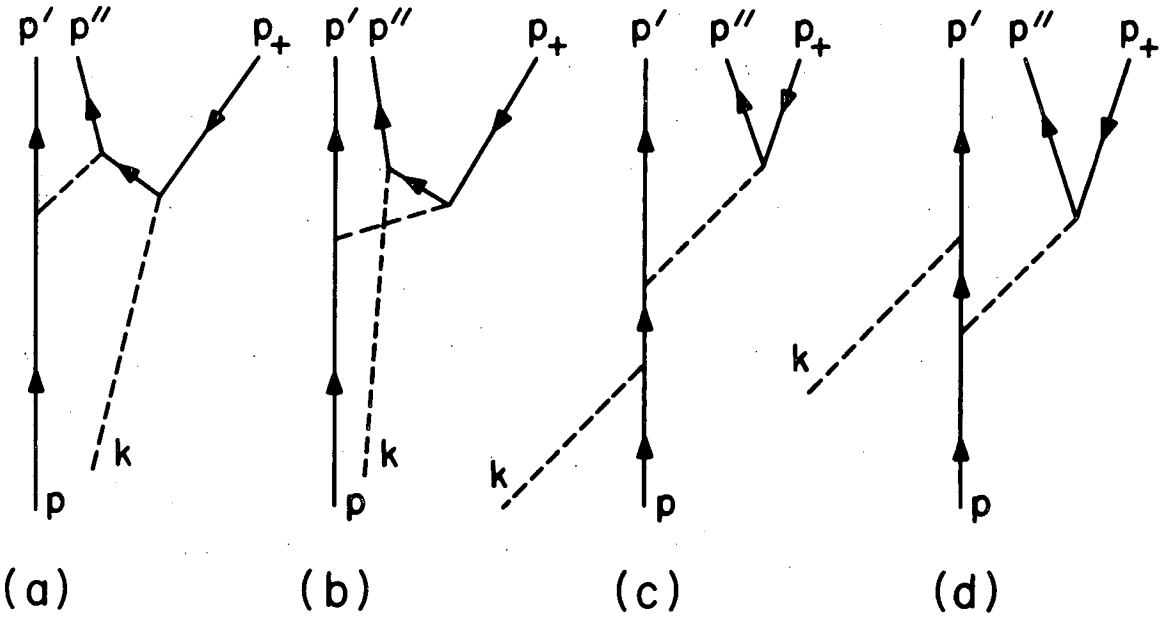

MU-21586

Fig. 1. Lowest-order Feynman diagrams for triplet production. Not shown are the four exchange diagrams which may be obtained by exchanging p′ and p″.

where ω and k are photon energy and momentum; β, p, and ϵ are electron v/c, momentum, and energy; and X is a dimensionless trace which was first evaluated completely by Votruba.[6] The expression for X is so complicated (about four pages long) that integrations of Eq. (1) have been performed only in the limits of very high and very low (near threshold) photon energies.

Votruba obtained a simplified expression for the differential cross section in the limiting case $k \gg 1$, $q \ll 1$ (of order $q_{min} = 2/k$), where q is the recoil momentum in units of mc. Joseph and Rohrlich[7] subsequently integrated Votruba's expression exactly, obtaining the recoil momentum distribution (in units of αr_0^2)

$$\Gamma(k, q, M) = (4/q) \Bigg\{ (2/3)(1-2/kq)^{1/2}(7/6 + 25/6kq - 2/(kq)^2) + \\ - (2/kq - (1 - \ln(2kq))/(kq)^2 + 4/3(kq)^3 \ln\left(\frac{1 + (1-2/kq)^{1/2}}{1 - (1-2/kq)^{1/2}}\right) + \\ - (2/(kq)^2)\left[L\left(\frac{1+(1-2/kq)^{1/2}}{2}\right) - L\left(\frac{1-(1-2/kq)^{1/2}}{2}\right)\right]\Bigg\}, \qquad (2)$$

where $L(y) = \int_0^y dx. \left[\ln(1-x)\right]/x$ denotes the Spence function.[9] Since this result is identical with that of Suh and Bethe,[5] who neglected the γ-e interaction and exchange terms, it follows that those terms give no contribution in the region $q \ll 1$ (of order q_{min}).

Suh and Bethe also calculated the recoil momentum distribution for larger recoil momenta. For the case $k \gg 1$, $q \ll k$, $kq \gg 1$ (or $q \gg q_{min} = 2/k$), $\Gamma(k, q, M)$ can be expressed as a series of descending powers of k, the recoil momentum distribution being

$$\Gamma(k, q, M) = \Gamma_0(k, q, M) + k^{-1}\Gamma_1(k, q, M) + \ldots, \qquad (3)$$

where k = photon energy, q = recoil momentum, and M = mass of recoil particle, all values being expressed in units of the pair particle (electron) rest energy. Suh and Bethe were able to show that $\Gamma_0(k, q, M)$ has the same functional dependence for triplet and pair production when expressed in appropriate variables. In the case of triplet production ($M = 1$) they get

$$\Gamma_0(k, q, 1) = \frac{2}{3} \frac{q}{W(W-1)^2} \left[1 + \frac{2W-3}{q} \ln(W + q) \right], \tag{4}$$

where $W = \sqrt{q^2 + 1}$. $\Gamma_1(k, q, M)$ is a small negative correction and the reader is referred to Ref. 5 for its evaluation.

Note that $\Gamma_0(k, q, 1)$ is independent of photon energy. Since the γ-e interaction terms are of relative order q/k and the exchange terms are of order $k^{-1}\ln k$,[7] the total cross section approaches the Wheeler-Lamb cross section[3] in the extreme relativistic limit.

At moderately high energies, the total cross section is expected to lie between the results of Borsellino and Votruba (after correction for screening):

$$\Phi_t^V - \left[\Phi_p^{BHunscr}(Z=1) - \Phi_t^{WL} \right] < \Phi_t < \Phi_t^B - \left[\Phi_p^{BHunscr}(Z=1) - \Phi_t^{WL} \right]. \tag{5}$$

The work of Suh and Bethe[5] shows that in the extreme relativistic limit Φ_t may be expected to approach the upper limit (which becomes Φ_t^{WL}). At lower energies, where the exchange effect cannot be neglected, Φ_t is expected to be nearer to the lower limit.[7] The unscreened cross sections appearing in Eq. (5) are

$$\Phi_t^V = \alpha r_0^2 \left(\frac{28}{9} \ln \frac{2k}{m} - \frac{100}{9}\right), \tag{6}$$

$$\Phi_t^B = \alpha r_0^2 \left\{ \frac{28}{9} \ln \frac{2k}{m} - \frac{218}{27} - \frac{m}{k} \cdot \left[\frac{4}{3} \left(\ln \frac{2k}{m}\right)^3 - 3\left(\ln \frac{2k}{m}\right)^2 + 6.84 \ln \frac{2k}{m} + 21.51 \right] \right\}, \tag{7}$$

$$\Phi_p^{BH\ unscr.} = \alpha r_0^2 \left(\frac{28}{9} \ln \frac{2k}{m} - \frac{218}{27}\right), \tag{8}$$

$$\alpha r_0^2 = 0.5794 \times 10^{-27} \mathrm{cm}^2. \tag{9}$$

Φ_t^{WL} was obtained by numerical integration of the differential triplet cross section, using the screening functions for hydrogen calculated by Wheeler and Lamb.[3]

The upper and lower limits on Φ_t are expected to be valid in the range $k > 40$ Mev. Below 40 Mev the relativistic approximation is known to break down for pair production and the same is probably true for triplet production.

The upper limit is believed to be valid because there is reason to believe[7] that the net effect of the γ-e interaction and exchange terms is to reduce the cross section. The lower limit is believed to be valid because it is the cross section for recoils with $q \leqslant 1$, and the neglected terms have little effect in this region.

B. Previous Experimental Work

1. Total Cross Section

The total cross section for triplet production has been measured at several energies by an absorption method. In this method, the total cross section for all absorptive processes is measured and the triplet cross section is obtained by subtraction of the known experimental or theoretical cross sections for the Compton effect, pair production, etc. The method is not suitable for obtaining differential cross sections.

Anderson et al.,[10] Moffatt et al.,[11] and Malamud[12] used the absorption method to obtain the triplet cross section for hydrogen.[13] Their results have been plotted in Fig. 2 along with the theoretical upper and lower limits, and the Bethe-Heitler pair cross section. They seem to indicate that the triplet cross section does indeed lie between the limits suggested earlier.

Hart et al.,[14] however, have made a direct cloud chamber measurement of the cross section which is near to the Wheeler-Lamb result at low energies, at which they see almost all of the recoils. Their low-energy results are also plotted in Fig. 2. At higher energies, at which the shortest recoils are not detectable, their cross sections for triplets with visible recoils are in reasonable agreement with theory of Suh and Bethe.

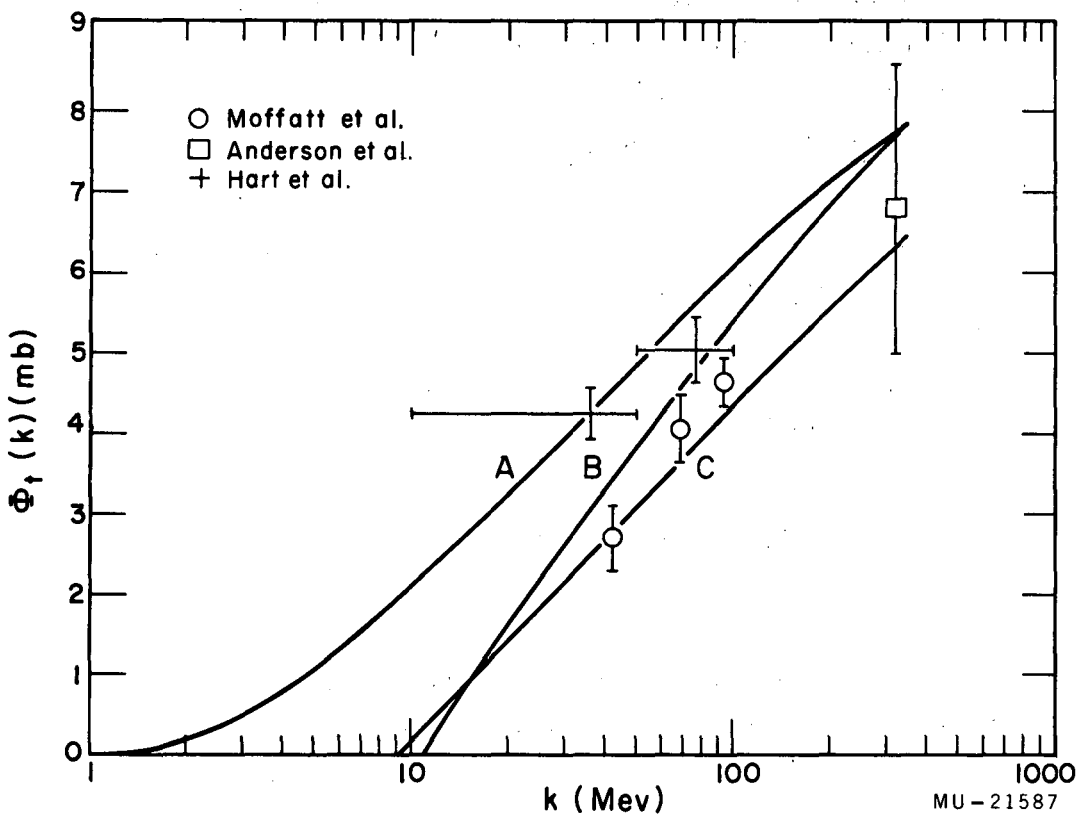

Fig. 2. Results of previous determinations of the triplet cross section in the energy range of this experiment. Also shown are the theoretical triplet cross sections of Borsellino (B) and Votruba (C), and the Bethe-Heitler pair cross section (A).

It was intended that this experiment, in an energy range in which the γ-e interaction and exchange terms are not expected to be completely negligible, should more precisely locate the position of the triplet cross section between the theoretical values and perhaps give an indication of the magnitude of these terms.

2. Differential Cross Section

The experiment of Hart et al. is the only definitive work presenting details of the process. They measured the recoils of about 950 triplets produced by photons in the range $10 < k < 1000$ Mev. They obtained reasonable agreement with the recoil momentum distribution of Suh and Bethe, but noted a small deviation in the region $10 < k < 100$ Mev.

It was intended that this experiment, with many more events in a narrower energy range, should evaluate the deviation more precisely.

C. Purpose of This Investigation

This experiment was undertaken with the aim of measuring the total cross section and determining details of the triplet production process for the range of photon energies available from the Berkeley synchrotron. In view of the paucity of definitive information, both experimental and theoretical, concerning this fundamental process (particularly when this experiment was begun in mid-1956), it was felt that the experiment might serve to check both the validity of the existing theoretical approximations and the correctness of more complete calculations which may be made in the future.[15]

With this object in mind, it was desirable to obtain as much information as possible about the recoil electron, i.e., its momentum and angular distribution. In particular, the large momentum recoils were interesting because they were expected to be most affected by the γ-e interaction and exchange terms. Also these terms might introduce a detectable asymmetry in the energy sharing (partition function) of the pair members.

D. Choice of Experimental Technique

1. Necessity of Photographic Method

One characteristic of triplet production by high-energy photons is that most of the time the pair members are produced in the forward direction with extreme relativistic energies, while the recoil electron travels at a large angle with low energy. Consequently it is virtually impossible to identify an ordinary triplet without actually "seeing" the recoil in association with the pair members. This circumstance, together with a desire to observe the details of the process, necessitates the use of emulsion, cloud chamber, or bubble chamber as a detector.

2. Desirability of Hydrogen

Hydrogen was desirable as a photon target for several reasons. Identification and measurement of events are easiest when there is a minimum of background tracks. Hydrogen is ideal in this respect because in it, the ratio of pairs to triplets is a minimum (for any element, the ratio is approximately equal to Z). Another consequence of its low Z is that the atomic binding of the electron has little effect on the process and is negligible below 100 Mev, i.e., below this energy the target electron may be considered to be a free particle. Also the effect of atomic screening has been accurately calculated by Wheeler and Lamb for hydrogen.

3. Need for a Magnetic Field

A magnetic field was necessary to facilitate measurement of the momenta of the particles whose ranges were too long to be measured accurately or that did not stop in the detector. This was always the case for the pair members.

4. Availability of Bubble Chamber

Practical necessities, plus the screening consideration, thus point to the use of a hydrogen cloud chamber or bubble chamber for an investigation of this nature. It was the availability of the Alvarez 4-inch liquid hydrogen bubble chamber, with its pulsed magnetic field, that made this experiment possible. The chamber was originally designed

as an engineering prototype for larger chambers. But after it had fulfilled its original purpose it was successfully used in several experiments, in spite of its limited size.

II. APPARATUS AND PROCEDURE

A. Geometry of Experiment

Figures 3 and 4 show the arrangement of apparatus used to produce a "hardened" photon beam incident on the bubble chamber unaccompanied by charged particles.

The 323-Mev bremsstrahlung beam from the Berkeley electron synchrotron was collimated to a small diameter 57 inches from the internal synchrotron target. It then passed through approximately one radiation length of lithium hydride (LiH) "beam-hardener" material, which increased the relative number of high-energy photons in the spectrum. After being redefined by the third collimator and cleared of charged particles by the third sweep magnet, the beam then passed through the Alvarez 4-inch diameter liquid hydrogen bubble chamber. Finally it struck the Cornell-type thick-wall ionization chamber used to monitor the beam intensity.

B. Collimation and Shielding

Three lead collimators were used to define the photon beam used in this experiment. Also additional material was placed around the beam path and near the bubble chamber to shield it from stray background radiation produced by the synchrotron, collimators, and beam hardener.

A 10-inch brass-lined tapered primary collimator reduced the beam to 1/8-inch diameter 57 inches from the synchrotron target. This made the beam approximately 1/2-inch diameter at the bubble chamber. The effect of the small aperture on the spectral distribution is discussed in Sec. VA.

The 1/2-inch-diameter secondary collimator just after the primary collimator served primarily as shielding against stray radiation produced by the primary collimator.

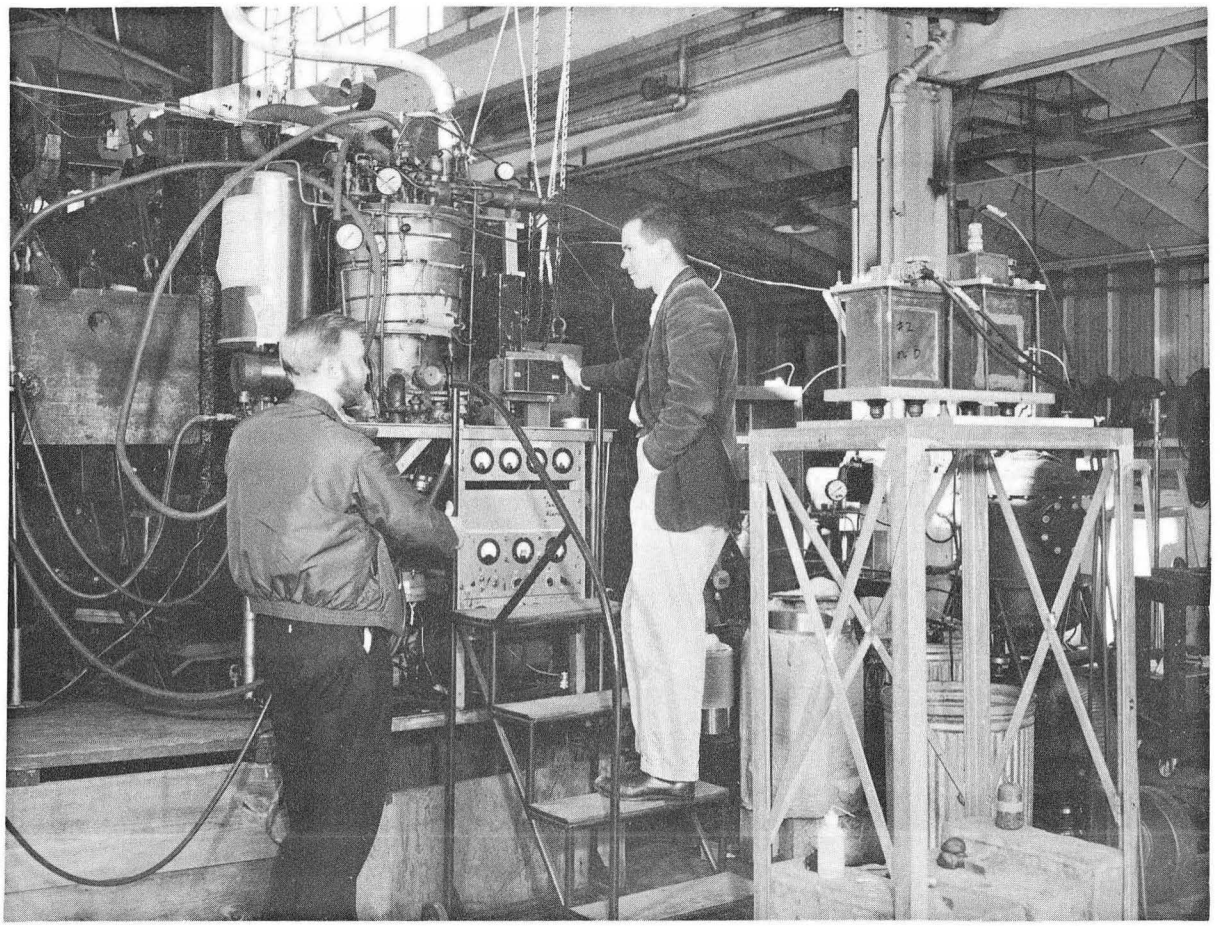

ZN-2522

Fig. 3. Bubble chamber in position.

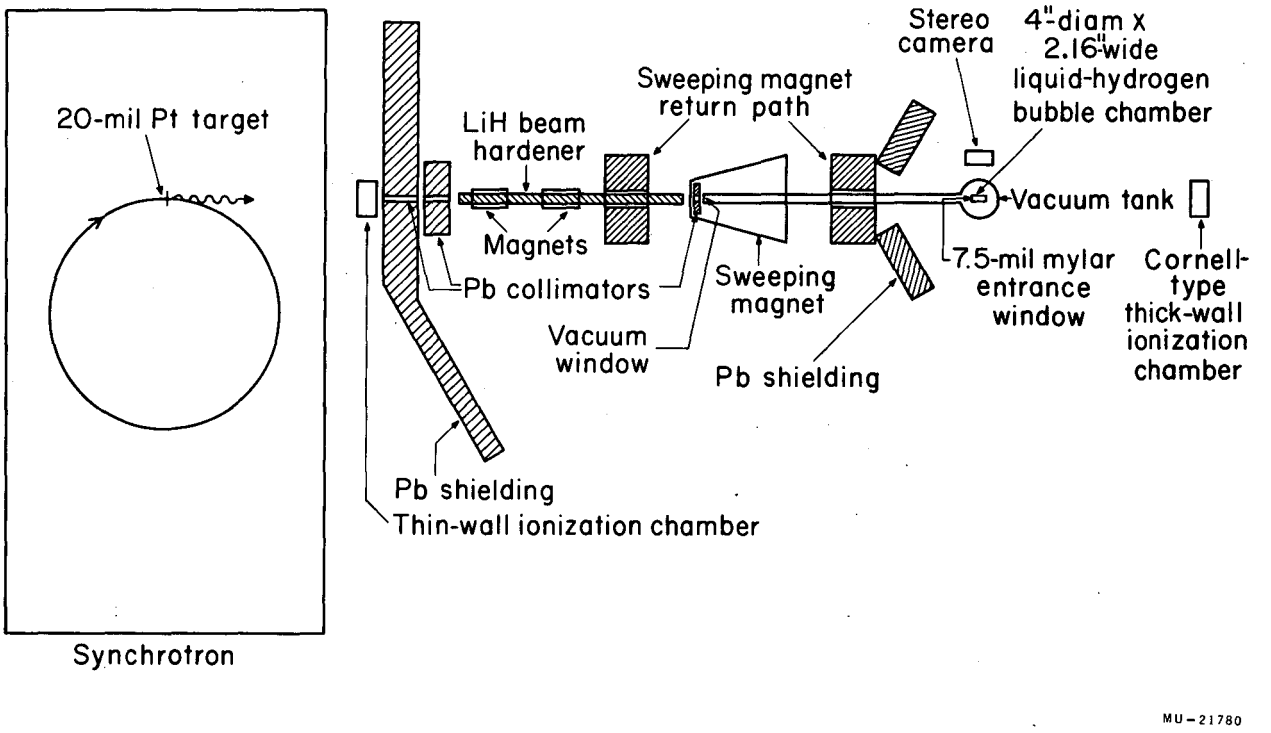

Fig. 4. Schematic diagram of experimental arrangement used during bubble chamber runs.

The 3/8-inch diameter tertiary collimator after the lithium hydride absorber was found necessary to redefine the beam boundary before it reached the bubble chamber and to shield against off-axis particles which might otherwise have been deflected toward the bubble chamber by the last sweep magnet.

C. Lithium Hydride Beam Hardener

The principal source of background particles in the bubble chamber was Compton electrons produced in the liquid itself. Since the Compton cross section is relatively large at energies below 1 Mev, it was desirable to reduce the relative number of low-energy photons in the beam. Lithium hydride was chosen as an absorber for this purpose because it was the lowest-Z material with high enough density to make its use practical. A low Z was necessary in order to minimize absorption of high-energy photons by pair creation, for which the cross section is proportional to Z^2.

The lithium hydride, in granular form, was sealed in six lucite ($H_8C_5O_2$) tubes for ease of handling and to prevent absorption of moisture from the atmosphere. Each tube was approximately 12-in. long by 2 inches in diam with ends 1/16 in. thick. The combined surface density of the lucite ends was 2.27 g/cm^2.

The surface density of the material in the tubes was 99.48 g/cm^2. Since it was not certain how much moisture the lithium hydride might have absorbed before being sealed up, it was necessary to perform an auxiliary experiment to measure the spectral transmission. This measurement is described in Sec. III.

D. Sweep Magnets

One of the problems associated with the satisfactory operation of a bubble chamber in a high-energy photon beam is the establishment of a "clean" beam, i.e., a beam unaccompanied by charged particles. The elimination of charged particles was accomplished by the use of sweep magnets and thin entrance windows in appropriate places.

Three magnets were placed along the photon path between the secondary collimator and the bubble chamber. Their presence served several purposes, the most important of which was the removal of charged particles from the beam.

The first two magnets, operated at 7.6 kilogauss (kG), were placed so that they contained a portion of the lithium hydride absorber between their pole tips. This was done to remove charged particles produced in the primary collimator or in the absorber before they had an opportunity to radiate and add low-energy quanta to the beam. It was later determined by the auxiliary pair spectrometer experiment described in Sec. III that the use of the magnets had no appreciable affect on the spectral distribution of photons in the beam.

The second of these magnets also served to deflect high-energy positrons into the scintillation-counter monitor, which is described in Sec. II. G. 4.

The third sweep magnet, operated at 10.1 kG, removed particles produced in the tertiary collimator and the 10-mil Mylar entrance window for the bubble chamber vacuum system. This window was mounted on the end of a 6-ft vacuum extension, which had the effect of eliminating the charged-particle background which might otherwise have come from the vacuum system entrance window and air column in front of the chamber.

The thick iron return path of the third magnet provided useful shielding against stray radiation from the particles that had been swept from the beam.

E. Synchrotron

The Berkeley synchrotron produced the high-energy photon beam used in this experiment. The machine provided a pulse of photons six times per second. The rf envelope was adjusted so that the pulse duration was 100 μsec. A short pulse duration was required so that bubbles formed in the bubble chamber at different times during the pulse had approximately equal growth times (a few milliseconds). This ensured a uniform bubble size for all tracks.

The pulse duration was not made shorter because of the scintillation counter monitor which is described in Sec. II. G. 4. The synchrotron beam pulse was actually a series of shorter "fine-structure" pulses which occurred every 2×10^{-8} sec, the time for one revolution of the internal electron beam. A total of 5000 fine-structure pulses occurred in a 100-μsec period. This ensured that the 50 or so coincidences counted by the monitor were separated by 2×10^{-8} sec or more, which was much longer than the 3×10^{-9}-sec recovery time of the coincidence unit.

The energy E_0 of the electrons striking the 20-mil internal target was determined to be 323±3 Mev from an auxiliary experiment described in Sec. III. The uncertainty in E_0 was due to this determination, and not to fluctuation in the synchrotron operating parameters.

The voltage on the synchrotron capacitor bank was maintained at 14.9 kv with the limit of day-to-day fluctuations within ± 0.05 kv.

The other parameter that affected the peak energy of the machine was the time of the photon pulse (fall-out) in relation to the time of peak magnetic field. The fall-out and peak field signals were monitored continuously on an oscilloscope and maintained within 200 μsec of each other throughout the experiment.

It is estimated that the peak energy of the machine varied within limits of ± 1 Mev during the experiment.

The intensity of the beam was chosen to produce on the average approximately one electron-positron pair in the bubble chamber for each pulse. This corresponded to an average of 4.0×10^{4} Mev/pulse in the incident spectrum, and is about 10^{-6} times the maximum intensity the machine was capable of providing at the chamber.

F. Liquid Hydrogen Bubble Chamber

1. Description

a. General The Alvarez 4-in.-diam liquid hydrogen bubble chamber used in this experiment has been described in detail elsewhere.[16-18] A schematic diagram illustrating the essential features of the apparatus is shown in Fig. 5.

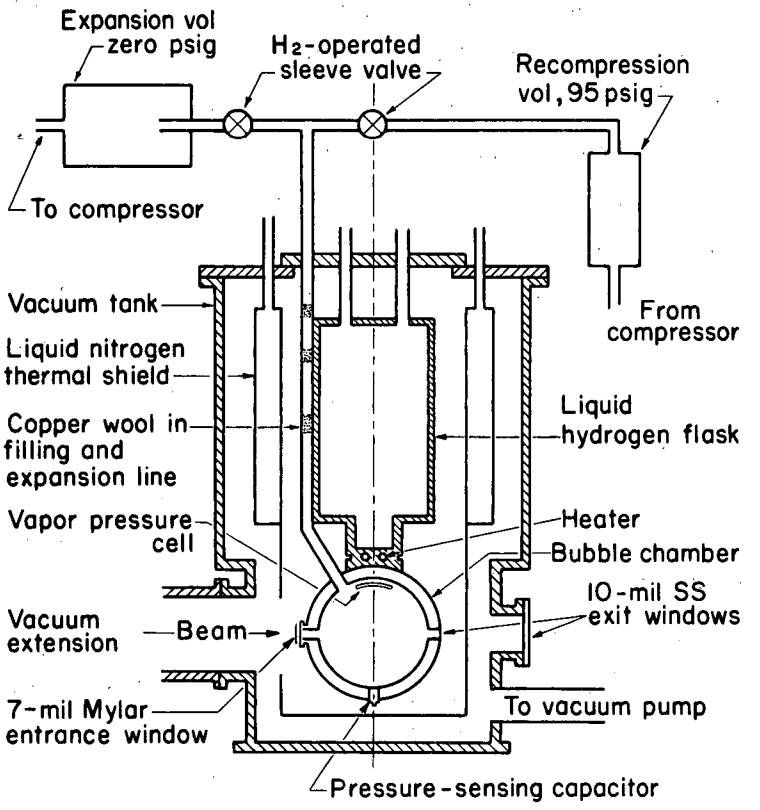

MU-20665

Fig. 5. Schematic of 4-in. bubble chamber.

b. Thin Windows The major problem in operating a bubble chamber in a photon beam is the elimination of undesirable background from Compton and pair creation processes in and near the chamber. For this reason, the bubble chamber was modified to include thin windows at the points where the beam entered and exited the vacuum system and bubble chamber, ports in the heat shield surrounding the chamber, and a 6-ft vacuum extension to eliminate the air column in front of the apparatus.

The 10-mil Mylar entrance window on the vacuum extension was in a magnetic field. Therefore the 7/8-in.-diam 7-mil Mylar entrance window on the bubble chamber was the only significant external source of background. It contributed less than 15% of the background, the remainder being produced in the hydrogen itself.

The 10-mil stainless steel exit windows on the bubble chamber and vacuum system served mainly to allow the beam to reach the Cornell thick-wall ionization chamber without further attenuation.

c. Magnetic Field Another important feature of the bubble chamber was the use of Helmholtz coils to produce the magnetic field. These coils were placed next to the chamber as shown in Fig. 6. They were cooled by thermal conduction via copper straps which were soldered to the liquid nitrogen shield. Under normal operating conditions, the average magnetic field in the chamber was measured to be 0.0151 kG per ampere of current in the coils. The field varied less than 4% across the chamber. Together with the 4.1-mf power supply, the coils formed a resonant L-R-C circuit with a period of 60 msec. The heat produced in the coils was the limiting factor in the repetition rate of the bubble chamber with stable conditions. The peak current was normally about 490 amp, corresponding to a magnetic field of 7.4 kG.

d. Chamber Alignment A thin lead cross, which extended 1/4 in. along the beam direction, was used to facilitate the precision alignment of the bubble chamber in the photon beam. The cross was centered on the entrance window and the chamber position was adjusted until x-ray pictures indicated that the centers of the beam and cross coincided. The cross was removed after alignment was completed.

ZN-2587

Fig. 6. Photograph of 4-in. bubble chamber and Helmholtz coils.

Although there was only 1/16-inch clearance between the beam and the flange on the entrance window, there was no indication of photon interactions with the flange.

e. Photography Tracks were photographed on 100-ft rolls of Panatomic-X film by use of a remotely controlled 35 mm stereo camera mounted 19 inches from the bubble chamber. The camera shutter was left open. The light source was a xenon-filled flash tube which was operated at 10 watt-sec. Dark-field illumination was used. The light was focused by a condensing lens to a spot between the camera lenses so that only light scattered by bubbles in the hydrogen would reach the film.

Images were bright enough so that lens apertures of f/22 could be used, providing good depth of field. Hourly checks of the chamber conditions were made possible by the use of a remotely controlled camera which could produce a developed picture in 60 seconds.

With each exposure, there was also photographed on the same film the data box which contained meters indicating picture number, magnet current, and scintillation monitor counts.

2. Operation

The sensitivity of the bubble chamber to ionizing particles was achieved by placing the liquid in a superheated state at the time the beam passed through the chamber. This was accomplished by a rapid decrease in pressure just before "beam time." Local heating along the ionization path caused the formation of bubbles which were photographed after they had grown to a diameter of approximately 70 microns. After photography, the liquid was rapidly recompressed to a nonsuperheated state. The current pulse in the Helmholtz coils was adjusted to be at a maximum at beam time. The maximum current was measured by a triggered vacuum tube voltmeter and displayed simultaneously in the control area and data box.

The chamber was pulsed once every 20 to 30 seconds. The chamber alone is capable of cycling every 4 sec, but in this experiment it was limited by the heat from the near-by Helmholtz coils, which caused excessive boiling when faster repetition rates were attempted.

A timing signal from the synchrotron was used to synchronize the bubble chamber cycle with that of the synchrotron. Since the synchrotron pulsed 6 times/sec, a Flex-O-Pulse automatic timer was used to select a trigger each time the chamber was ready to be cycled. Because of the time length of the bubble chamber cycle, the trigger had to be taken from the synchrotron pulse preceding the pulse from which the beam was used. A schematic diagram of the operating cycle is shown in Fig. 7.

The chamber operating conditions are given in Table I below.[19] Some ranges of long term variation of the parameters are indicated. (For temperature and vapor pressure, the short-term variation is shown.)

G. Beam Monitors

1. General

One of the quantities necessary in the calculation of a cross section from an experiment of this nature is q, the average photon energy flux per beam pulse. There are several ways that q may be measured, the most accurate method at the synchrotron being the use of the Cornell-type thick-wall ionization chamber. For this reason the Cornell chamber was placed behind the bubble chamber in the position shown in Fig. 4 and was used as the primary monitor for the experiment.

The bubble chamber, however, used only a small fraction of the beam pulses supplied by the synchrotron, while the Cornell chamber monitored all pulses. This meant that the Cornell chamber provided not the actual q used by the bubble chamber, but the q for all synchtrotron pulses. The difference between these two quantities was believed to be negligible, owing to the random nature of the fluctuation of beam intensity from pulse to pulse. However, as a check, a scintillation-counter monitor was used throughout the experiment which detected positrons formed in the lithium hydride and deflected into the counter channel by the second sweep magnet. The scintillation monitor was calibrated periodically against the Cornell chamber by letting it count during all pulses for a short time.

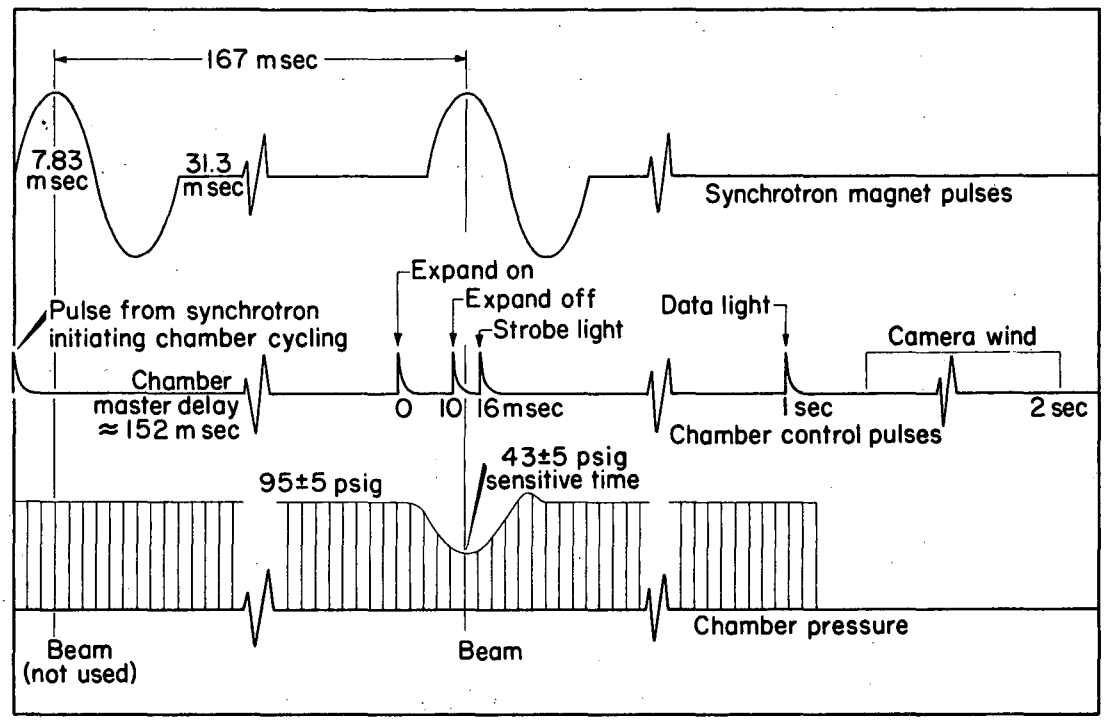

MU-20666

Fig. 7. Schematic of bubble chamber timing. The top axis represents synchrotron magnet pulses, the middle axis represents bubble chamber control pulses, and the lower one displays the chamber pressure variation as measured by a Linlor condenser pressure gauge.

Table I

Chamber operating conditions	
Temperature (^{o}K)	28.3±.03
Vapor pressure (psig)	74.0±.5
Chamber pressure (psig)	
pre-expansion	95± 5
post expansion	43± 5
Beam intensity (Mev/pulse)	4×10^{4}
Magnetic field (kgauss)	7.4±.3

In an early run, the photon beam was pulsed only when the bubble chamber was cycled. This system allowed direct ionization-chamber monitoring of the beam used by the bubble chamber. But the ion current was so small that the Cornell chamber could not be used. Instead the Nunan thin-wall ionization chamber was used. It was placed in front of the primary collimator. For optimum sensitivity, a 4-in.-thick carbon block was placed in front of it to act as a source of ionizing particles.

This method proved to be less satisfactory than the one previously described for three reasons. The average beam intensity was so low that corrections for drift of the monitoring system were important. The calibration of the Nunan chamber varied considerably throughout the run. And it was difficult to maintain a stable beam under these conditions. In later runs, the Nunan chamber served as a secondary monitor and as a hedge against temporary malfunction of the primary monitor.

2. Cornell-Type Thick-Wall Ionization Chamber

The thick-wall ionization chamber used was identical in construction to a widely used type of monitor designed at Cornell University.[20] The chamber was operated at 1500 volts and the ion charge was collected on a 0.001061-μf capacitor by a 100%-feedback vibrating-reed electrometer. The voltage across the capacitor was recorded on a Speedomax recorder, with full scale equal to 0.3 volt.

Cornell-type chambers have been calibrated at Purdue[21] and Cornell[22] universities. Their results are in good agreement at E_0=323 Mev. By combining their data, a value of $(3.83\pm0.08)\times10^{18}$ Mev/coulomb was obtained as the total energy in the spectrum represented by each collected coulomb of charge. This value, however, was for an unmodified bremsstrahlung beam and a chamber filled with air at 273.2°K and 760 mm Hg pressure. Since the chamber used in this experiment was filled at approximately 286°K and 744 mm Hg pressure, a correction factor of 1.07±0.016 was applied. Another correction factor of 3.865±0.008 was applied to take into account the reduction of the beam intensity before it reached the

Cornell chamber. This factor was determined by monitoring equal amounts of beam, as determined by the Nunan chamber, with the lithium hydride and carbon in and out of the beam and taking the ratio of the collected charges.

Combining these results, we get the calibration factor $(15.84 \pm 0.40) \times 10^{18}$ Mev/coulomb for the total energy in the primary spectrum (the spectrum at the primary collimator). For convenience in data reduction, the calibration value was re-expressed in terms of "dumps" (1 dump = 0.300×0.001061 μcoul), that is, $(5.04 \pm 0.13) \times 10^{9}$ Mev/dump. The monitor data were subject to a -9% correction due to drift in the electronics. This correction and its accuracy are discussed in Sec. V. G.

3. Nunan Thin-Wall Ionization Chamber

The thin-wall ionization chamber was operated at 1500 volts in conjunction with an electrometer and Speedomax recorder in the same manner as the Cornell chamber. The Nunan chamber was less reliable than the Cornell chamber for absolute monitoring purposes. Its position in front of the primary collimator made it sensitive to variable synchrotron operating conditions which did not appreciably affect the collimated beam. Consequently it was used as a stand-by monitor during the bubble chamber runs. The calibration of the Nunan chamber relative to the Cornell chamber was 7.5±0.5 Nunan dump/Cornell dump (1 Nunan dump = 0.0 0956 μcoul).

4. Scintillation Coincidence Counter

The scintillation monitor consisted of two 3×3-inch plastic scintillators, each viewed by a 1P21 photomultiplier. A block diagram of the electronics is shown in Fig. 8. The monitor was located between the second and third sweep magnets and was shielded so that only high-energy positrons could reach it. This was done to make it most sensitive to the high-energy photon flux, as was the Cornell chamber. Signals for the phototubes were first amplified. Then those in coincidence were counted with a 10-Mc decade scaler. The counts were indicated on two decade meters in the data box so they would appear on film beside each

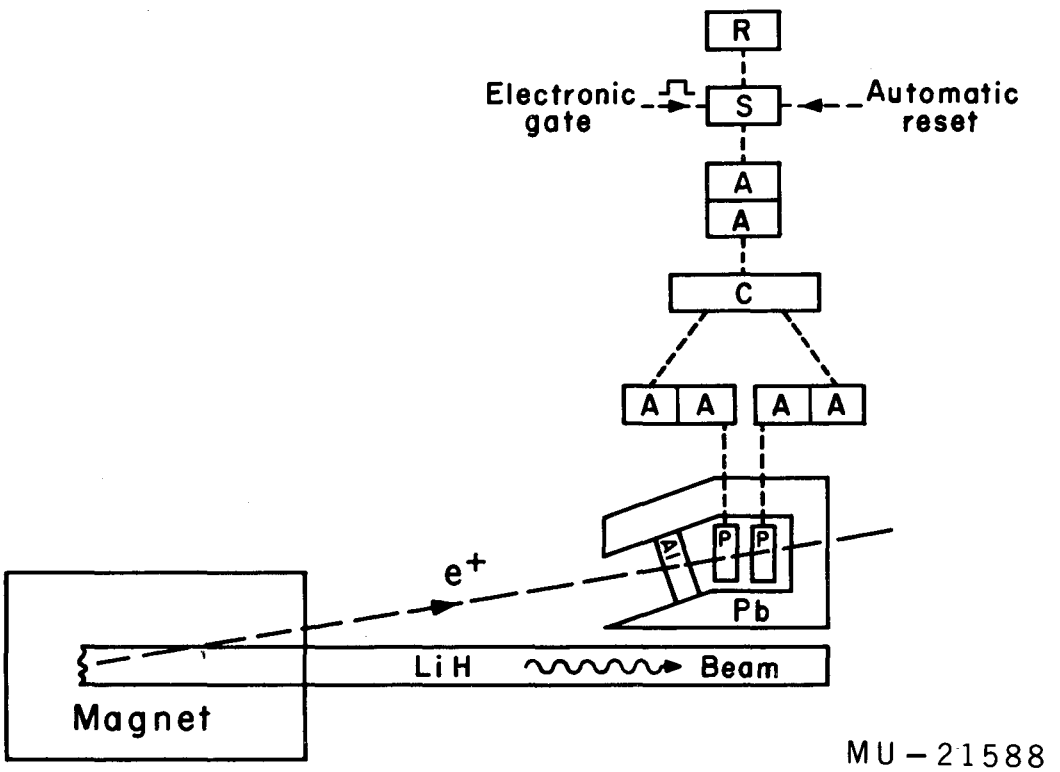

Fig. 8. Schematic representation of scintillation counter monitor setup and electronics: P represents plastic scintillator viewed by 1P21 phototube; Pb, lead shield; Al, aluminum filter; LiH, lithium hydride tube in beam path; A, 20-db amplifier; C, coincidence circuit; S, 10-Mc decade scaler; R, remote meter readout in data box.

picture of the bubble chamber. The scaler was electronically gated so that it would count only during the beam pulses that the bubble chamber used, and an automatic reset was employed which zeroed the meters before the next pulse.

The scintillation monitor was calibrated in terms of the Cornell chamber monitor by operating the scaler ungated, so that it would respond to every beam pulse, as did the Cornell chamber. During normal bubble chamber operation, the number of monitor counts was recorded on the film beside the picture of the chamber. Thus it was possible to determine the actual amount of beam flux used and compare it with the amount calculated from the Cornell chamber data (see Sec. V. G.). This procedure was carried out for only a small portion of the film because of the large amount of time and effort required. It was found that the ratio of the average q-per-synchrotron-pulse to the average q-per-used-pulse was equal to 1.037 ± 0.024. The error indicated is entirely due to the uncertainty in the drift correction to the Cornell chamber data. This result shows that the Cornell chamber was a satisfactory monitor for this experiment.

III. PAIR-SPECTROMETER MEASUREMENTS

A. Introduction

A knowledge of the bremsstrahlung quantum limit energy and of the spectral transmission of the beam-hardening material is essential for an accurate calculation of the photon spectrum incident on the bubble chamber. These quantities were measured in an auxiliary experiment with an electron pair spectrometer, as follows.

B. Apparatus and Procedure

1. Experimental Arrangement

A diagram of the experimental arrangement for the pair spectrometer measurements is shown in Fig. 9. The photon beam from the synchrotron passed through a thin-wall ionization chamber and was collimated to 1/8-inch diameter 57 inches from the target. Subsequently it passed through a 1/2-inch-diameter secondary collimator and the beam hardener with its two sweep magnets. This much of the setup was identical with that for the bubble chamber experiment.

After leaving the hardener, the beam traversed a 9.5-ft extension connected to the volume between the pole tips of the pair spectrometer. The spectrometer and extension were filled with helium gas slightly above atmospheric pressure.

Photons produce about one-tenth as many pairs in helium ($Z = 2$) as in air ($Z = 7.3$) at the same pressure. Consequently, the use of helium served to reduce the background coincidences in the spectrometer to a reasonable level (less than 10% of foreground) and eliminated the necessity of a vacuum system.

A 10-kG sweep magnet was placed just ahead of the pair spectrometer to remove charged particles produced in the beam hardener and lucite window on the helium extension.

2. The Pair Spectrometer

The pair-spectrometer geometry and electronics have been described in detail elsewhere.[23,24] However, it is appropriate here to describe some of the general features of the apparatus.

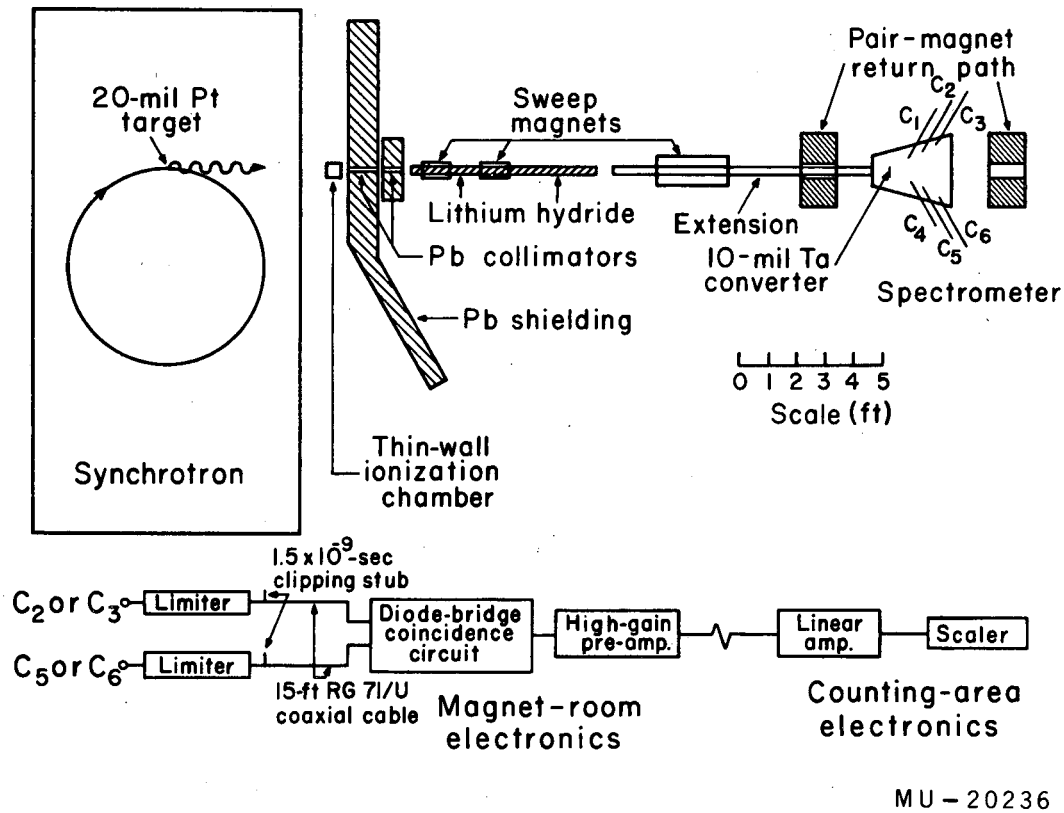

Fig. 9. Schematic of experimental arrangement used for transmission measurements.

The pair spectrometer is used to detect high-energy photons of selected energies by a coincidence counting method. Electron-positron pairs produced by photons striking the 0.010-inch-thick tantalum converter are deflected through circular arcs by the uniform magnetic field. The electron detectors, three on each side of the pair magnet, were placed along a line making an angle of 30 degrees with the beam axis and passing through the center of the converter.

This geometry makes the easily measurable converter-detector distance equal to the electron radius of curvature which, with the magnetic field, determines the electron momentum. For this experiment, two photon energy channels (here-after called 2+5 and 3+6) were used by making coincidences between detectors C2 and C5, and C3 and C6, respectively, whose positions are shown in Fig. 9.

The electron detectors were mounted on 3-foot lucite light pipes viewed by 1P21 photomultiplier tubes. Coincidences were detected in a Neher-type diode bridge circuit,[25] after which they were amplified and scaled in the counting area. A block diagram of the electronics is included in Fig. 9.

3. Procedure

The rf envelope of the synchrotron was adjusted to spread out the beam over a 2.5-msec period during each pulse. Also, the beam intensity was maintained at a level allowing only a few coincidences per pulse. These steps insured instantaneous counting rates which could be handled efficiently by the electronics.

Absolute monitoring of the beam intensity was not necessary for the spectrometer measurements, since only relative counting rates were needed to determine the desired quantities. The thin-wall pre-collimator Nunan ionization chamber was used to monitor the intensity in the same manner as for the bubble chamber experiment. Related runs were done in cycles of less than an hour's duration in order to minimize the effect of any drift in the monitoring system.

Pairs created in the helium gas in the spectrometer contributed to a background of real coincidence counts, which was determined by separate runs with the converter out of the beam path.

Compton electrons and unrelated pair electrons could cause random "accidental" coincidences. Their counting rate was determined by delaying one of the signals to the coincidence circuit by a time equal to one revolution of the internal electron synchrotron beam (2×10^{-8} sec).

A typical cycle of runs would include measurements of real foreground (converter in), accidental foreground (delayed signal, converter in), and background (converter out). Cycles were repeated several times for each magnetic field value.

For each new setting of the magnet current the previous magnetic history was first erased by saturating the magnet and then shutting off the current before applying the new current.

A curve of the magnetic field vs. the voltage across a standard shunt had been measured previously by using proton nuclear magnetic resonance equipment.[26] These values were verified during this experiment by a search coil and magnetometer apparatus accurate to 1% of full scale. The magnetic field for individual runs was determined from a precise measurement of the shunt voltage by using a potentiometer accurate to 0.1%.

C. Bremsstrahlung Quantum Limit Energy

The photon energies detected by the two pair-spectrometer channels (2+5 and 3+6) are given by the equations

$$k_{2+5} = 0.300\ H(L_2 + L_5), \tag{10}$$

$$k_{3+6} = 0.300\ H(L_3 + L_6),$$

where k, H and L represent photon energy in Mev, magnetic field in kilogauss, and converter-detector distance in centimeters, respectively. The peak energy of the spectrum is given by the relation

$$k_{max} = E_0 - mc^2, \tag{11}$$

where $E_0 - mc^2$ is the kinetic energy of the electrons that strike the internal target of the synchrotron. This energy was determined by measuring the counting rate vs. magnetic field for the two pair-spectrometer channels and extrapolating to zero counts. The extrapolated value of H_{max} for each channel was then used to calculate $E_0 - mc^2$. The results are summarized as follows.

Channel	Sum of radii (cm)	H_{max} (kG)	$E_0 - mc^2$ (Mev)
2 + 5	103	10.57	326 ± 1.5
3 + 6	140	7.62	320 ± 1.5

From these values, the peak energy was found to be

$$E_0 - mc^2 = 323 \pm 3 \text{ Mev.} \tag{12}$$

The error of this determination is larger than the errors due to variation of the synchrotron operating conditions. Hence, the effect of those variations on the peak energy during the bubble chamber experiment can be neglected.

D. Spectral Transmission of the Beam Hardener

The transmission of the beam hardener for a photon energy k is equal to the ratio $\frac{I(k)}{I_0(k)}$ of the transmitted photon intensity to the intensity incident on the beam hardener. The ratio of intensities was obtained from a measurement of the relative counting rates of the pair spectrometer at several photon energies with the beam hardener in and out of the beam. If C is the number of coincidence counts for an integrated beam intensity M, and we use the notations r = real coincidence, acc = accidental coincidence, c = converter, h = hardener, then we can write

$$\frac{I}{I_0} = \frac{\left[\left\{\left(\frac{C}{M}\right)_r - \left(\frac{C}{M}\right)_{acc}\right\}_{c\ in} - \left\{\left(\frac{C}{M}\right)_r - \left(\frac{C}{M}\right)_{acc}\right\}_{c\ out}\right]_{h\ in}}{\left[\left\{\left(\frac{C}{M}\right)_r - \left(\frac{C}{M}\right)_{acc}\right\}_{c\ in} - \left\{\left(\frac{C}{M}\right)_r - \left(\frac{C}{M}\right)_{acc}\right\}_{c\ out}\right]_{h\ out}}, \qquad (13)$$

where the real and accidental coincidence counts were obtained by using the procedure described in Sec. III. B. 3.

The quantities in Eq. (13) were measured several times in cyclical manner for ten different photon energies. A total of 68 determinations of I/I_0 was obtained.

The individual determinations of I/I_0 were combined statistically at the various photon energies. The resulting values are given in Table II, and are also plotted in Fig. 10.

Table II

Measured transmission of beam-hardener material

k (Mev)	I/I_0
24.9	0.2713 ± 0.0091
34.3	0.3108 ± 0.0137
41.0	0.3060 ± 0.0056
56.2	0.3249 ± 0.0088
82.5	0.3463 ± 0.0048
113.4	0.3510 ± 0.0079
172.7	0.3486 ± 0.0043
197.7	0.3503 ± 0.0037
237.3	0.3464 ± 0.0055
271.6	0.3476 ± 0.0052

A smooth curve through the measured points was desirable for use in accurately determining the transmitted spectrum. For this purpose, the theoretical cross sections of LiH, LiOH, and $H_8C_5O_2$ (lucite) were used to determine the shape of the curve.

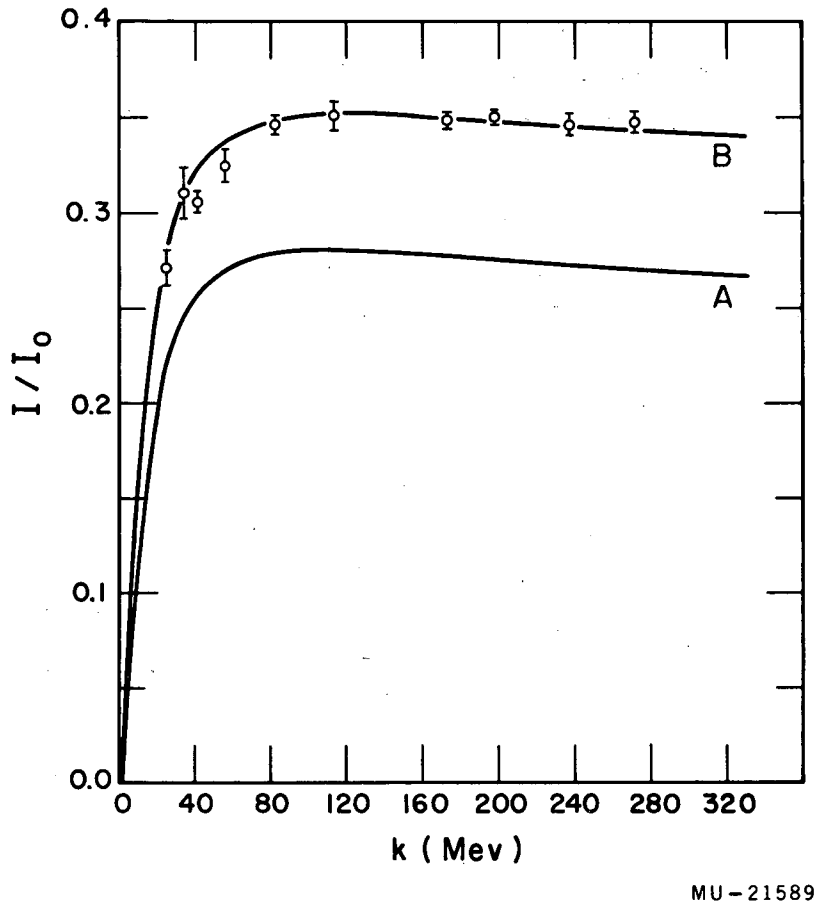

Fig. 10. Transmission measurements of the LiH beam hardener. The experimental points shown were fitted to a combination of the transmissions of elements Li, H, C, and O to include the effect of the absorbed H_2O and lucite ends (Curve B). Curve A includes the effect of the carbon block used with the precollimator ionization chamber.

The molecular photon-attenuation cross sections were taken to be the sums of the atomic cross sections

$$\Phi_{atom} = \Phi_{Compton} + \Phi_{pair} + \Phi_{triplet} \tag{14}$$

The Compton cross section was calculated from the Klein-Nishina formula for the free electron.[27] The pair cross section was that of Bethe and Heitler[28] corrected for deviation from the Born approximation.[29] The triplet cross section was that of Wheeler and Lamb,[3] corrected for the exchange effect as suggested by Joseph and Rohrlich.[7,30]

The measured surface density of the beam hardener, 99.48 g/cm^2, was taken to be partly LiOH as well as lithium hydride. The fraction of LiH was least-squares adjusted to obtain the best fit to the data with the constraint

$$t_{measured} = f t_{LiH} + (1-f) t_{LiOH}, \tag{15}$$

where t is the surface density and f is the fraction of LiH.

The value of f giving the best fit was $f = 0.748 \pm 0.006$. This value was used in the calculated spectral transmission of the beam hardener, curve B of Fig. 10. The χ^2 value for the least-squares fit was 56, which was about one standard deviation from the expected (most probable) value of 66.5, indicating a reasonable fit to the measured values.

The transmission of the carbon block used to increase the sensitivity of the thin-wall ion chamber was measured at four photon energies in the same manner as described above.

The results are given in Table III. Since the measured transmission of the carbon block was in good agreement with the theoretical transmission, calculated by using the measured surface density of 16.29 ± 0.06 g/cm^2, the theoretical value was combined with that for the beam hardener. The result, curve **A** of Fig. 10, is the spectral transmission, T(k), of the significant material in the photon beam and is to be combined with the primary spectrum to obtain the transmitted spectrum, which was incident on the bubble chamber.

Table III

Measured transmission of carbon block	
k (Mev)	I/I_0
24.9	0.7595 ± 0.0560
34.3	0.8320 ± 0.0829
197.7	0.7703 ± 0.0088
271.6	0.7710 ± 0.0125

IV. MEASUREMENT OF PHOTOGRAPHIC TRACKS

A. Method

A major task of the experiment was the finding and measuring of the events of interest that were photographed during the bubble chamber run. There were 39 rolls of film containing approximately 16,000 stereoscopic pictures. All the pictures were scanned for events at least twice. The first scan was perfomed by projecting the bubble chamber picture onto a flat surface, using a chamber-table magnification of 4.14. The second scan was performed by viewing the pictures in a stereoscopic viewer. All events were identified by at least two persons.

The events were measured concurrently with the first scan. Sufficient measurements were performed on most events to allow calculation of the photon energy, pair member and recoil energies, recoil angle, and the position of the event in the chamber. The value of each measurement was dictated into a tape recorder as it was made and at a later time the measurements were transcribed onto forms suitable for use by IBM key-punch operators. After being punched, the cards were processed on an IBM 650 computer which performed the necessary calculations.

B. Apparatus

1. Stereoscopic Viewer

A photograph of the stereoscopic viewer is shown in Fig. 11. It was a simple device using prisms and eyepieces to bring the stereo images to the proper eye spacing. It had the advantage of facilitating rapid scanning of the film.

2. Projection Table

The projection table was used both for scanning and measuring. It was identical in most respects to the Mark III Scanner developed by the Alvarez Group for use with the 10-inch bubble chamber film. A photograph is shown in Fig. 12. The film image is projected vertically

ZN-2516

Fig. 11. Use of the stereo viewer for film scanning.

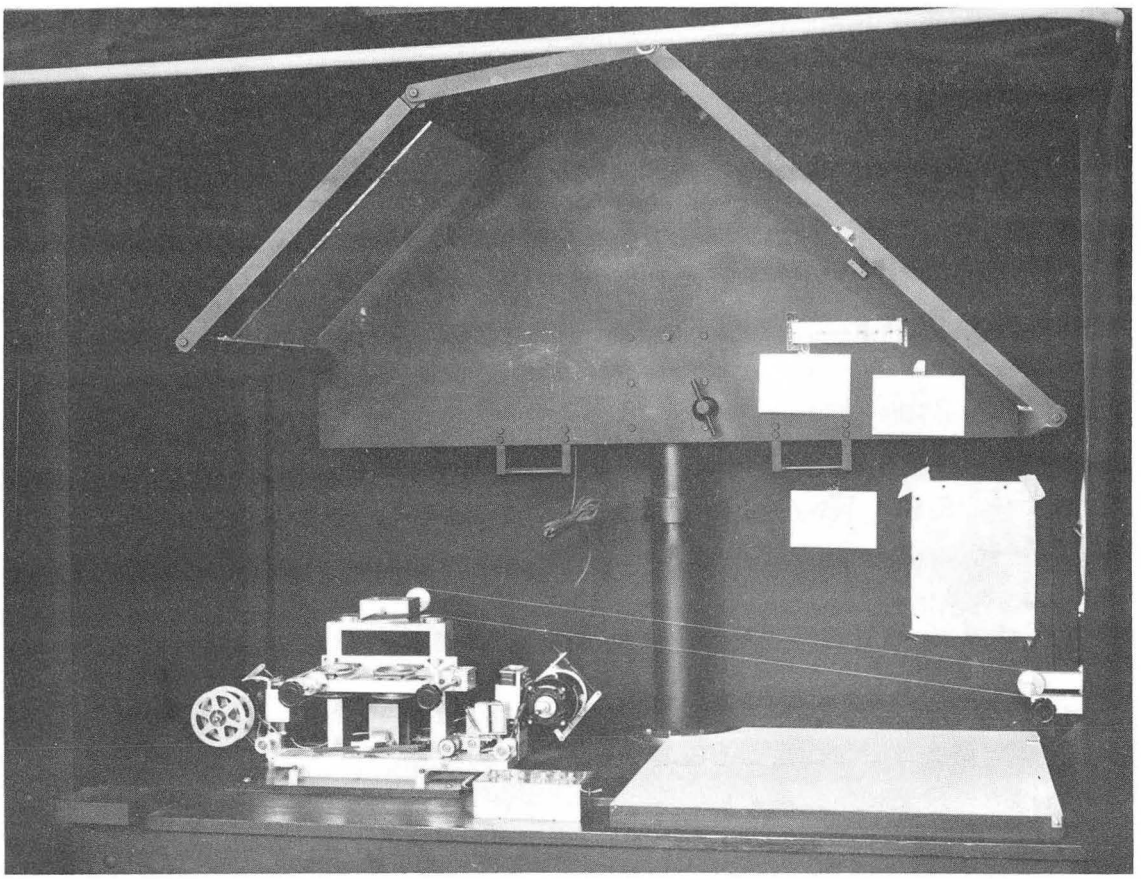

ZN-2588

Fig. 12. Projection table used for film scanning and measurements.

upward and reflected down onto an adjacent white "table" by two front-surface mirrors inclined at 45 deg to the vertical. The film is held flat against a glass backing plate by a mechanical hold-down device and by vacuum suction. The stereo images can be viewed on the table either separately or superimposed. The projection lenses were adjustable so that corresponding points in the two views could be brought into super-position. The film advance was electrically controlled.

C. Reconstruction of Event from Stereo Measurements

1. Bubble Chamber Optics

A diagram of the bubble chamber optical system is shown in Fig. 13. The coordinate system used in the reconstruction of events was chosen so that the z and x axes lay in the plane of the inner face of the bubble chamber window farthest from the camera (the plane of the far fiducial marks). The x axis was parallel to the line joining the lens centers (positive down), while the origin was located so that the y axis (positive toward the camera) passed through the upper right fiducial mark on the near bubble chamber window, as seen from the camera. With this coordinate system, the position of any point in the bubble chamber can be calculated from its z and x coordinates in the two views, the geometrical constants A and D, the window positions and thicknesses and the indices of refraction of hydrogen, glass, and lucite.

It is most convenient to derive the location of a point from measurements in real space in the near fiducial plane in both views, and then to show how these results are modified by the presence of the windows and liquid hydrogen, and by the projection system (projector space).

Let (x, y, z) be the real space coordinates of a point in the chamber; (X_t, Z_t) and (X_b, Z_b) be the intersection with the near fiducial plane of the top (View 1) and bottom (View 2) lens axes, respectively; A be the distance from the lens center to the near fiducial plane; y_0 be the distance from the point to the near fiducial plane and (x_t, z_t) and (x_b, z_b) be the apparent coordinates in the near fiducial plane of the point as seen from the top and bottom lenses, respectively.

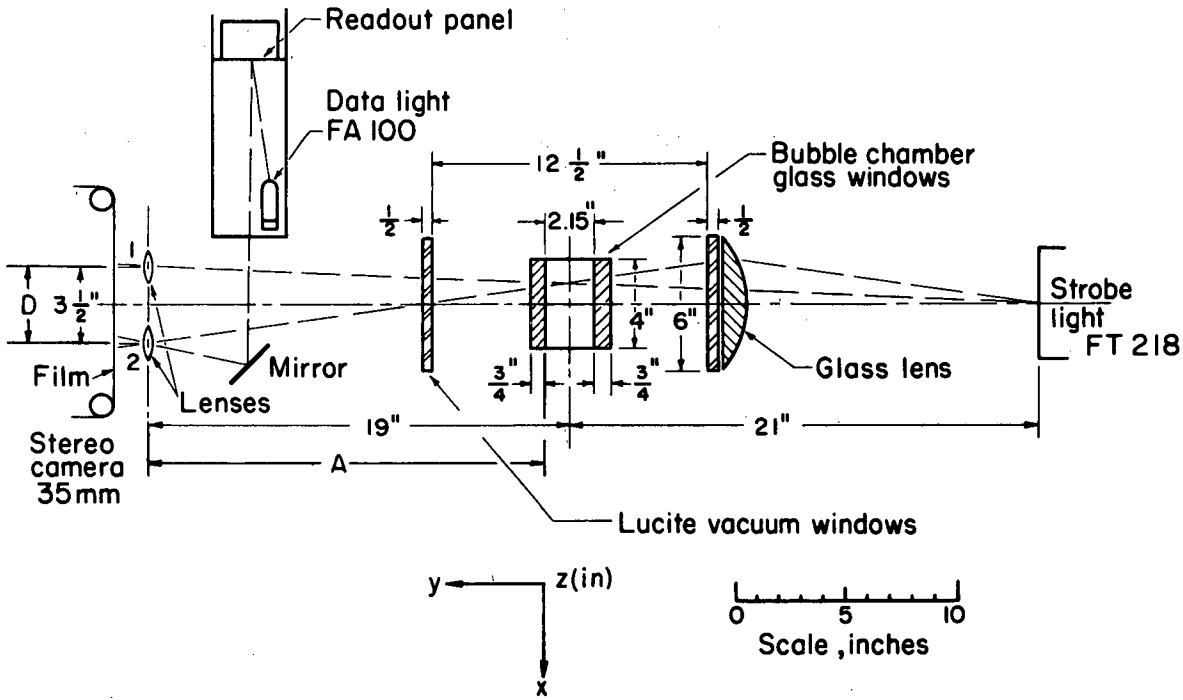

Fig. 13. Bubble chamber optics. The main light source at the right illuminates the chamber, which is viewed by a stereo camera at the left. The orientation of the coordinate system used for track reconstruction is also shown, as are the optical constants A and D.

The following relationships are obtained from the properties of similar triangles:

$$\frac{x_t - X_t}{A} = \frac{x - x_t}{y_0}, \quad \frac{X_b - x_b}{A} = \frac{x_b - x}{y_0}, \quad \frac{Z_b - z_b}{A} = \frac{z_b - z}{y_0} \quad . \tag{16}$$

These equations may be solved to obtain the following expressions for y_0, x, and z:

$$y_0 = \frac{(x_b - x_t)\,A}{(X_b - X_t) - (x_b - x_t)} = \frac{\Delta x}{D - \Delta x}\,A, \tag{17}$$

$$x = x_b\left(1 + \frac{y_0}{A}\right) - \frac{y_0}{A}\,X_b, \tag{18}$$

$$z = z_b\left(1 + \frac{y_0}{A}\right) - \frac{y_0}{A}\,Z_b, \tag{19}$$

where $\Delta x = x_b - x_t$ and $D = X_b - X_t$, the lens separation.

The presence of the bubble chamber and vacuum jacket windows has approximately the same effect as a pair of weak lenses. This is because the rays are all paraxial, the maximum angle being 11 deg, and the windows have parallel plane surfaces. The effect of the windows and the index of refraction of the liquid hydrogen is taken into account by replacing A by A', x by x/m, and z by z/m in Eqs. (17) - (19). The camera and projector magnification factors are taken into account by replacing x_b, x_t, and z_b by x'_b/M, x'_t/M, and z'_b/M, respectively, in the same equations; x'_b and z'_b are the coordinates measured on the projection table, and M is the chamber-table magnification. Thus, in terms of the measured coordinates, the equations become

$$y_0 = \left(\frac{\zeta}{DM - \zeta}\right) A', \tag{20}$$

$$x = x'_b \left(1 + \frac{y_0}{A'}\right) \frac{m}{M} - m \frac{y_0}{A'} X_b , \tag{21}$$

$$z = z'_b \left(1 + \frac{y_0}{A'}\right) \frac{m}{M} - m \frac{y_0}{A'} Z_b , \tag{22}$$

where $\zeta = x'_b - x'_t$. The origin of the coordinate system was chosen so that $y = t - y_0$, where t is the distance between the near and far fiducial planes. The constants in Eqs. (20) - (22) were calculated from the known distances between fiducials.

Equations (20) - (22) were used to derive approximate expressions for the distance between two points in the chamber.

These are

$$y_2 - y_1 = \left(- \frac{\zeta_2}{DM - \zeta_2} + \frac{\zeta_1}{DM - \zeta_1}\right) A' \approx \frac{-DMA'\Delta}{(DM - \zeta_2)^2} , \tag{23}$$

where

$\Delta = \zeta_2 - \zeta_1$, and

$$x_2 - x_1 = (x'_{b2} - x'_{b1}) \left(1 + \frac{y_{02}}{A'}\right) \frac{m}{M} , \tag{24}$$

$$z_2 - z_1 = (z'_{b2} - z'_{b1}) \left(1 + \frac{y_{02}}{A'}\right) \frac{m}{M} , \tag{25}$$

which correspond to neglecting terms of relative order Δ. The ζ_2 and Δ were measured directly by projecting both views simultaneously, superposing the images of Point 2, and then measuring the distance (Δ), between the two images of Point 1. The approximate equations above were used because the sign of Δ was not normally determined.

2. Track Reconstruction

By making use of Eqs. (23) - (25) it is relatively simple to calculate the spatial angles of a track. Let

α = dip angle, the angle between the track (at its origin) and the x, z plane,

$\bar{M}$ = magnification at center of the chamber,

s = projected track length between Point 1 and Point 2,

θ = projected angle of the track (at its origin) with the z axis in the x, z plane,

θ_R = polar angle of the track at its origin,

ϕ_R = azimuthal angle of the track at its origin.

Then, $\tan \alpha = (y_2 - y_1) / (s/\bar{M})$, (26)

while θ_R and ϕ_R may be obtained from the relations

$$\cos \theta_R = \cos \alpha \cos \theta, \tag{27}$$

$$\tan \phi_R = \tan \alpha / \sin \theta. \tag{28}$$

True radius of curvature, ρ_T, and range, R_T, can be calculated from the projected values as follows:

$$\rho_T = (\rho / \bar{M}) \sec \alpha, \tag{29}$$

$$R_T = (R/\bar{M}) \sec \alpha. \tag{30}$$

Little error is introduced by using $\bar{M}$ in place of the actual magnification for each track.

D. Procedure

1. Scanning

a. Types of Events Recorded

Three basic processes contributed the bulk of photon interactions that produced events visible in the photographs. They were the Compton effect, pair production, and triplet production.

All single electrons originating in the chamber were considered to be Compton electrons and were not recorded or measured, except in the rare instances when the electron underwent an unusual interaction before leaving the chamber, e.g., pair production by an electron.

For the purposes of event identification, it was necessary to use the phenomenological categories labeled "apparent pair" and "apparent triplet" (usually called just "pair" and "triplet," for brevity, throughout most of this dissertation). This was because many actual triplets had recoils too short to be seen in the bubble chamber and were thus indistinguishable from pairs. And, on the other hand, some actual pairs were indistinguishable from triplets by virtue of a delta ray or a Compton electron very near the origin.

All the film was scanned for triplets, which were subsequently measured. An equal number of pairs was desired and these were obtained from only 13 rolls of film, since their numbers were greater. The pairs in the remaining film were not recorded.

In addition to the pairs and triplets, two other types of events were particularly searched for. The first, two negative electrons with a common origin, could be interpreted as a triplet with a positron too short to be seen, a double Compton effect, or a Compton electron with a delta ray very near the origin (most likely). The second type of event was double pair creation. It could be identified by the four or five tracks with a common origin, corresponding to pair creation in the nuclear field, or electron field, respectively.

The scanners also recorded, in general, any unusual-appearing events, e.g., positron annihilation in flight, bremsstrahlung, pair creation by electron, etc.

Each event was designated by a roll number, frame number, z'_b coordinate, ζ measurement (y coordinate), and a two-digit descriptive code, which went on the IBM card along with the various track measurements. The code description not only specified the type of event but also indicated whether or not the identification was positive and whether there was an important comment recorded on the scan sheets that could not be placed on the IBM card. This facilitated sorting out events that needed to be rechecked or were unacceptable to the computer program.

b. Criteria for Acceptance of Events

The only quantitative criterion for the acceptance or rejection of events was based upon their position in the chamber. The beam entrance and exit in the chamber were located at $z'_b = -10$ cm and $z'_b = 30$ cm (projected), respectively. Owing to imperfect optical lighting near the entrance, and the need to have tracks long enough for an accurate curvature measurement, only those events were accepted for complete measurement and analysis whose origins lay in the region $-7 \leq z'_b \leq 20$ cm. This corresponded to a mean length of 6.52 cm in the chamber. In order to improve the statistics in the recoil momentum distribution, triplets were also accepted in the interval $20 \leq z'_b \leq 25$ cm. However, only the recoil electron was measured, making the photon energy indeterminate.

The scanners were instructed to label an event as questionable if they felt that there was the slightest possibility of a second interpretation. The result of this policy was that approximately 20% of the events were so designated. All questionable events were closely scrutinized by a physicist. Approximately 1% of the events could not be uniquely identified. Because many triplets had extremely short recoils the most common ambiguity was whether an event was a pair or a triplet.

Individual frame rejection on the basis of improper operating conditions or beam intensity for particular pulses was a minor problem. Only twenty frames were rejected for this reason. Several complete

rolls of film were rejected, however. The rejection of complete rolls, or a continuous portion of a roll, eliminated the possibility of biasing the data through the process of frame rejection.

c. Checking Procedure

All the usable film was systematically scanned at least two times. The first scan was done by using the projection table. Each event was measured as it was found and the identifying data, comments, and measurements were dictated into a tape recorder. The same person later transcribed the information onto permanent data forms made especially for recording the measurements. The data forms were designed for easy use by IBM key-punch operators: one IBM card per line per event.

The second scan was performed independently by a different person who used the stereoscopic viewer. The stereoscopic viewer had the advantage of allowing rapid scanning and depth perception, but lacked the magnification necessary for the examination of fine details required for some events. Consequently, a magnifying lens was used occasionally to inspect the film directly.

After the first and second scans were completed the scan sheets were cross-checked. Discrepancies in identification of events were rechecked and additional events found on the second scan were measured. Then the completed data forms were thoroughly checked to ensure that all the necessary measurements had been made and that there were no obvious errors in recording the data. This, and a similar check by the computer program, was the only over-all quality control applied to the events, since it was impractical to measure them all twice. However, a selected group of 115 events was measured independently by four persons and their results were used to determine the accuracy of measurement, which is discussed in Sec. V.E.

2. Method of Measurement

a. Curvature

The projected radius of curvature ρ_+, ρ_-, or ρ_R of each track of an event was measured whenever possible by means of templates provided for the purpose. The templates consisted of a set of curves drawn

on white cardboard. The radii of curvature of the templates were at 10% intervals in the range $2.7 \leqslant \rho \leqslant 483$ cm. and at 0.2-cm intervals in the range $0.3 \leqslant \rho \leqslant 2.7$ cm. Interpolation between templates was not possible on most of the measurements because of the effects of multiple Coulomb scattering and turbulence in the liquid hydrogen.

The entire length of a larger-radius track was used in the measurement unless scattering or turbulence in the chamber prohibited a good fit. Then a shorter section was used. The smaller-radii tracks --vis., those tracks that which underwent a deflection of 90 deg or more in the chamber-- were significantly affected by ionization energy loss from beginning to end. Consequently, measurement was restricted usually to the first 90 deg of deflection, but measurement out to 180 deg was necessary on the very-small-radius tracks.

b. Range

The projected range R_R was measured for all recoil electron tracks that had a projected radius of curvature $\rho_R \leqslant 2$ cm. Many of the electron trajectories in this region were severely affected by scattering and energy loss. A flexible string was laid along the track and then its length was measured with a ruler. The measurer indicated on the data form which measurement, ρ_R or R_R, was the more accurate, and that value was used in the calculation of the recoil momentum, P_R.

c. Angle

The projected angle of a recoil electron, θ, was obtained by placing the appropriate template along the track in such a way that a radius line intersected the curve at the origin of the track. Then a protractor was used to measure θ, the angle between the radius and the x axis. The angle was defined to be negative in the sense indicated by a vector in the plus y direction. The x direction was established from the fiducial marks. If ρ could not be measured, the template was replaced by a straight line parallel to the track at its origin.

In order to determine the dip angle α, it was necessary to measure three lengths: ζ_2, Δ, and @ or s (ζ_2 and Δ are defined in Sec. IV. C. 1). For their measurement, the origin of the event was

chosen to be Point 2. When ρ was measured, @ was measured; @ was defined as the chord of the arc between Point 2 and Point 1. Then s was calculated from the relation

$$s = 2\rho \tan^{-1}\left(\frac{@}{\sqrt{4\rho^2 - @^2}}\right).$$

When ρ was not measured, s was measured directly, instead of @ .

d. Location

The z_b' coordinate of the origin of each event was measured, as well as ζ_2. These two values permitted the calculation of y and z. The x coordinate was not needed in the analysis of the data.

e. Magnification

The chamber-to-projection-table magnification was determined from the measurement of the projected fiducial separations. It remained constant throughout the course of the measurements. The magnification factors were

$$M(\text{near fiducial plane}) = 4.352,$$

$$\bar{M}(\text{center of chamber}) = 4.142.$$

V. ANALYSIS OF DATA

A. Spectrum

1. Schiff Spectrum

The distribution in energy of the radiation from the synchrotron is closely approximated by the intrinsic integrated spectrum of Schiff.[31] The Schiff spectrum was obtained from the integration of the Bethe-Heitler differential bremsstrahlung cross section[32] over the angles of the scattered electron and photon. Screening was taken into account through the assumption of an atomic potential $(Ze/r) \exp(-r/a)$. The spectrum is shown as Curve B of Fig. 14.

2. Modifications due to the Target and Collimators

The Schiff spectrum was corrected where necessary to take into account the following eight effects:

(1) the failure of photons radiated at large angles to reach the bubble chamber,

(2) multiple scattering of electrons in the target before bremsstrahlung,

(3) deviation from the Born approximation,

(4) approximate form of the atomic potential,

(5) ionization energy loss before bremsstrahlung,

(6) increased path length in the target,

(7) bremsstrahlung by electrons of degraded energy due to previous bremsstrahlung,

(8) absorption of radiated photons in the target.

The net effect of these corrections was small. A discussion of them follows. (1) Schiff integrated over all photon angles. However, in this experiment the half angle subtended by the primary collimator was 0.0011 radian, or 0.69 mc^2/E_0. Since the high-energy component of the spectrum is relatively more intense in the forward direction, the effect of the collimator was to harden the beam somewhat. (2) Multiple scattering changes the direction of the electron and allows photons radiated at larger angles to pass through the collimator. This makes the collimated beam more nearly like the integrated spectrum.

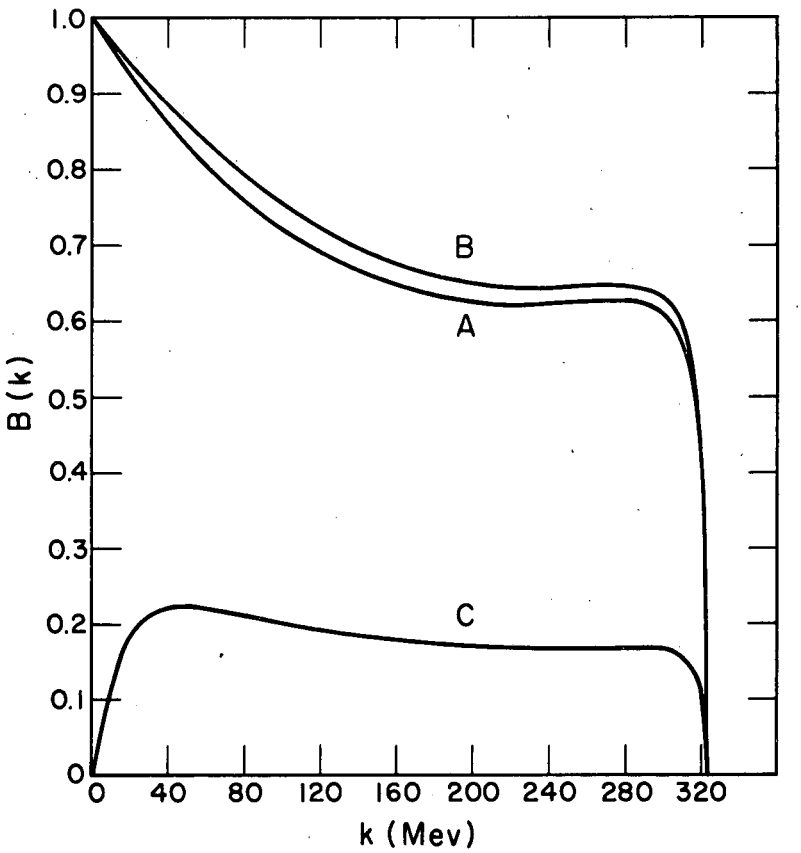

MU-21590

Fig. 14. The energy spectrum of the photon beam. Curve A is the primary spectrum $B_p(k)$, Curve B is the Schiff spectrum, $B_s(k)$, and Curve C is the incident spectrum $B_i(k)$.

The effect of (1) and (2) has been calculated quantitatively by Hisdal for energies from 10 Mev to 300 Mev and platinum target thicknesses from 0.5 mil to 50 mils.[33] The correction factor for this experiment was obtained by extrapolation of his results to 323 Mev and interpolation at a platinum thickness of 20 mils. The results are shown in Curve A of Fig. 15. It should be noted that his calculation assumed a half angle of mc^2/E_0. Therefore the correction factor might be underestimated for this experiment. (3) The intrinsic differential cross section for bremsstrahlung has been calculated by Bethe and Maximon without the use of the Born approximation.[34] They showed that the Coulomb correction is important only for small momentum transfer and is negligible when the angle of emission is less than mc^2/E_0. (This is opposite to pair production, in which the Coulomb correction is important for large momentum transfer and is consequently independent of screening.) No correction was necessary for this experiment. (4) R. Christian has calculated the spectrum for E_0 = 322 Mev, using the more accurate Fermi-Thomas model of the atom.[35] His results were used to obtain a correction factor to the Schiff spectrum, which is shown as Curve B of Fig. 15.

Effects (5) through (8) have been treated by Wilson for the case of no collimator.[36] In order to apply his results to this experiment it is necessary to calculate the effective target thickness due to the collimator and multiple elastic scattering. Since most of the bremsstrahlung has an angle less than mc^2/E_0 radians, it is reasonable to say that when the "rms" scattered angle θ_{rms} reaches a value of $3\ mc^2/E_0$, most of the subsequent radiation will fail to reach the collimator. The "rms" scattered angle is given by[37]

$$\theta_{rms} = Z \frac{21.2(\text{Mev})}{pv} \sqrt{\frac{L}{L_{rad}}} (1 + \epsilon), \tag{32}$$

where $Z = 1$, $pv = E_0 = 323$ Mev, $L_{rad} = 111$ mils, $(1 + \epsilon) = 0.8$, and L is the effective target thickness in mils. We choose

$$\theta_{rms} = 3\ mc^2/E_0 \tag{33}$$

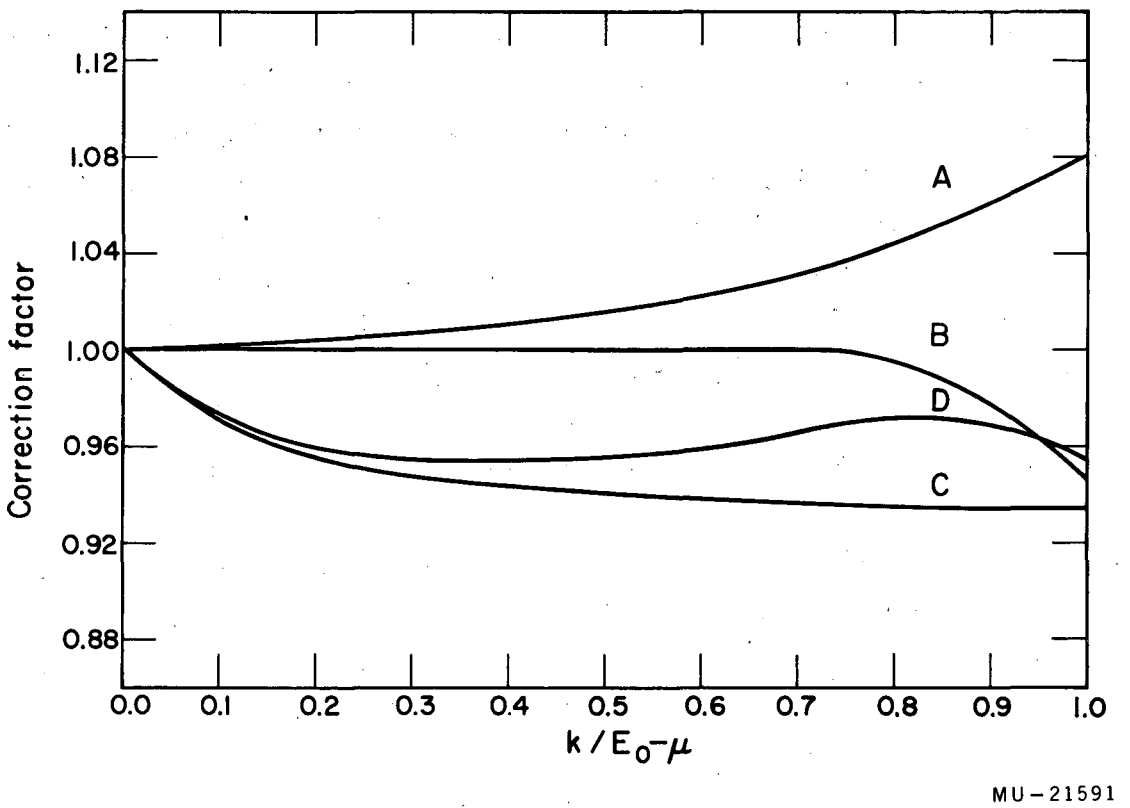

Fig. 15. Correction factors for the Schiff spectrum. Curve A is due to multiple Coulomb scattering in the target, and the finite collimator size; Curve B is due to Fermi-Thomas screening; Curve C is due to absorption of photons in the target; and Curve D is F(k), the product of Curves A, B, and C.

and calculate L = 0.9 mil or 0.008 radiation length. Thus the effect of multiple scattering and the collimator is to limit the accepted radiation to that coming form the front of the target. Wilson has shown that for target thicknesses less than 0.1 radiation length the effects of ionization losses, extra path length, and radiation losses become negligible. Consequently, the only remaining correction of importance is that due to absorption of photons in the target. For this experiment, the whole target was considered to act as an absorber, since a few mils change in effective target thickness does not appreciably affect the shape of the spectrum. This correction is shown as Curve C of Fig. 15.

The net correction factor F(k) for the Schiff spectrum is the product of the factors given by Curves A, B, and C, and is shown as Curve D of Fig. 15. Note that the curves have been normalized to unity at k = 0.

When the Schiff spectrum, $B_s(k)$, is corrected as described above, one obtains the "primary spectrum," $B_p(k)$, i.e., the spectrum passed by the primary collimator. This is shown as Curve A of Fig. 14, and was obtained from the relation $B_p(k) = F(k) \cdot B_s(k)$.

3. Incident Spectrum

The "incident spectrum," $B_i(k)$--i.e., the energy spectrum of the hardened photon beam incident on the bubble chamber--is the product of the primary spectrum and the transmission factor of the material in the beam path:

$$B_i(k) = T(k) \cdot B_p(k).$$

$B_i(k)$ is shown as Curve C in Fig. 14.

The normalized areas under the curves for $B_i(k)$ and $B_p(k)$ are, respectively, 0.1778 and 0.6945. Thus the reduction factor of the total energy in the primary spectrum due to the material in the beam path is the ratio of these two numbers and is 0.2560.

In order to calculate an absolute total cross section using the monitor data, one needs to know the number of quanta, $N(k_1, k_2)$, in the chosen energy range, $k_1 < k < k_2$, per Mev of energy in the primary spectrum. $N(k_1, k_2)$ was calculated graphically for various values of k_1 and k_2, by using the relation

$$N(k_1, k_2) = \int_{k_1}^{k_2} (1/k)B_i(k)\, dk \Big/ \int_0^{323} B_p(k)\, dk. \qquad (34)$$

The average photon energy in the incident spectrum was found to be

$$(0.2560)/N(0,323) = 80.6 \text{ Mev}.$$

The calculated values of $B_s(k)$, $F(k)$, $B_p(k)$, $T(k)$, $B_i(k)$, and $N(k_1, k_2)$ are given in Table IV.

B. Kinematics of Triplet Production

A typical triplet event in the bubble chamber consists of an electron-positron pair whose energies E_+ and E_- are very much greater than mc^2, and a "recoil" electron with momentum P_R, of order mc.

The recoil angular distribution has not been calculated. However, Votruba[6] has shown that the maximum angle of recoil $\theta_{R\,max}$ is given by the relation $\cos(\theta_{R\,max}) = 2\sqrt{mc^2/k}$. Also, if it is assumed that one of the pair members is always produced at zero degrees, the resulting two-body problem yields the relation $\cos\theta_R \approx (\sqrt{P_R^2 + (mc^2)^2} - mc^2)/P_R$. A similar equation is satisfied by the second pair member.

Hart et al.[14] have shown that the distribution of the opening angle between the pair members is substantially the same as that for nuclear pairs, for which Borsellino[38] has calculated the most probable opening angle to be of the order $4\, mc^2/k$.

Table IV

Calculated values of $E_0 - mc^2 = 323 \pm 2$ Mev

$k/(E_0-mc^2)$	$B_s(k)$	$F(k)$	$B_p(k)$	$k/(E_0-mc^2)$	$T(k)$	$B_i(k)$	$k_1 - k_2$	$N(\times 10^{-7})$
0.05	0.9513	0.9853	0.9373	0.0031	0.0004	0.0004	0 - 1	17.7
0.10	0.9062	0.9735	0.8822	0.0063	0.0046	0.0046	1 - 2	72.7
0.15	0.8648	0.9652	0.8347	0.0156	0.0410	0.0402	2 - 4	415.4
0.20	0.8270	0.9595	0.7935	0.0313	0.1113	0.1069	4 - 8	1525
0.25	0.7929	0.9561	0.7581	0.0469	0.1624	0.1529	8 - 12	1879
0.30	0.7624	0.9545	0.7277	0.0625	0.1953	0.1802	12 - 16	1857
0.35	0.7354	0.9543	0.7018	0.0938	0.2360	0.2098	16 - 20	1686
0.40	0.7121	0.9541	0.6794	0.1250	0.2550	0.2187	20 - 24	1516
0.45	0.6923	0.9548	0.6610	0.1563	0.2656	0.2202	24 - 28	1370
0.50	0.6761	0.9557	0.6461	0.1875	0.2706	0.2173	28 - 32	1240
0.55	0.6632	0.9570	0.6347	0.2500	0.2795	0.2119	32 - 36	1121
0.60	0.6538	0.9589	0.6269	0.3125	0.2808	0.2023	36 - 40	1018
0.65	0.6476	0.9618	0.6229	0.3750	0.2804	0.1935	40 - 48	1783
0.70	0.6444	0.9655	0.6222	0.4375	0.2794	0.1858	48 - 56	1510
0.75	0.6437	0.9693	0.6239	0.5000	0.2780	0.1796	56 - 64	1302
0.80	0.6449	0.9717	0.6266	0.5625	0.2765	0.1747	64 - 72	1136
0.85	0.6461	0.9715	0.6277	0.6250	0.2750	0.1719	72 - 80	1001
0.90	0.6421	0.9688	0.6221	0.6875	0.2735	0.1702	80 - 92	1300
0.91	0.6396	0.9680	0.6191	0.7500	0.2722	0.1699	92 - 108	1448
0.92	0.6358	0.9669	0.6148	0.8125	0.2709	0.1701	108 - 132	1736
0.93	0.6303	0.9658	0.6087	0.8750	0.2697	0.1688	132 - 160	1582
0.94	0.6224	0.9647	0.6004	0.9063	0.2691	0.1671	160 - 188	1269
0.95	0.6106	0.9630	0.5880	0.9375	0.2685	0.1622	188 - 216	1064
0.96	0.5928	0.9619	0.5702	0.9688	0.2680	0.1462	216 - 256	1288
0.97	0.5643	0.9601	0.5418	0.9844	0.2677	0.1226	256 - 323	1643
0.98	0.5148	0.9585	0.4934	0.9922	0.2676	0.0962	0 - 323	31,760
0.99	0.4145	0.9563	0.3964					
1.00	0.0378	0.9540	0.0361					

That the pair members were produced at small angles simplified the measurements greatly. It was not necessary to measure the dip angle α except in a few cases. This was not true for the recoils.

By use of the true radius of curvature, ρ_T, obtained from Eq.(29), and the magnetic field H, the momenta of the particles were calculated from the relation

$$cP = 0.300\ H\rho_T\ (\text{Mev}/c = \text{kG} \times \text{cm}). \tag{35}$$

The photon energy k was obtained from the energy-conservation relation

$$k = E_+ + E_- + E_R - mc^2. \tag{36}$$

The energies of many of the less energetic recoil particles were determined from range measurements. In this case the energies were obtained by interpolation in the tables of Nelms.[39]

The method of calculating the recoil angle was described in Sec. IV.C.2.

C. Cross-Section Calculations

When the attenuation is small (it was less than 1% in this experiment), the number of events $n(k_1, k_2)$ produced in a photon energy interval $k_1 \leqslant k \leqslant k_2$ by a process with cross section $\Phi(k)$ is given by

$$n(k_1, k_2) = \tau W_p \int_{k_1}^{k_2} dk \cdot N_i(k) \cdot \Phi(k), \tag{37}$$

where τ = surface density (atoms/cm^2),

W_p = total energy in the primary spectrum (Mev),

$N_i(k)$ = number of incident photons of energy k, per Mev of photon energy, per Mev of energy in the primary spectrum,

and $\int_{k_1}^{k_2} dk \cdot N_i(k) = N(k_1, k_2)$, defined in Sec. V.A.3.

The experimental cross section was defined as the average

$$\Phi^{exp}(k) = \int_{k_1}^{k_2} dk \,.\, N_i(k) \,.\, \Phi(k) \Big/ \int_{k_1}^{k_2} dk \,.\, N_i(k). \tag{38}$$

For the purposes of calculation, this can be more conveniently expressed, by using Eq. (37), in the form

$$\Phi^{exp}(k) = n(k_1, k_2)/\tau\, W_p\, N(k_1, k_2). \tag{39}$$

Similarly, for a differential cross section (e.g., the recoil momentum distribution), the number of events $n(k_1, k_2, P_{R1}, P_{R2})$ produced in a photon energy interval $k_1 \leqslant k \leqslant k_2$ and recoil momentum interval $P_{R1} \leqslant P_R \leqslant P_{R2}$ by a process with a differential cross section $\Phi(k, P_R)$ is given by

$$n(k_1, k_2, P_{R1}, P_{R2}) = \tau\, W_p \int_{k_1}^{k_2} dk. \left[N_i(k) \int_{P_{R1}}^{P_{R2}} dP_R \,.\, \Phi(k, P_R) \right]. \tag{40}$$

In this case, the experimental cross section was the average

$$\Phi^{exp}(k, P_R) = \int_{k_1}^{k_2} dk. \left[N_i(k) \int_{P_{R1}}^{P_{R2}} dP_R \,.\, \Phi(k, P_R) \right] \Big/ \left[\int_{k_1}^{k_2} dk. N_i(k) \right] . \left[\int_{P_{R1}}^{P_{R2}} dP_R \right], \tag{41}$$

or, more conveniently,

$$\Phi^{exp}(k, P_R) = n(k_1, k_2, P_{R1}, P_{R2})/\tau\, W_p\, N(k_1, k_2) \,.\, (P_{R2} - P_{R1}). \tag{42}$$

The surface density is given by

$$\tau = N_0\, \rho_H\, (z_2 - z_1)/A, \tag{43}$$

where N_0 = Avogadro's number (6.0249×10^{23} atoms/mole),
ρ_H = density of hydrogen (0.0586 g/cc), discussed in Sec. V. F.,
$(z_2 - z_1)$ = effective path length in the bubble chamber,
A = atomic weight of hydrogen (1.008).

The quantity $(z_2 - z_1)$ was evaluated in terms of the projected path length $(z'_{b2} - z'_{b1})$ by means of Eq. (25). Because the proportionality factor varied less than ±2%, according to the depth of the event in the chamber, an average value was used, so that one could write

$$z_2 - z_1 = 0.242 \times (z'_{b2} - z'_{b1}). \tag{44}$$

In Sec. II. G. 2 the energy W_p in the primary spectrum was shown to be

$$W_p = (5.04 \times 10^9) \times (\text{"No. dumps"}) \text{ Mev}, \tag{45}$$

a dump being a "practical" unit of measure used during the experiment to record the integrated current from the Cornell-type ionization chamber.

Owing to variation in the bubble chamber operating conditions throughout the course of the experiment, the scannable path length was not the same for all rolls of film. Consequently it was necessary to evaluate the product τW_p for each roll individually and then to sum the products when combining the data. Thus, the quantity τW_p was calculated from the relation

$$\tau W_p = \sum_{\text{rolls}} (\tau W_p)_i = (4.275 \times 10^{31}) \cdot \sum_{\text{rolls}} (z'_{b2} - z'_{b1})_i \cdot (\text{"No. dumps"})_i . \tag{46}$$

D. Scanning Efficiency

1. Human Detection Efficiency

Two aspects of the event-detection efficiency of the scanners were examined. First of all, it was felt that the detection efficiency might depend on the position in the chamber of the origin of the events, those events nearer the entrance being more susceptible of detection because of their longer visible track length. To test this possibility, a group of 4659 events was used to make a plot of the relative number of events per unit length versus six intervals of the z coordinate, shown in Fig. 16. The points in the figure are normalized so that their weighted average is equal to unity. The fit is good ($\chi^2 = 2.25$), indicating no dependence on the z coordinate. The dashed line in the same figure is the best two-parameter fit, and has an average value 3.83%, below its maximum value at the entrance, with the expected trend toward the exit. This suggests that the absolute scanning efficiency was no greater than 96.17%. However, that value was not accepted because of the good one-parameter fit (unity) and the knowledge from other considerations that the scanning efficiency was greater.

The other aspect considered was the effect of the scanning efficiency on the calculated cross sections. If n_1 and n_2 are the numbers of events found by the first and second scans, respectively, and n is the net number of events found, then the net scanning efficiency ϵ is given by

$$\epsilon = n(n_1 + n_2 - n)/n_1 n_2. \tag{47}$$

This relation assumes that all events have the same probability of being missed.

A third of the film had been scanned for all events, in order to obtain a total pair-plus-triplet cross section. The scanning efficiency ϵ_{p+t} for this group of events, from a comparison of two independent scans, was found to be

$$\epsilon_{p+t} \geqslant 99.5\%. \tag{48}$$

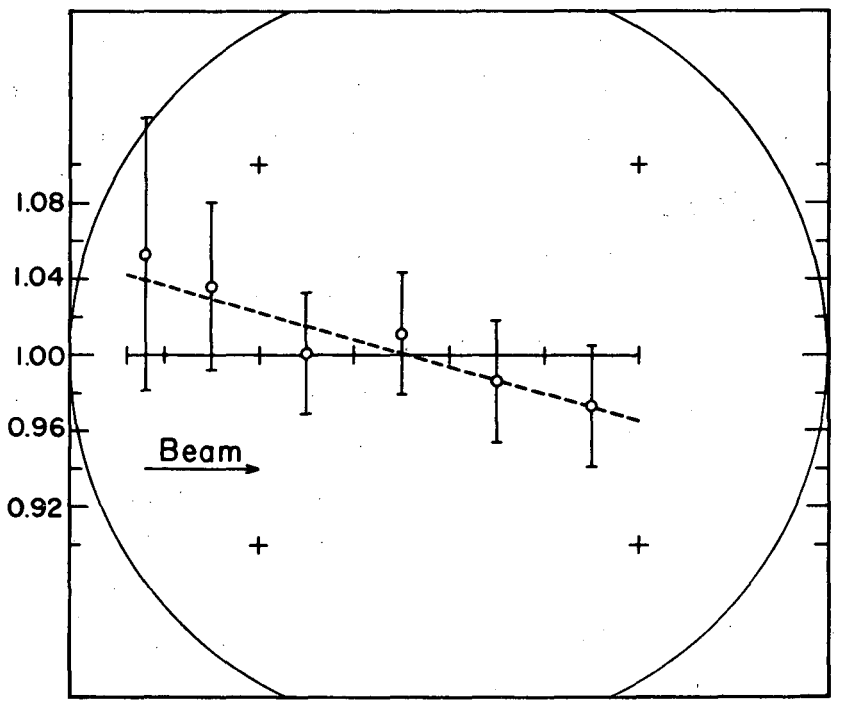

MU-21592

Fig. 16. Distribution of events according to distance from the bubble chamber entrance, normalized to an average value of 1.00. The dashed line is the best fit, but the solid line is more consistent with the known scanning efficiency.

Similarly, the scanning efficiency ϵ_t for the remainder of the film, which was scanned only for triplets, was found to be

$$\epsilon_t \geqslant 99\%. \tag{49}$$

Unfortunately, the data were insufficient to make a useful analysis of the scanning efficiency as a function of photon energy or of the various differential-cross-section variables P_R, θ_R, etc.

2. Spurious Events

Pair production in the field of an electron can be simulated by three other kinds of events. These events and their contributions to the experimental triplet cross section are discussed below.

For this experiment, the least important type of spurious event was created by the accidental coincidence of the origins of an electron-positron pair and a Compton recoil electron. This type of event was estimated to contribute less than 0.2% to the triplet cross section. Two factors were responsible for this small value. One was the reduction, by the lithium hydride, of the relative number of low-energy photons, which were the principal source of Compton electrons. The other was the operation of the synchrotron at a low level of beam intensity so that, on the average, there were only 1.4 pairs or triplets in each picture.

The next type of event to be considered, the "electron pair," belies the name "triplet," for its signature in the bubble chamber was made by two electrons with a common origin. However, electron pairs must be considered because it was possible for a triplet to have a zero-momentum positron. An electron pair could also be created by a delta ray near the origin of a Compton electron, or by two Compton electrons in close proximity. The latter occurrence was the least important and is not discussed.

The number of electron pairs found was equal to 5% of the number of triplets ($P_+ \neq 0$). This frequency of occurrence of electron pairs may be completely explained on the basis that they were all produced by delta rays on Compton electrons. This conclusion was derived

from the results of a delta-ray count described later in this section. Consequently, there was no contribution of this type of event to the experimental triplet cross section.

The combination of an electron-positron pair plus a delta ray near the origin produced a type of spurious event which contributed significantly to the experimental triplet cross section. The magnitude of the "pair-plus-delta-ray" cross section Φ_{p+d}, which must be subtracted from the experimental triplet cross section, was determined from the results of a delta-ray count, which is described below.

The individual tracks of a random group of 163 pairs were scanned for delta rays occurring in a selected region near, but not including, the origin. In a total track length (D) of 788 cm, 105 delta rays (n), were found and measured in the same fashion as recoil electrons. If one lets d be the distance from a pair origin within which a delta ray is indistinguishable from a true recoil electron, then the ratio of the "pair-plus-delta-ray" cross section to the experimental triplet cross section is given by the relation

$$\Phi_{p+d}/\Phi_t^{exp} = \frac{(2n/L)d}{1 - (2n/L)d} \cdot \bar{R} . \tag{50}$$

The factor of two is necessary because the delta ray may be on either pair member; and $\bar{R}$ represents the average experimental pair-to-triplet ratio, which was equal to 3.4±0.1. A reasonable value of d was chosen as 0.0484±0.0121 cm (2.0±0.5 mm in projector space), resulting in the value, from Eq. (50), of

$$\Phi_{p+d}/\Phi_t^{exp} = (4.48\pm1.65)\times10^{-2} . \tag{51}$$

The delta rays, of course, had no effect on the total pair-plus-triplet cross section.

Several other items of useful information were obtained from the delta-ray measurements. The experimental delta-ray momentum distribution is shown in Fig. 17, along with the theoretical distribution given by Heitler.[40] The fact that the experimental cross section is equal to one-half of the theoretical cross in the bin $0.22 \leqslant P_R \leqslant 0.32$ Mev/c

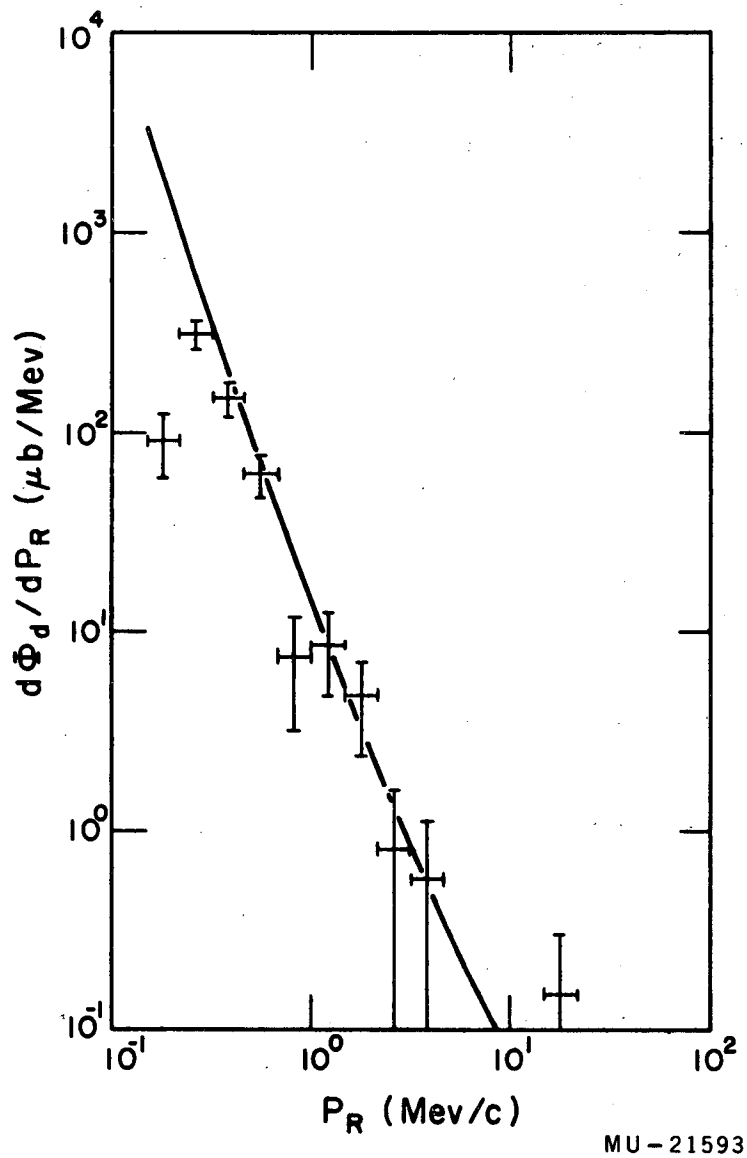

Fig. 17. Differential momentum distribution $d\Phi_d/dP_R$, of 105 delta rays; $2 \leqslant k \leqslant 323$ Mev. The curve is from electron scattering theory.

indicates that the detection efficiency for recoil electrons was not good in the region $P_R \leqslant 0.32$ Mev/c. This momentum corresponds to a range of approximately 1 mm in the bubble chamber.

The delta-ray data were not sufficient to determine the detection efficiency for recoil s with momentum less than 0.32 Mev/c. Therefore the delta-ray theory could be used only above this value to correct the experimental triplet recoil momentum distribution.

Comparison of theory with experiment also showed that the average minimum detectable recoil momentum, $\overline{P}_{R\ min}$, was 0.27±0.14 Mev/c.

3. Effective Path Length

Except for a few film rolls, the events used in the calculation of the absolute cross sections were taken from the region $-7 \leqslant z_b' \leqslant 20$ cm (projector space), for reasons given in Sec. IV. D. 1. b. The exceptions were due to local boiling in the bubble chamber, which occasionally restricted the useful region to a smaller range of z_b'.

It is necessary to know accurately the effective photon path in the chamber for use in the cross section calculation. The direction of the photon beam through the chamber was intended to coincide with the z axis of the chamber (defined in Sec. IV. C. 1.). This was checked by measuring event origins near the entrance and exit; they had the same average x and y coordinates. Therefore it was possible to use Eq. (25) to obtain the actual path length in the chamber. The relation between the projected length, $z_{b2}' - z_{b1}'$, and the actual path length, $z_2 - z_1$, is seen to depend on the y coordinate (distance from the camera). Since the dependence was linear, no accuracy was lost by using the average y coordinate. The resulting relation was

$$z_2 - z_1 = 0.242 \times (z_{b2}' - z_{b1}') . \tag{52}$$

E. Accuracy of Measurement

The accuracy of measurment was analyzed in order to aid in the selection of bin sizes to be used in the calculation of the various cross sections. The bins were generally made equal to, or larger than, the error in the argument of the cross section in question (e.g., k in $\Phi_t^{exp}(k)$). This served to minimize the effect of the resolution in measurement.

The root-mean-square error Δc in curvature measurement was determined from an analysis of 115 events, each of which was measured independently by four persons. The radii were converted into curvature ($c = 1/\rho$), and the mean curvature and the standard deviation of the mean were computed for each track.

If the difference between the curvatures of the templates were sufficiently small, one would expect Δc to be a constant, independent of c and equal to the minimum measurable curvature. However, if the template curvatures were spaced far enough apart to dominate the error, and furthermore, since they were approximately the same percentage apart, one would expect $\Delta c/c$ to be a constant, of the same order as the template spacing. The results of the curvature analysis showed that the first case was valid for momenta greater than 40 Mev/c, while the latter case was correct for momenta less than that value.

Expressed in terms of momenta, the results were

$$\begin{aligned} \Delta P/P &= 0.05 \text{ for } P < 40 \text{ Mev/c}, \\ \Delta P/P &= P/800 \text{ (Mev/c) for } P < 40 \text{ Mev/c}. \end{aligned} \tag{53}$$

It should be noted that the template with the smallest curvature corresponded to a largest measurable momentum of 259 Mev/c. From Eq. (53), the relative error on the measurement of such a momentum would be 32.4%. Obviously, the use of templates with smaller curvatures would have added little accuracy to the experiment, especially since only a small fraction of all the tracks measured had such large momenta.

The average relative error in the photon energy was calculated by using the approximation that the pair members divided the total energy in a random way. The result was

$$\Delta k/k = (8.4\times10^{-4})\times k \text{ (Mev)}. \tag{54}$$

The relative error reached its maximum value of 27% at the quantum limit energy (323 Mev).

F. Density of Hydrogen

It was necessary to know the density, ρ_H, of the liquid hydrogen in the bubble chamber in order to calculate the absolute cross sections. Reed and Tripp[41] have determined the operating density of the Alvarez 15-inch bubble chamber by means of a thermodynamic calculation, and from the measurement of the ranges of μ^+ mesons occurring in the $\pi^+ \rightarrow \mu^+ \rightarrow e^+$ decay chain. Their values were 0.05863 g/cc and 0.0588±.0006 g/cc, respectively.

The two bubble chambers had similar operating conditions, the 4-inch bubble chamber being operated 0.1°K warmer than the larger chamber. The density assumed for this experiment was

$$\rho_H = 0.0586\pm.0006 \text{ g/cc}. \tag{55}$$

G. Monitor Results

As explained in Sec. II. G, the Cornell-type thick-wall ionization chamber was the primary beam monitor. By means of the ion chamber, an electrometer, and an automatic recorder, a permanent record of the integrated beam intensity was obtained, which could be correlated later with the film strips.

The monitoring apparatus integrated every synchrotron pulse, at the rate of 360 per min. If p pictures were taken in a synchrotron running time of t minutes, then the fraction of the beam actually used was equal to p/360 t. Thus, the amount of beam used, D, is given by

$$D = (p/360\ t) \times C, \tag{56}$$

where C is the amount of beam recorded by the monitor.

The drift rate of the monitor apparatus was measured at periodic intervals throughout the course of the experiment. This was done by operating the monitor while the synchrotron beam was turned off. The drift rate was found to fluctuate about an average which was nearly constant for long periods of time (many rolls of film). However, uncertainty over the exact value of the drift rate during each particular run introduced a significant error into the results. The relative size of the drift correction to the monitor data was -9±1%.

The monitor data used in the calculation of the two cross sections Φ_t^{exp} and Φ_{p+t}^{exp} are given in Table V. In order to simplify the presentation, the results have been expressed in terms of the quantity $(z'_{b2} - z'_{b1}) \times$ (No. dumps) given in Eq. (46). There was included a 1% error in interpreting the permanent monitor record.

Table V.

Monitor results for calculation of Φ_{p+t}^{exp}	
$\Sigma(z'_{b2} - z'_{b1}) \times$ (No. dumps) (Uncorrected)	4.414±0.044 cm-dump
Drift Correction	-0.376±0.045
$\Sigma(z'_{b2} - z'_{b1}) \times$ (No. dumps) (Corrected)	4.038±0.063
Monitor results for calculation of Φ_t^{exp}	
$\Sigma(z'_{b2} - z'_{b1}) \times$ (No. dumps) (Uncorrected)	14.71±0.15 cm-dump
Drift Correction	-1.30±0.17
$\Sigma(z'_{b2} - z'_{b1}) \times$ (No. dumps) (Corrected)	13.41±0.23

The integrated beam intensity used in this experiment corresponds to an average energy in the incident spectrum of 4.0×10^4 Mev per synchrotron pulse. Or, expressed slightly differently, there were 124 equivalent (323-Mev) quanta per pulse. It is believed that this intensity could not have been appreciably increased without seriously contaminating the chamber with background tracks.

VI. RESULTS AND DISCUSSION

A. Cross Section for Visible Recoils

1. Relative Cross Section

The ratio of the experimental triplet and pair cross sections was calculated from the relation

$$\Phi_t^{exp}(k)/\Phi_p^{exp}(k) = (0.301 \pm 0.007) \times (T^*/P^*), \qquad (57)$$

where T* and P* were the observed numbers of triplets and pairs, respectively, and the constant was equal to the ratio of the monitor results for the two groups of events (determined from Table V). The results are given in Table VI and the ratio is plotted versus photon energy in Fig. 18. The quoted errors are standard deviations due to counting statistics and do not include the 2.3% error in the monitor ratio.

The ratio of the two cross sections is of particular interest because it is independent of several factors that contribute as sources of error for the cross sections individually, e.g., the shape of the spectrum, the monitor calibration (but not the other monitor errors), the density of hydrogen, etc.

The ratio is expected to be equal to zero at the threshold for triplet production ($k = 4\ mc^2$), and indeed this was so for the lowest-photon-energy bin ($4\ mc^2 \leqslant k \leqslant 4$ Mev). Inspection of Fig. 18 shows that the ratio is approximately constant between 4 Mev and 100 Mev, but decreases toward higher photon energies. The over-all ratio for all photon energies was found to be 0.291±0.0097.

2. Absolute Cross Section

The absolute experimental triplet cross section Φ_t^{exp} for detectable recoils was calculated, as well as the experimental cross section $\Phi_t^{exp}(P_R > Mc)$ for recoils with momentum greater than mc. The results are presented in Table VI and Fig. 19. All the errors given in Table VI are standard deviations due to counting statistics. The two triplet cross sections do not include an additional 3.4% error that was contributed

Table VI

Experimental triplet and pair cross section

k (Mev)	$\Phi_t^{exp}/\Phi_p^{exp}$	Φ_t^{exp} (mb)	$\Phi_t^{exp}(P_R>mc)$ (mb)	Φ_{p+t}^{exp} (mb)
1 - 4	-	-	-	0.5937±.2654
2 - 4	0	0	0	- -
4 - 8	.3012±.0908	0.2518±.0537	0.1373±.0396	0.9500±.1900
8 - 12	.3114±.0569	0.5666±.0725	0.3158±.0541	2.374 ±.2706
12 - 16	.2976±.0461	0.7800±.0856	0.3289±.0556	3.558 ±.3333
16 - 20	.3470±.0495	1.097 ±.1066	0.5797±.0775	4.503 ±.3936
20 - 24	.3170±.0454	1.151 ±.1151	0.6216±.0846	4.931 ±.4343
24 - 28	.3838±.0508	1.656 ±.1452	0.8025±.1011	5.880 ±.4987
28 - 32	.3702±.0509	1.661 ±.1528	0.9007±.1126	5.982 ±.5286
32 - 36	.3250±.0449	1.697 ±.1625	0.8095±.1123	6.876 ±.5961
36 - 40	.3461±.0507	1.714 ±.1714	1.046 ±.1339	7.059 ±.6342
40 - 48	.2858±.0279	2.007 ±.1402	1.057 ±.1017	9.297 ±.5497
48 - 56	.3250±.0339	2.207 ±.1597	1.156 ±.1155	9.170 ±.5932
56 - 64	.2901±.0324	2.104 ±.1679	1.152 ±.1243	9.744 ±.6586
64 - 72	.2992±.0343	2.336 ±.1895	1.368 ±.1450	10.41 ±.7287
72 - 80	.2989±.0365	2.337 ±.2019	1.273 ±.1490	10.19 ±.7684
80 - 92	.3272±.0333	2.698 ±.1903	1.503 ±.1420	11.10 ±.7032
92 - 108	.3154±.0304	2.663 ±.1792	1.422 ±.1309	11.17 ±.6683
108- 132	.2960±.0246	2.885 ±.1703	1.709 ±.1311	12.52 ±.6461
132- 160	.2987±.0272	2.659 ±.1712	1.401 ±.1243	11.10 ±.6378
160- 188	.2606±.0256	2.653 ±.1910	1.485 ±.1428	13.01 ±.7706
188- 216	.2135±.0215	2.757 ±.2127	1.526 ±.1583	15.86 ±.9296
216- 256	.2303±.0212	2.819 ±.1955	1.572 ±.1460	15.44 ±.8336
256- 323	.2498±.0210	2.741 ±.1706	1.360 ±.1201	14.07 ±.7044
No. triplets:	3445	3445	1859	1092
No. pairs:	3561			3561

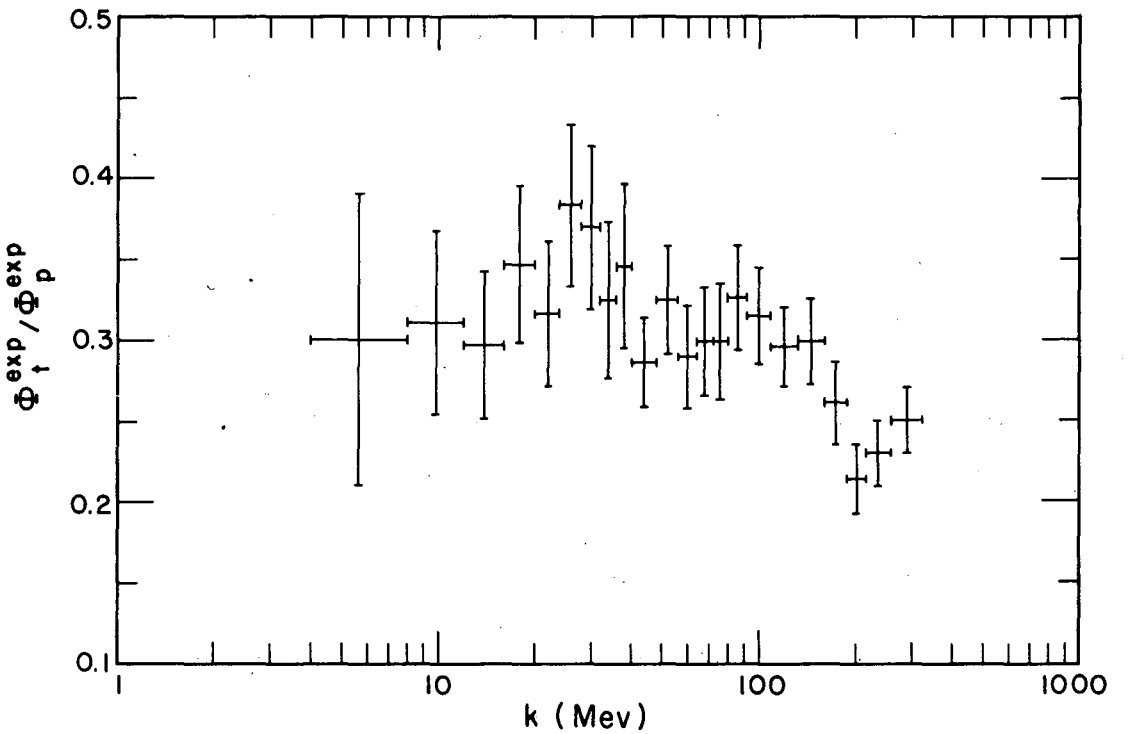

MU-21594

Fig. 18. The experimental triplet-to-pair ratio, $\Phi_t^{exp}/\Phi_p^{exp}$.

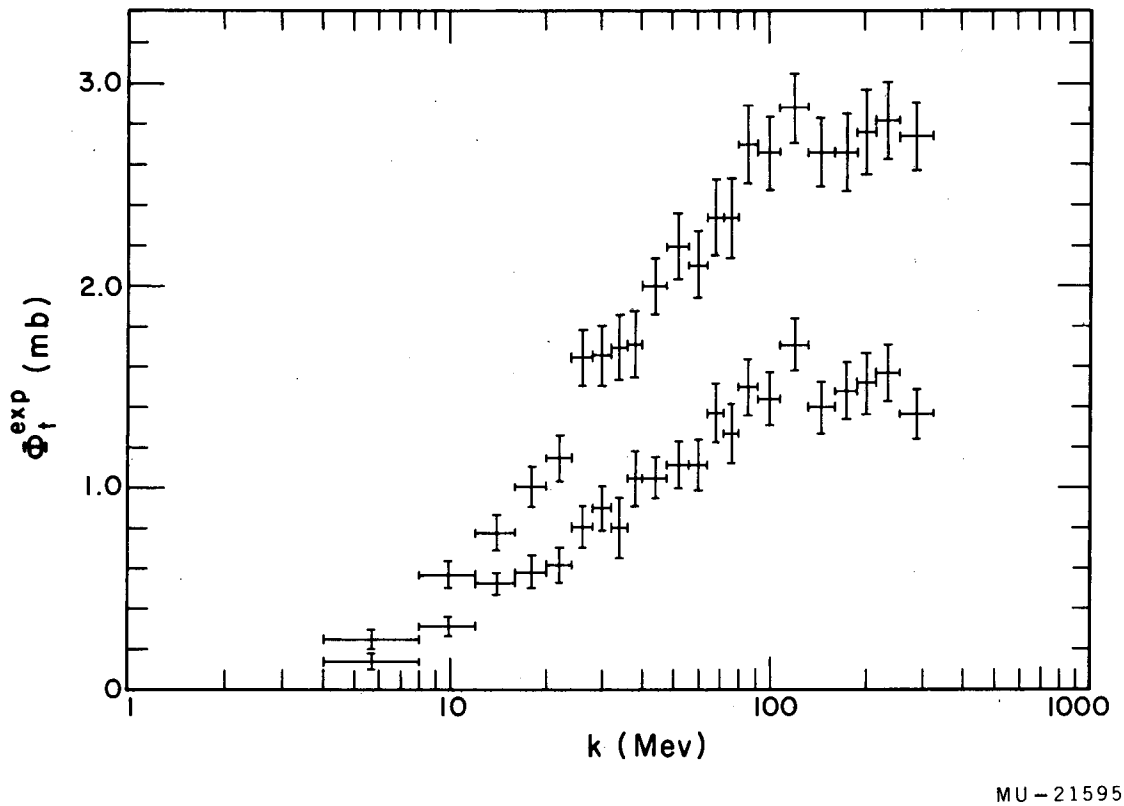

Fig. 19. The observed triplet cross section, $\Phi_t^{exp}(k)$ (upper points), and the cross section for recoils with momenta greater than mc, $\Phi_t^{exp}(k, P_R > mc)$ (lower points).

by the other quantities used in the calculations. Neither do they include the -4.48±1.65% delta-ray correction which must be applied at each energy.

The most notable feature of the behaviour of the two cross sections is their logarithmic increase up to a photon energy of 100 Mev, after which there is a definite leveling off. The leveling off of the triplet cross section above 100 Mev explains the decrease in the triplet-to-pair ratio in the same region. It may be understood qualitatively on the basis that as the photon energy increases, interactions at larger impact parameters (which produce smaller recoil momenta) contribute increasingly to the cross section. A point is finally reached where the increase in the cross section is primarily due to those impact parameters that result in undetectable, low-momentum recoils. Then the observed part of the cross section is seen to level off.

B. Total Cross Sections

1. Pair-Plus-Triplet Cross Section

The total triplet cross section $\Phi_t^{tot}(k)$ could not be obtained directly from this experiment, of course, because the minimum detectable momentum in the chamber was much greater than the minimum recoil momentum possible in triplet production. However, the combined experimental pair-plus-triplet cross section $\Phi_{p+t}^{exp}(k)$ was equal to the sum of the actual cross sections, $\Phi_p(k) + \Phi_t(k)$.

The cross section $\Phi_{p+t}^{exp}(k)$ is given in Table VI, as well as in Fig. 20. There is also at each energy a ±3.3% error due to errors other than counting statistics.

Also shown in Fig. 20 are the theoretical upper and lower limits on the triplet cross section, given in Eq. (5), to which has been added the theoretical pair cross section Φ_p^{BHscr}. The pair cross section was obtained by numerical integration of the exact (in Born approximation) Bethe-Heitler pair cross section,[1] corrected for screening in the relativistic region.[3] The theoretical limits are uncertain below 40 Mev because of the relativistic approximation in the triplet cross section. It is seen that they are in good agreement with this experiment.

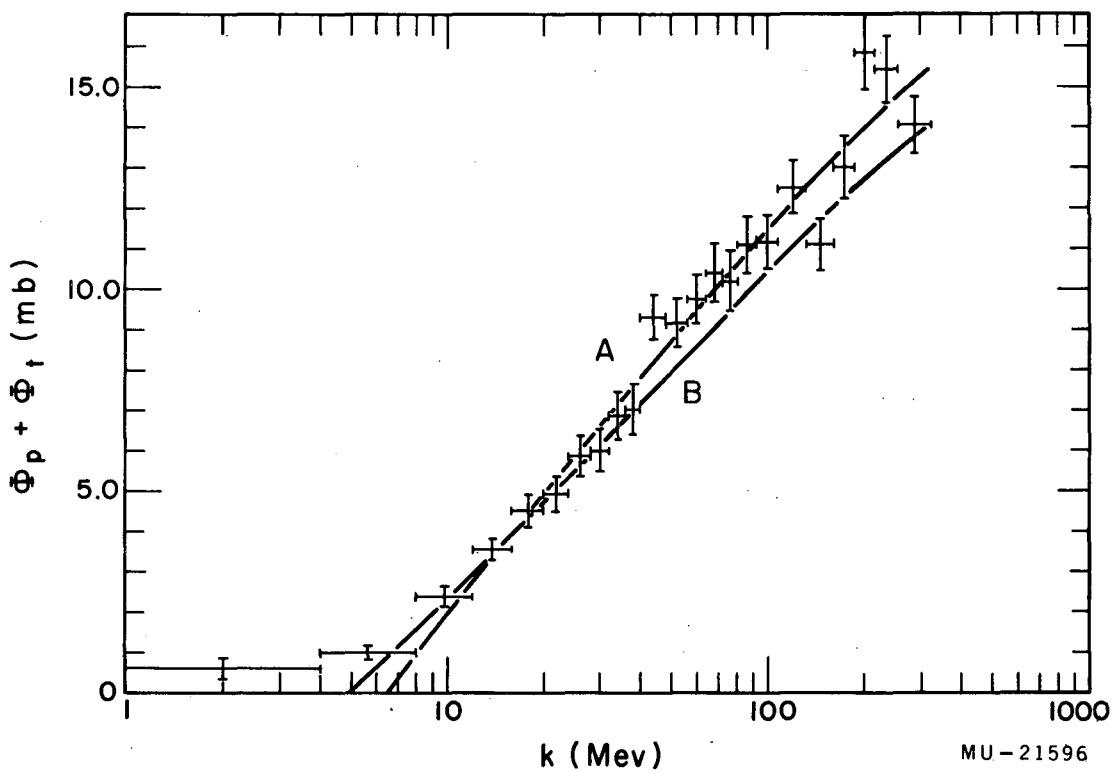

Fig. 20. The experimental triplet-plus-pair cross section, Φ_{p+t}^{exp}. Also shown are the sum of the Bethe-Heitler and Borsellino cross sections (Curve A) and the sum of the Bethe-Heitler and Votruba cross sections (Curve B), i.e., the theoretical upper and lower limits, respectively. The Wheeler-Lamb screening correction is included in the curves.

2. Triplet Cross Section

The total triplet cross section for this experiment was obtained from the relation

$$\bar{\Phi}_t^{tot} = \bar{\Phi}_{p+t}^{exp} - \bar{\Phi}_p^{BHscr}, \tag{58}$$

where $\bar{\Phi}_p^{BHscr}$ was the Bethe-Heitler pair cross section, averaged over the photon energy interval according to Eq. (38). The results are given in Table VII, along with the calculated values of $\bar{\Phi}_p^{BHscr}$ and the average photon energy, $\bar{k}$, for each interval of k. The quoted standard deviations include all sources of error.

The magnitude of the γ-e interaction and exchange terms was estimated by fitting the eighteen data points above 20 Mev to a cross section of the form

$$\bar{\Phi}_t = \bar{\Phi}_t^B - \left[\bar{\Phi}_p^{BHunscr}(Z = 1) - \bar{\Phi}_t^{WL}\right] - B(\alpha r_0^2)(mc^2/k)\ln(2k/mc^2), \tag{59}$$

where B was an adjustable parameter. The first three terms on the right-hand side of Eq. (59) are just the theoretical upper limit, given in Sec. I.A.2, i.e., Borsellino's cross section corrected for atomic screening. The last term is the approximate functional form due to the γ-e interaction and exchange terms, which Borsellino neglected.[7] The value of B found from a least-squares analysis was

$$B = 2.4 \pm 7.4 \tag{60}$$

The χ^2 value for the least-squares fit was 23.8. The curve given by Eqs. (59) and (60) is shown in Fig. 21 along with the triplet cross section obtained from Eq. (58), and $\bar{\Phi}_t^{WL}$.

This experiment found no evidence of the effect of the γ-e interaction and exchange terms, and is in agreement with the theory of Borsellino,[4] for energies above 20 Mev.

Table VII

Total triplet cross section

k (Mev)	$\bar{k}$ (Mev)	$\bar{\Phi}_p^{BHscr}$ (mb)	$\Phi_t^{tot} = \Phi_{p+t}^{exp} - \bar{\Phi}_p^{BHscr}$ (mb)
2 - 4	~2.8	0.50	0.09±0.27
4 - 8	~6	1.37	-0.42±0.19
8 - 12	10	2.12	0.26±0.28
12 - 16	14	2.61	0.94±0.35
16 - 20	18	3.06	1.45±0.42
20 - 24	22	3.40	1.53±0.46
24 - 28	26	3.68	2.20±0.54
28 - 32	30	3.94	2.04±0.56
32 - 36	34	4.16	2.71±0.64
36 - 40	38	4.37	2.69±0.68
40 - 48	44	4.61	4.69±0.63
48 - 56	52	4.91	4.26±0.67
56 - 64	60	5.17	4.57±0.73
64 - 72	68	5.38	5.03±0.81
72 - 80	76	5.57	4.62±0.84
80 - 92	86	5.79	5.31±0.79
92 - 108	100	6.05	5.12±0.76
108 - 132	120	6.35	6.17±0.77
132 - 160	146	6.66	4.44±0.74
160 - 188	174	6.93	6.08±0.88
188 - 216	202	7.14	8.72±1.07
216 - 256	236	7.35	8.09±0.98
256 - 323	289	7.59	6.48±0.84

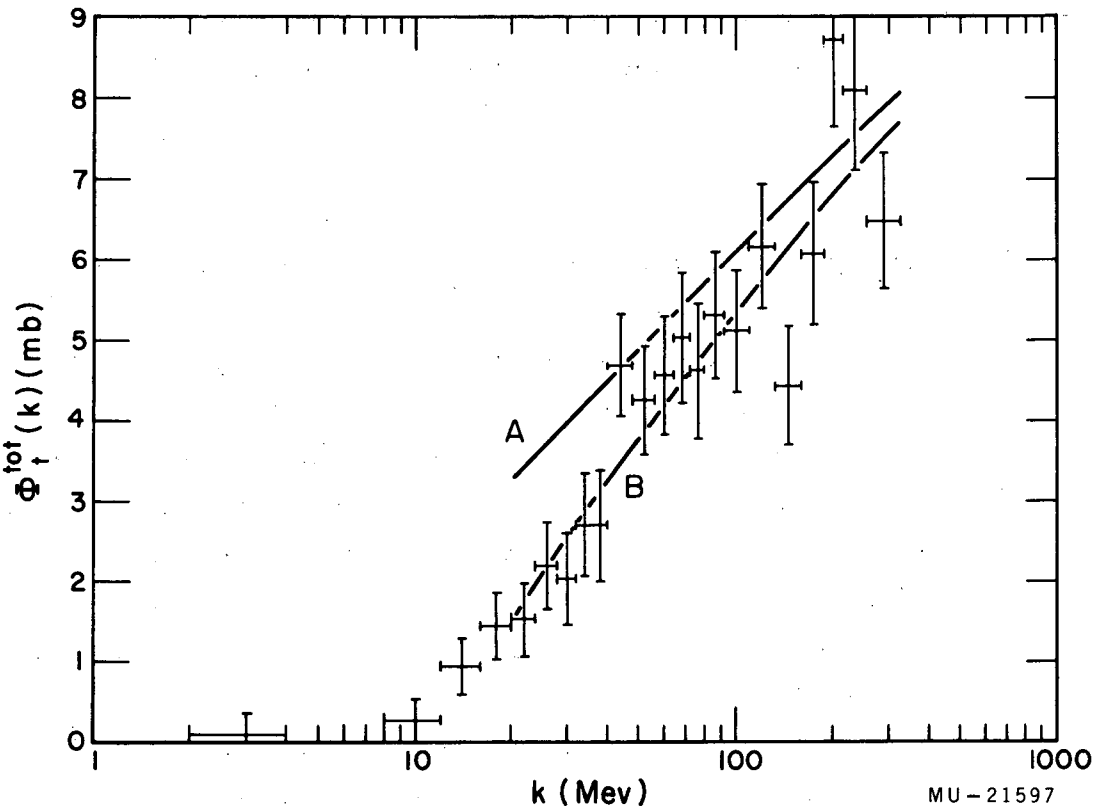

Fig. 21. The total triplet cross section, $\Phi_t^{tot}(k)$. Curve A shows the Wheeler-Lamb cross section, Φ_t^{WL}; Curve B shows the least-squares-fitted curve, discussed in Sec. VI. B. 2.

C. Partition Function

The partition function $\Phi(k, E_+)$ is a measure of the relative energy sharing between the member particles of an event. The partition value f for each pair and triplet event was calculated from the relation

$$f = (E_+ - mc^2) / (k - 2mc^2). \tag{61}$$

The quantity f is equal to the fraction of the available kinetic energy that is carried away by the positron. It is seen that the partition value is restricted to values between zero and unity, regardless of the magnitude of the positron energy or the photon energy.

Because the results of an early run of this experiment indicated the possibility of an asymmetry in the triplet partition function, it was decided to determine the pair partition function for purposes of comparison.[15] The pair partition function is known to be symmetric about the value $f = 1/2$,[28] and, at least for small recoils, one would expect the same results for triplet production.[5]

A total of 4019 pairs and 4874 triplets of all photon energies was used to obtain the experimental partition functions given in Table VIII and Figs. 22 and 23. The differential cross sections $\Phi(E_+)$ for the nine intervals of f have been normalized to an average value of unity. The larger interval from $f = 0.4$ to $f = 0.6$ was used because a significant number of events had a partition value equal to 1/2 (a result of the use of templates).

Table VIII

f Distributions for combined photon energies

f	$\Phi_t^{exp}(E_+)$	$\Phi_p^{exp}(E_+)$	$\Phi_t^{exp}(E_+)/\Phi_p^{exp}(E_+)$
0 - .1	0.784±.0401	0.677±.0410	1.158±.0919
0.1 - .2	1.143±.0484	1.094±.0522	1.045±.0667
0.2 - .3	1.096±.0474	1.174±.0541	0.933±.0589
0.3 - .4	1.032±.0460	1.140±.0533	0.906±.0585
0.4 - .6	1.036±.0326	1.095±.0369	0.946±.0436
0.6 - .7	1.032±.0460	1.035±.0508	0.997±.0661
0.7 - .8	1.030±.0460	0.975±.0493	1.056±.0712
0.8 - .9	0.989±.0450	0.926±.0480	1.068±.0737
0.9 -1.0	0.823±.0411	0.789±.0443	1.043±.0784

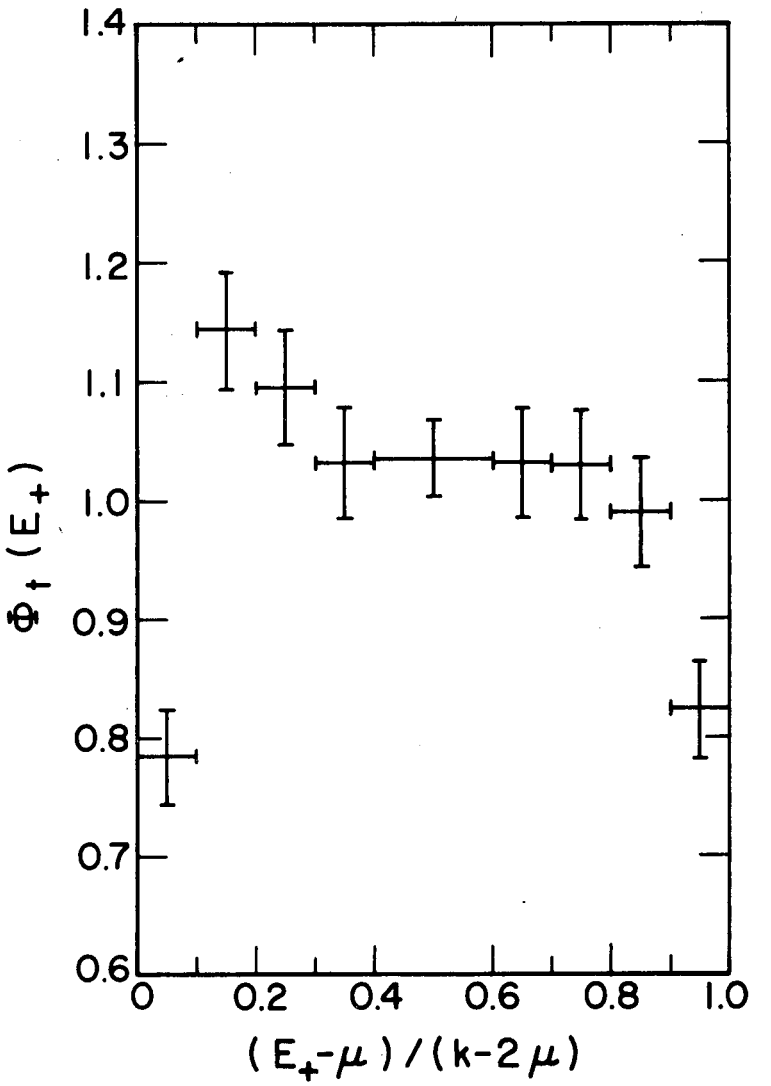

MU-21598

Fig. 22. The distribution, $\Phi_t(E_+)$, of the fraction of energy received by the positron in triplet production. All photon energies have been combined. (4874 events)

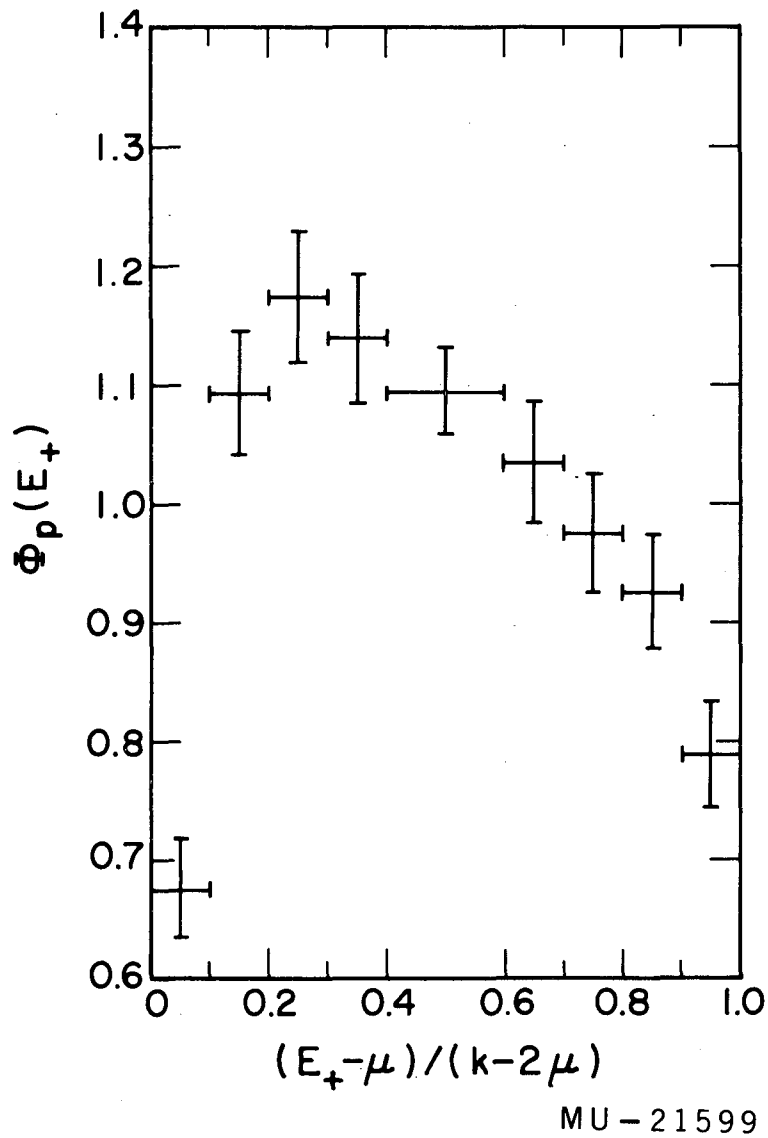

Fig. 23. The distribution, $\Phi_p(E_+)$, of the fraction of energy received by the positron in pair production. All photon energies have been combined. (4019 events)

A definite asymmetry was found in the pair and triplet partition functions. However, the cause of the asymmetry is not well understood. To examine it in more detail, the magnitude of asymmetry, A, was defined by

$$\left[A = n(f < 0.4) - n(f > 0.6)\right] / \left[n(f < 0.4) + n(f > 0.6)\right], \tag{62}$$

where $n(f < 0.4)$ and $n(f > 0.6)$ are the number of events with partition values less than 0.4 and greater than 0.6, respectively. Table IX gives the asymmetry found for various ranges of photon energy.

Table IX

Asymmetry in f distribution

k (Mev)	$A(\times 10^{-2})$(pairs)	$A(\times 10^{-2})$(triplets)
2 - 28	-9.6	-7.2
28 - 56	-7.3	-7.3
56 - 92	-2.1	0.7
92 - 160	5.9	0.2
160 - 256	18.6	13.7
256 - 323	28.1	28.6
2 - 323	4.6	2.3

The observed asymmetry was too large to be explained by the difference in multiple scattering or rate of energy loss between electron and positron. The most reasonable explanation is that it was due to the effects of turbulence in the hydrogen, caused by the expansion and recompression cycles of the chamber. If one makes the simplifying approximation that all values of f are equally probable, then a systematic error in the curvature measurements, corresponding to a momentum P_s, can be shown to produce an asymmetry given by the relation

$$A \approx 0.6\, k/P_s. \tag{63}$$

A value of P_s of the same order as the maximum measurable momentum (approx 800 Mev) would produce the observed amount of asymmetry. However, this argument does not explain the change in sign at low photon energies.

Because of the instrumental asymmetry, rather than investigate the triplet partition function alone, it was more meaningful to calculate the triplet-to-pair ratio $\Phi_t(k, E_+)/\Phi_p(k, E_+)$ as a function of the partition value. This ratio could be expected to be independent of systematic measurement errors. The ratios for six ranges of photon energy are given in Table X and Figs. 25-30. The ratio for all photon energies combined is shown in Fig. 24. The individual partition functions were normalized to an average value of unity before the ratios were calculated.

The only theoretical partition function available for comparison is that of Wheeler and Lamb,[3] which is expected to be correct in the extreme relativistic limit. Their partition function is nearly equal to that of Bethe and Heitler[28] in the energy range of this experiment because atomic screening was practically negligible. Thus, the experimental results are to be compared with a theoretical ratio which is unity for all f and k. It may be concluded that, within the accuracy of this experiment, the triplet partition function is not significantly different from the pair partition function except for a multiplicative constant.

D. Recoil Momentum Distribution

The differential recoil momentum distribution, $\Phi_t(k, P_R)$, was calculated for six ranges of photon energy by using Eq. (42). The results are given in Table XI and Figs. 31-37. There is also at each energy a ± 3.6% error due to errors other than counting statistics.

There was a total of 4874 triplets with measured photon energies (the average energy was approximately 115 Mev), and 543 triplets of which only the recoil track was measured. Because the shape of the recoil momentum distribution was practically independent of the photon energy, it was also possible to combine all energies and include the latter group of events in the results. At each energy, and in the combined results,

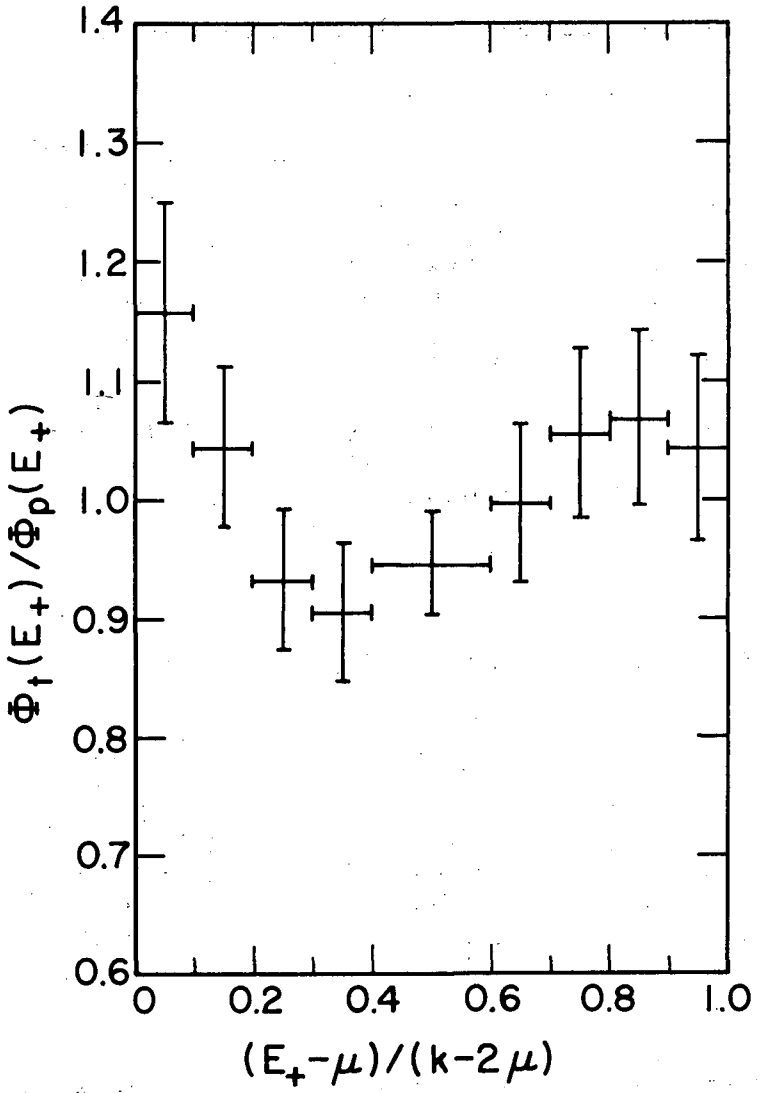

MU-21600

Fig. 24. The ratio $\Phi_t(E_+)/\Phi_p(E_+)$.

Table X

f Distribution

f	k (in Mev) 2 to 28	28 to 56	56 to 92
0 - 0.1	1.259±.323	1.068±.224	1.251±.237
0.1 - 0.2	1.166±.235	0.875±.126	1.246±.201
0.2 - 0.3	1.028±.185	0.903±.139	1.180±.185
0.3 - 0.4	0.904±.151	1.106±.173	0.827±.127
0.4 - 0.6	0.935±.120	1.083±.116	0.824±.083
0.6 - 0.7	1.167±.198	0.773±.112	1.199±.183
0.7 - 0.8	1.243±.226	0.918±.133	0.853±.134
0.8 - 0.9	0.981±.176	1.077±.158	1.213±.201
0.9 - 1.0	0.633±.123	1.209±.204	0.902±.158

f	k (in Mev) 92 to 160	160 to 256	256 to 323
0 - 0.1	1.230±.201	1.133±.179	1.122±.290
0.1 - 0.2	1.105±.151	0.946±.126	1.230±.256
0.2 - 0.3	0.918±.123	0.873±.122	0.782±.150
0.3 - 0.4	0.797±.112	0.874±.137	1.064±.202
0.4 - 0.6	0.842±.088	1.052±.111	0.957±.150
0.6 - 0.7	0.934±.135	0.950±.158	1.090±.268
0.7 - 0.8	1.121±.158	1.223±.206	1.033±.270
0.8 - 0.9	1.106±.160	1.096±.192	0.482±.157
0.9 - 1.0	1.319±.212	0.925±.166	1.767±.569

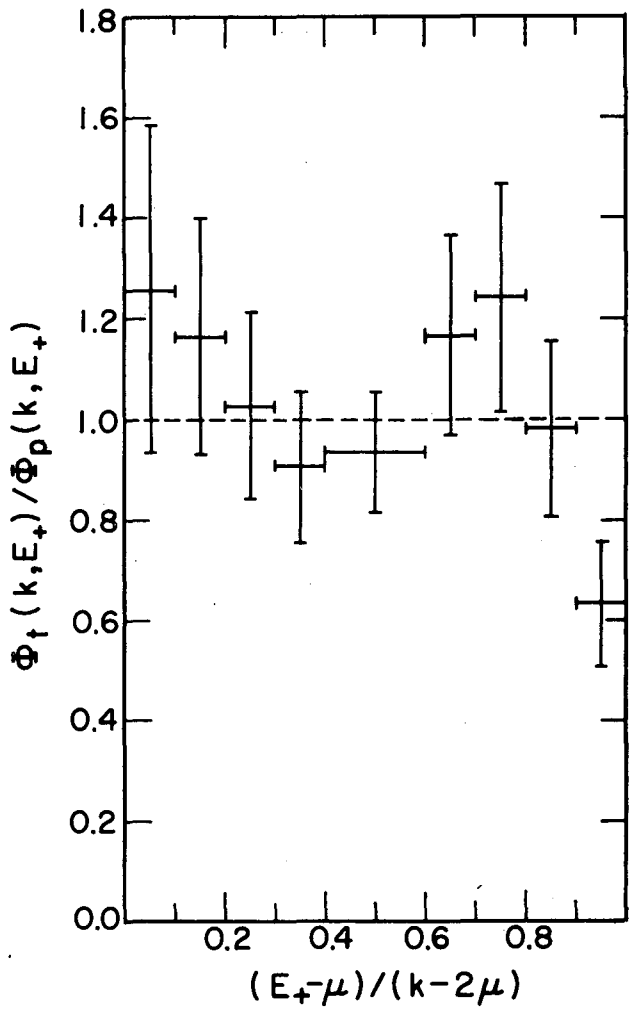

MU-21601

Fig. 25. The ratio $\Phi_t(k, E_+)/\Phi_p(k, E_+)$ for $2 \leqslant k \leqslant 28$ Mev. The dashed line shows the ratio of the normalized Wheeler-Lamb partition function to the normalized Bethe-Heitler partition function at the peak energy of the interval.

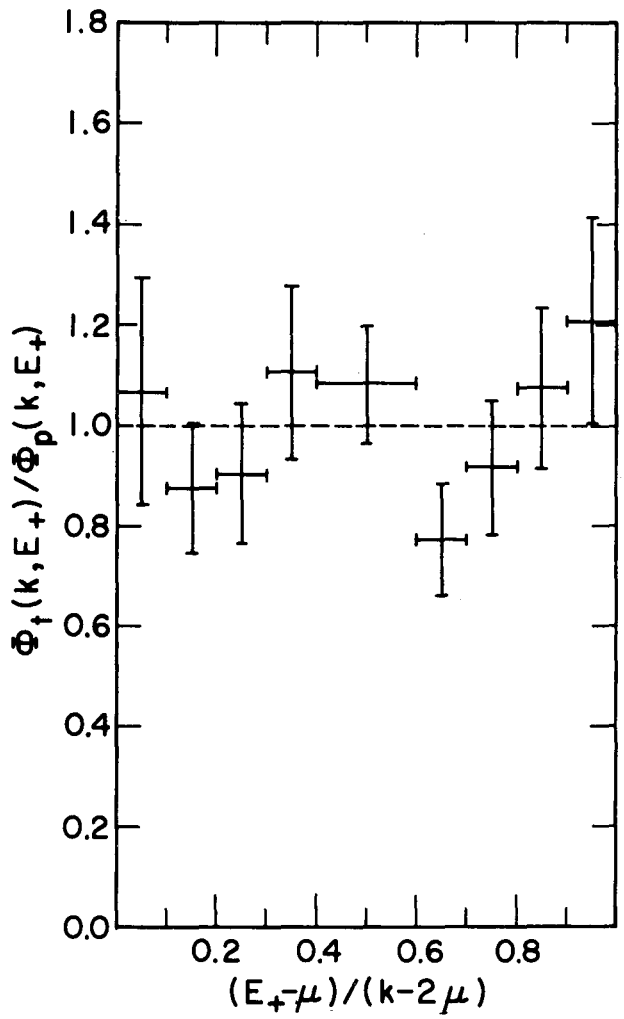

MU-21602

Fig. 26. The ratio $\Phi_t(k, E_+)/\Phi_p(k, E_+)$ for $28 \leqslant k \leqslant 56$ Mev. The dashed line shows the ratio of the normalized Wheeler-Lamb partition function to the normalized Bethe-Heitler partition function at the peak energy of the interval.

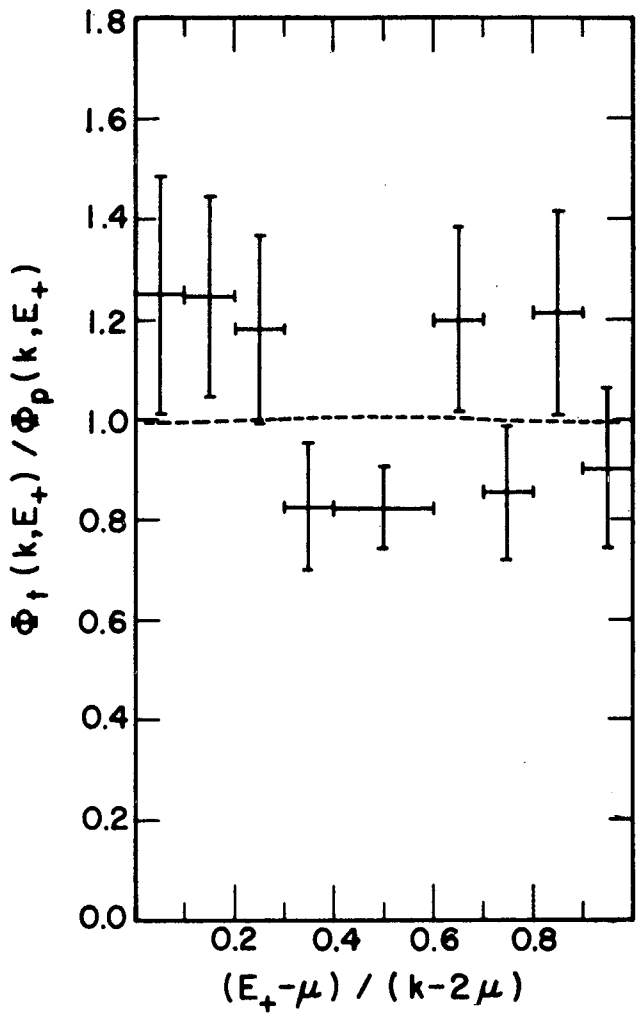

MU-21603

Fig. 27. The ratio $\Phi_t(k, E_+)/\Phi_p(k, E_+)$ for $56 \leqslant k \leqslant 92$ Mev. The dashed line shows the ratio of the normalized Wheeler-Lamb partition function to the normalized Bethe-Heitler partition function at the peak energy of the interval.

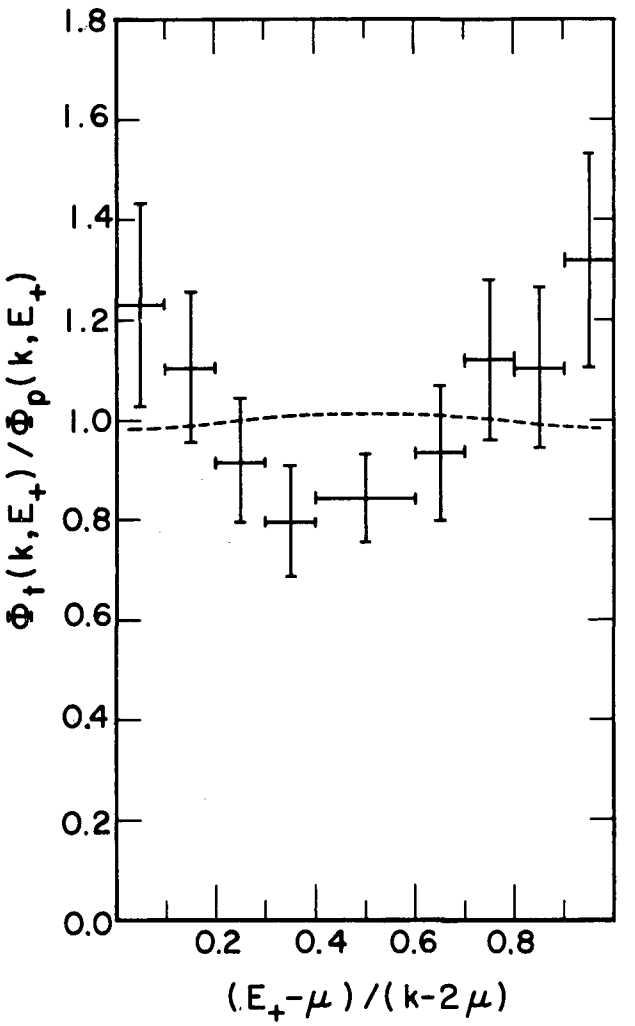

MU-21604

Fig. 28. The ratio $\Phi_t(k, E_+)/\Phi_p(k, E_+)$ for $92 \leqslant k \leqslant 160$ Mev. The dashed line shows the ratio of the normalized Wheeler-Lamb partition function to the normalized Bethe-Heitler partition function at the peak energy of the interval.

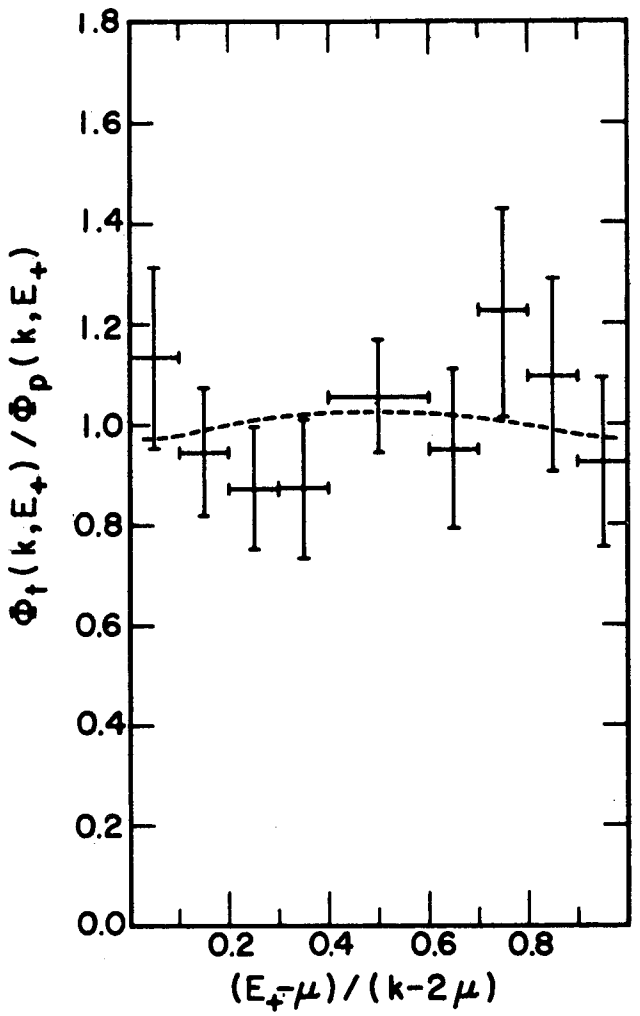

MU-21605

Fig. 29. The ratio $\Phi_t(k, E_+)/\Phi_p(k, E_+)$ for $160 \leqslant k \leqslant 256$ Mev. The dashed line shows the ratio of the normalized Wheeler-Lamb partition function to the normalized Bethe-Heitler partition function at the peak energy of the interval.

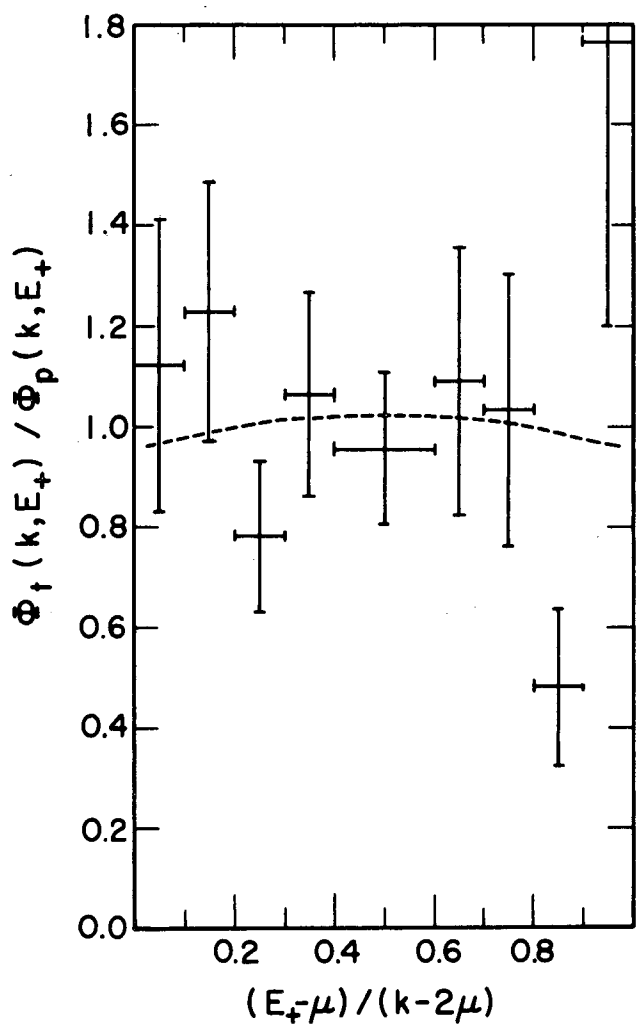

MU-21606

Fig. 30. The ratio $\Phi_t(k, E_+)/\Phi_p(k, E_+)$ for $256 \leqslant k \leqslant 323$ Mev. The dashed line shows the ratio of the normalized Wheeler-Lamb partition function to the normalized Bethe-Heitler partition function at the peak energy of the interval.

Table XI

$\phi_t(k, P_R)$ (in μb/Mev/c) vs. k (in Mev) and P_R (in Mev/c)

P_R (Mev/c	k (in Mev) 2 - 28	28 - 56	56 - 92	92 - 160	160 - 256	256 - 323	2 - 323
0.15- 0.22	757±114	1981±229	2417±300	2588±309	3359±404	3218±588	1941±98.6
0.22- 0.32	1264±123	2699±223	3722±311	4503±341	3543±347	4505±582	2882±100
0.32- 0.46	1135±98.8	2324±175	2659±222	3327±248	3480±291	3700±445	2342±76.5
0.46- 0.68	573±56.4	1101±96.2	1219±120	1835±147	2091±180	1945±258	1231±44.6
0.68- 1.0	367±37.5	659±61.7	944±88.5	1124±95.3	969±102	774±135	727±28.3
1.00- 1.47	227±24.6	445±41.8	554±55.4	600±57.5	623±67.2	703±106	450±18.4
1.47- 2.15	95.9±13.3	182±22.3	249±30.9	282±32.7	396±44.5	309±58.4	212±10.5
2.15- 3.16	37.2± 6.91	128±15.3	147±19.5	195±22.3	169±23.9	164±34.9	119± 6.50
3.16- 4.64	21.0± 4.47	52.5± 8.10	61.6±10.4	82.2±12.0	53.0±11.0	40.6±22.0	48.0± 3.45
4.64- 6.81	5.07± 1.91	15.3± 3.62	43.2± 7.20	38.2± 6.75	34.5± 7.37	20.8± 8.48	21.5± 1.94
6.81-10.0	1.20± 0.85	9.27± 2.32	12.2± 3.16	13.0± 3.25	19.2± 4.53	21.2± 7.06	10.2± 1.13
10.0 -14.7		2.75± 1.04	3.32± 1.36	8.81± 2.20	4.35± 1.78	3.19± 2.26	3.81± 0.59
14.7 -21.5		0.54± 0.38	2.68± 1.01	3.04± 1.08	2.51± 1.12	4.20± 1.88	2.21± 0.39
21.5 -31.6			0.52± 0.36	1.02± 0.51	1.35± 0.67	1.49± 1.05	0.67± 0.18
31.6 -46.4			0.18± 0.18	0.52± 0.30	0.69± 0.40	1.01± 0.72	0.37± 0.12
46.4 -68.1					1.47± 0.56		0.27± 0.10
No. events:	677	977	894	1104	845	377	5417

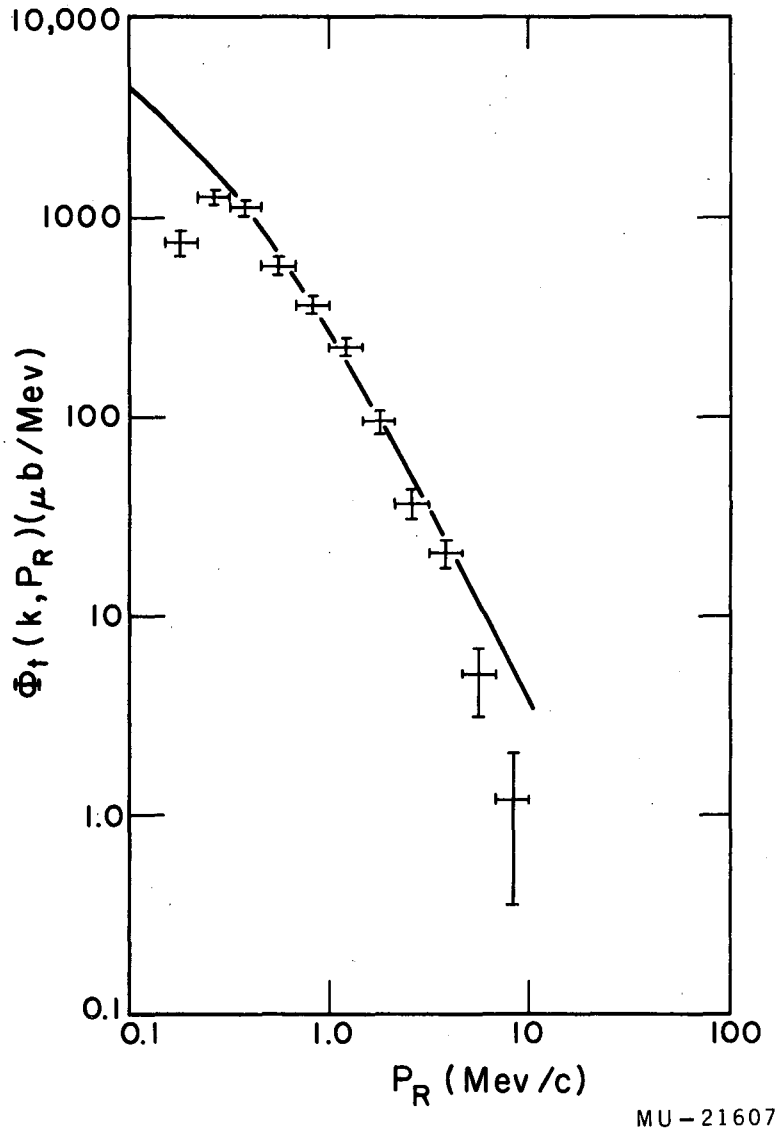

Fig. 31. The differential cross section, $\Phi_t(k, P_R)$, plotted versus the momentum of the recoil electron, P_R, for $2 \leqslant k \leqslant 28$ Mev. (677 events.)

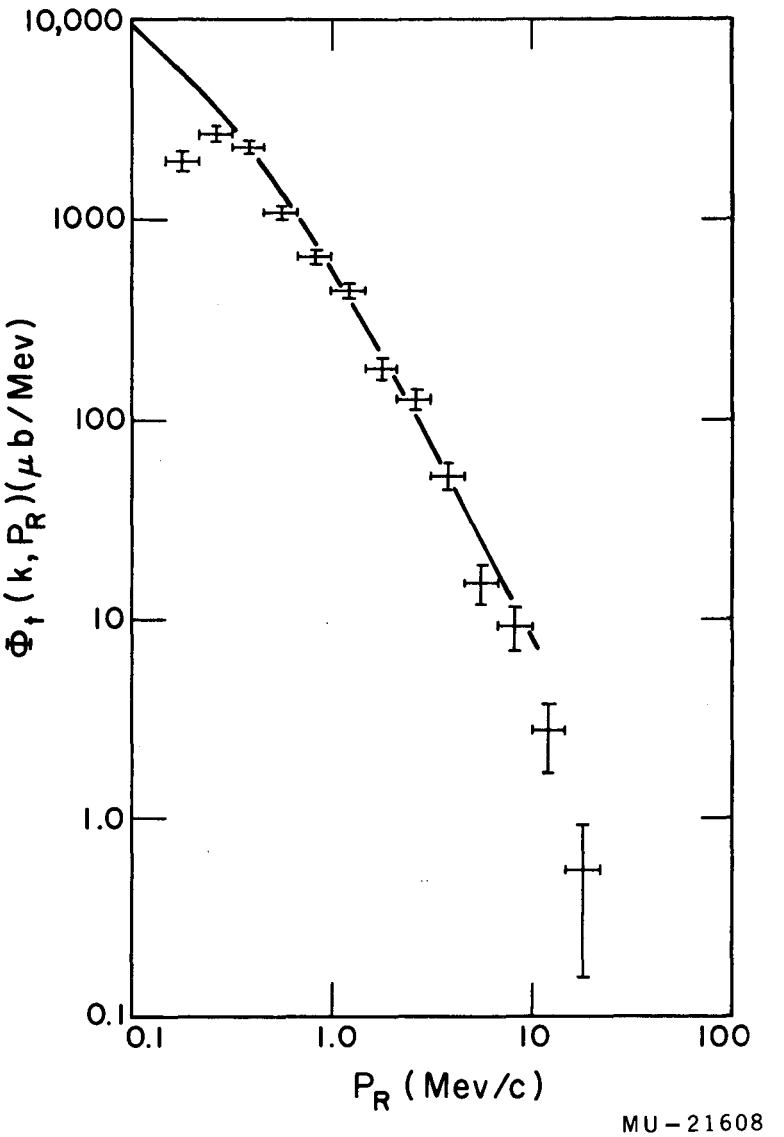

Fig. 32. The differential cross section, $\Phi_t(k, P_R)$, plotted versus the momentum of the recoil electron, P_R, for $28 \leq k \leq 56$ Mev. (977 events.) The curve shown is that calculated by Suh and Bethe for a photon energy of 100 Mev. It has been arbitrarily normalized to agree with the data at 1.0 Mev/c.

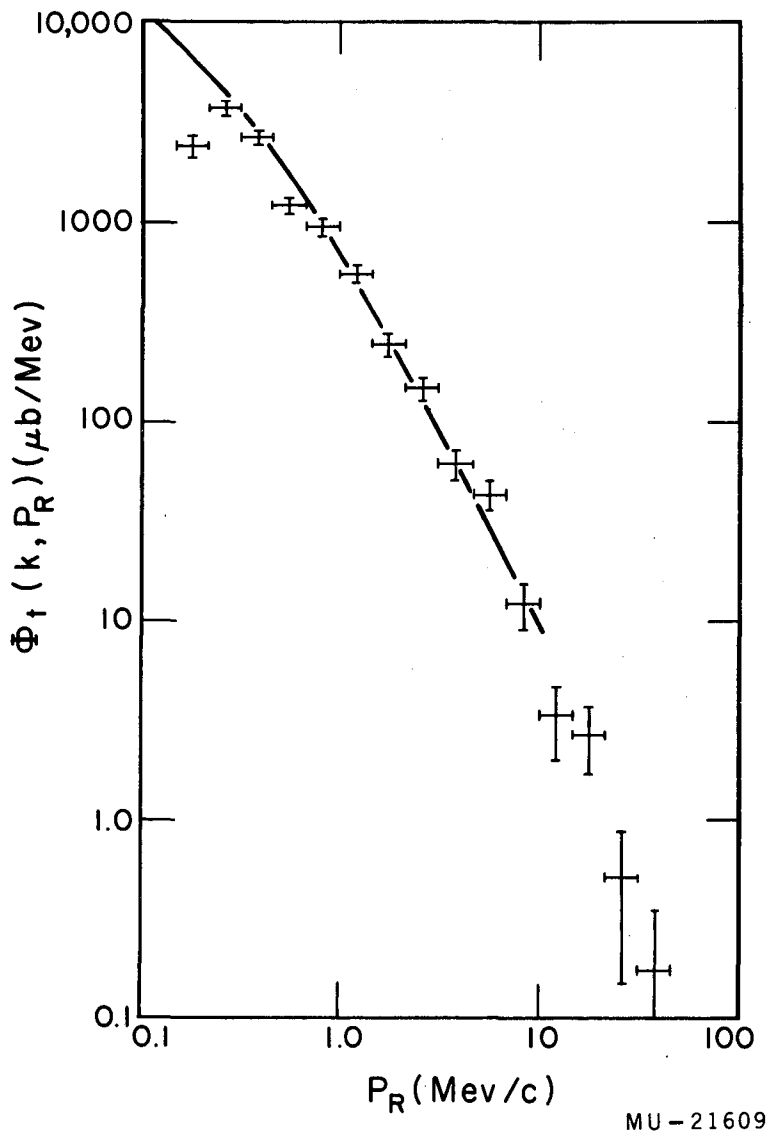

Fig. 33. The differential cross section, $\Phi_t(k, P_R)$, plotted versus the momentum of the recoil electron, P_R, for $56 \leqslant k \leqslant 92$ Mev. (894 events.) The curve shown is that calculated by Suh and Bethe for a photon energy of 100 Mev. It has been arbitrarily normalized to agree with the data at 1.0 Mev/c.

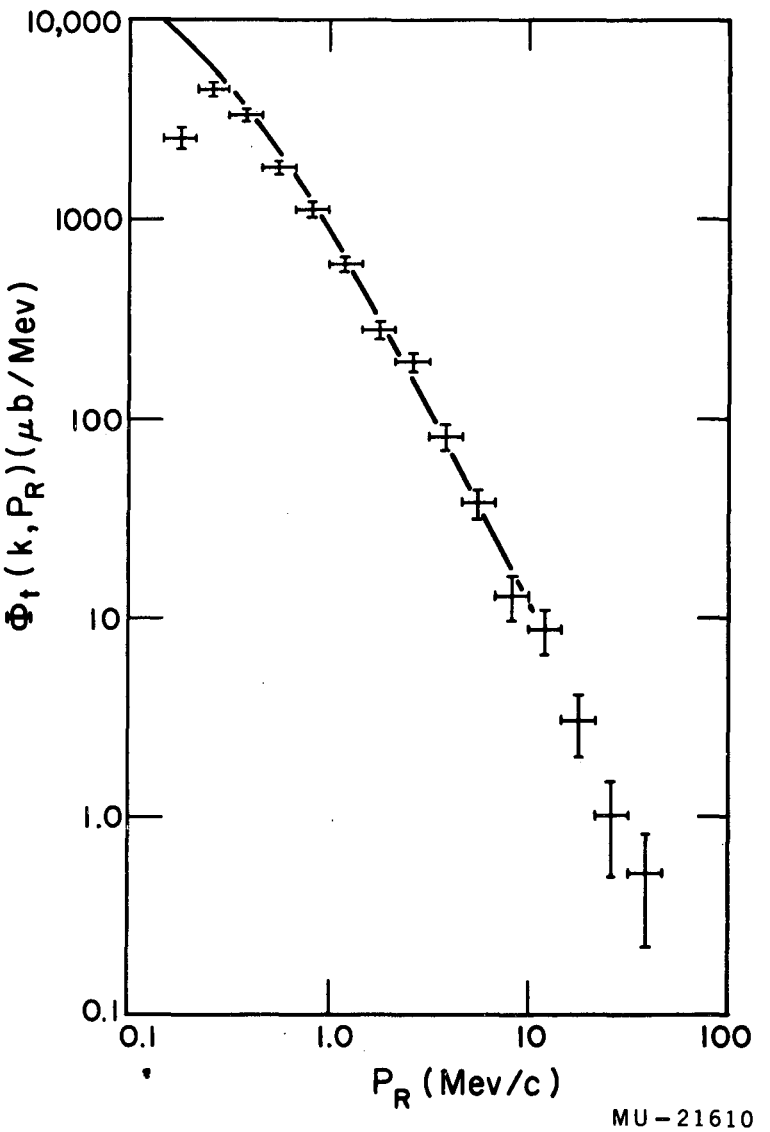

Fig. 34. The differential cross section, $\Phi_t(k, P_R)$, plotted versus the momentum of the recoil electron, P_R, for $92 \leq k \leq 160$ Mev. (1104 events.) The curve shown is that calculated by Suh and Bethe for a photon energy of 100 Mev. It has been arbitrarily normalized to agree with the data at 1.0 Mev/c.

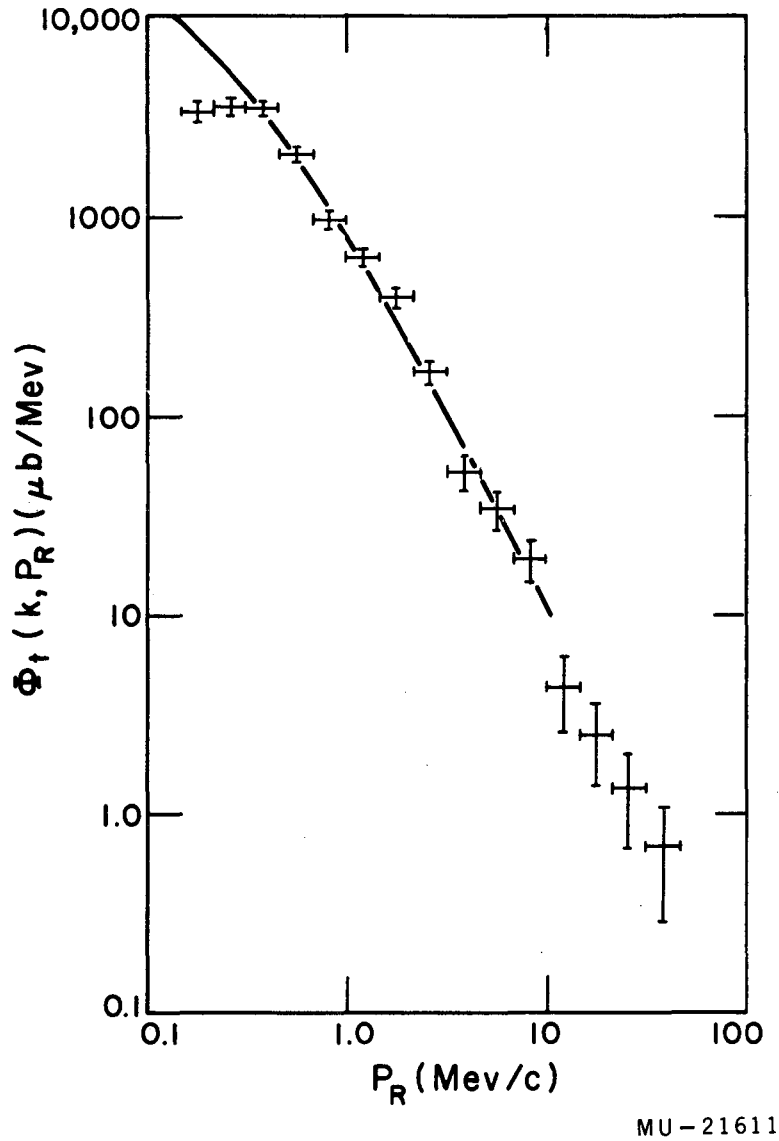

Fig. 35. The differential cross section, $\Phi_t(k, P_R)$, plotted versus the momentum of the recoil electron, P_R, for $160 \leq k \leq$ Mev. (845 events.) The curve shown is that calculated by Suh and Bethe for a photon energy of 100 Mev. It has been arbitrarily normalized to agree with the data at 1.0 Mev/c.

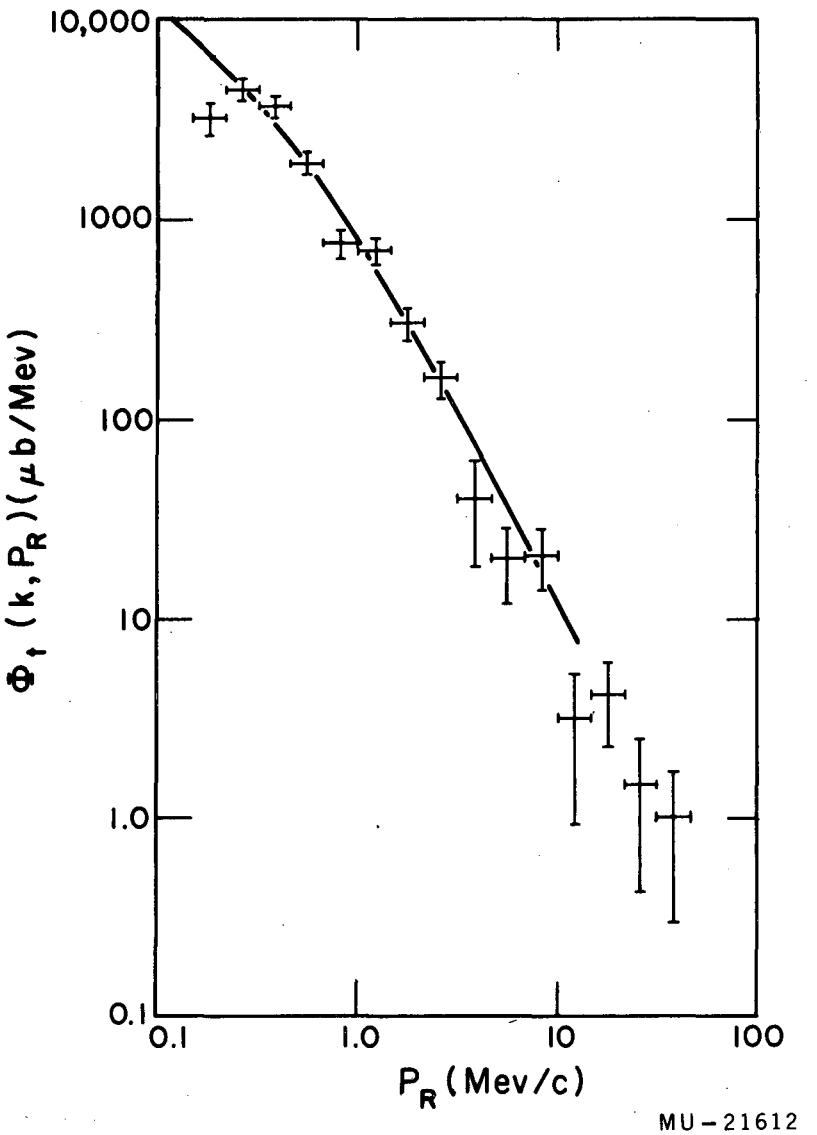

Fig. 36. The differential cross section, $\Phi_t(k, P_R)$, plotted versus the momentum of the recoil electron, P_R, for $256 \leq k \leq 323$ Mev. (377 events.) The curve shown is that calculated by Suh and Bethe for a photon energy of 100 Mev. It has been arbitrarily normalized to agree with the data at 1.0 Mev/c.

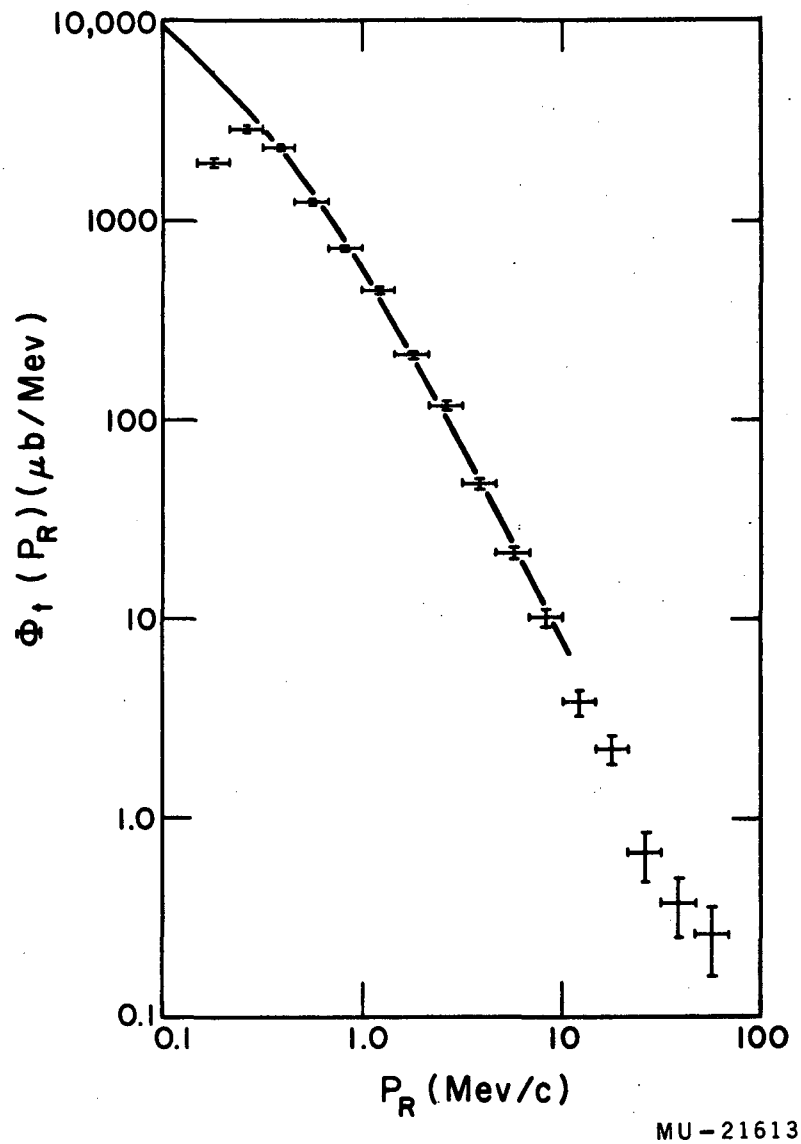

Fig. 37. The differential cross section, $\Phi_t(P_R)$, plotted versus the momentum of the recoil electron, P_R. All photon energies have been combined. (5417 events.) The curve shown is that calculated by Suh and Bethe for a photon energy of 100 Mev. It has been arbitrarily normalized to agree with the data at 1.0 Mev/c.

it was necessary to take into account the fact that the low-energy photons could not contribute to the larger recoil-momentum bins. Also, since accurate monitor data were available for only 3445 of the events, it was necessary to adjust the monitor results (Table V) by multiplying by the appropriate ratio of the increased number of events.

The delta-ray correction to the experimental distribution in momentum was calculated from scattering theory[39] for the combined results. The percentage correction was significant for three ranges of P_R and is given in Table XII.

Table XII

δ-Ray correction to recoil momentum distribution

P_R (Mev/c)	$(d\Phi/dP_R)_d/\Phi_t$ (all k, P_R)
0.32 - 0.46	-9.1%
0.46 - 0.68	-5.8
0.68 - 1.0	-3.2

There is a 25% uncertainty in the magnitude of the correction which was due to the choice of d = 2±.5 mm (see Sec. V. D. 2).

The theoretical recoil momentum distribution of Suh and Bethe is valid for photon energies greater than 100 Mev.[5] Their curve, for k = 100 Mev, is shown in each figure along with the experimental values. The theoretical curve has been arbitrarily normalized to fit the experimental results at P_R = 1 Mev/c.

As explained in Sec. V. D. 2, the two lowest recoil momentum bins are not expected to agree with the theory because of the uncertain detection efficiency below 0.32 Mev/c.

Agreement between experiment and theory is very good in the photon energy ranges above 92 Mev and in the combined results, whereas below that energy the theoretical values can be seen to be slightly too high in the region of large recoil momentum. The theory must be considered to be approximate in the region of large recoil momentum.

E. Recoil Angular Distribution

The measurements and calculations necessary to obtain the polar angle θ_R and the azimuthal angle ϕ_R of the recoil electron were made as described in Sec. IV. D.2.c and Sec. IV. C.2, respectively. The polar angle was the angle between the direction of the recoil and the direction of the incident photon (z axis), while the azimuthal angle was zero when the direction of the recoil was perpendicular to the optical axis (y axis).

A plot of the distribution in azimuthal angle of the recoils showed that all angles were equally populated. This result indicates that the scanning efficiency was independent of the orientation of the track with respect to the optical axis.

The number of events for 5-degree intervals of θ_R is given in Table XIII and Fig. 38. All photon energies have been combined because the angular distribution was nearly independent of that quantity. The triangular shape of the distribution, with a peak at approximately 50 degrees, is quite striking.

According to the kinematic argument given in Sec. V. B, one expects the small recoil angles to correspond to large momenta and the large recoil angles to correspond to small momenta. That this is approximately true is shown by Table XIV, which lists the number of events found in the various intervals of θ_R and P_R. At the position of the peak in the angular distribution, it is seen that the principal contribution was made by recoils of approximately 1 Mev/c momentum.

Table XIII

Number of events vs. θ_R	
θ_R	No. of events
0 - 5	7
5 - 10	17
10 - 15	62
15 - 20	82
20 - 25	133
25 - 30	167
30 - 35	209
35 - 40	239
40 - 45	244
45 - 50	281
50 - 55	334
55 - 60	296
60 - 65	245
65 - 70	193
70 - 75	193
75 - 80	159
80 - 85	109
85 - 90	84
90 - 95	50
95 - 100	8
100 - 110	10
110 - 120	5

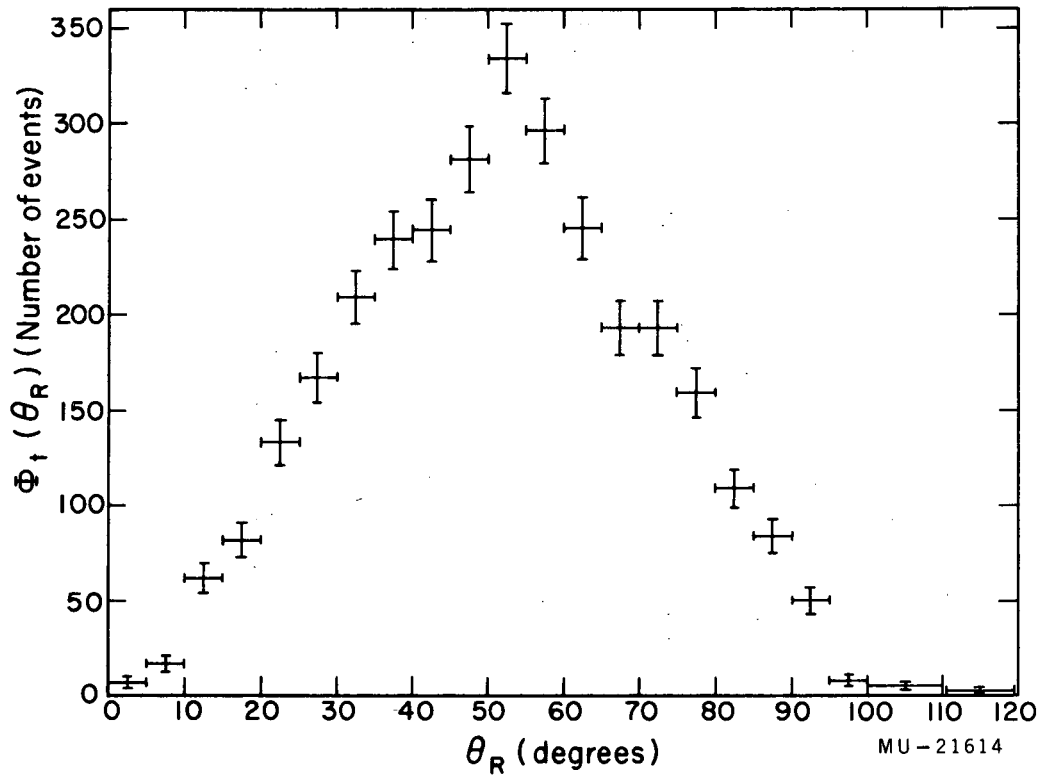

Fig. 38. The angular distribution of the recoil electron. Numbers of events are plotted versus the polar angle θ_R.

Table XIV

Distribution of events with respect to angle and momentum

P_R (Mev/c	θ_R (deg) 0-10	10-20	20-30	30-40	40-50	50-60	60-70	70-80	80-90	90-100	100-110
0.15 - 0.22	1		4	6	7	10	12	15	5	1	1
0.22 - 0.32		5	7	14	19	37	49	34	28	13	3
0.32 - 0.46		8	15	27	56	93	92	105	80	30	6
0.46 - 0.68	1	7	15	43	68	130	103	95	52	9	
0.68 - 1.0		4	18	33	84	145	102	61	10	2	
1.00 - 1.47	1	7	22	62	119	134	53	15	7	2	
1.47 - 2.15	2	5	25	91	93	52	17	13	5		
2.15 - 3.16	4	17	51	88	60	16	7	4	5	1	
3.16 - 4.64	1	16	53	56	13	7	2	5			
4.64 - 6.81		18	59	16	3	4		3	1		
6.81 -10.0	1	24	24	9	1			1			
10.0 -14.7	3	12	4	2		1	1	1			
14.7 -21.5	6	12	2		1						
21.5 -31.6	2	7			1	1					
31.6 -46.4	2	2	1								
46.4 -68.1				1							

The position of the peak and the shape of the distribution are believed to have been strongly influenced by the value of the minimum detectable momentum, especially at the larger angles. Unfortunately there is no theoretical angular distribution with which the results may be compared.

F. Multiple Pair Production

There was a total of approximately 24,000 pairs and triplets in the film scanned for this experiment. Since there are two extra vertices in the lowest-order Feynman diagrams for double pair production, one would expect the cross section to be reduced by a factor of $(1/137)^2$, relative to the sum of the pair and triplet cross sections. Thus, one would "expect" to find one double pair in this experiment.

Several events were found which, after careful inspection, turned out to be ordinary pairs with origins very nearly in coincidence. There were also two events which could have been either double pairs or accidental coincidences of ordinary pairs (actually, a pair and a triplet in one case). Positive identification was uncertain because the tracks remained merged together near the origin.

The results indicated that an accidental coincidence was more probable than a real double pair. Consequently, it was concluded that this experiment contained no definite evidence for double pair production in hydrogen.

G. Summary

Electron-positron pairs and triplets were produced by a 323-Mev hardened bremsstrahlung beam in the Alvarez 4-inch-diameter liquid hydrogen bubble chamber. Measurements and analysis were performed on 5417 triplets and 4019 pairs of the approximately 24,000 events photographed. The results may be summarized as follows:

(a) The experimental triplet-to-pair ratio was equal to 0.291 ± 0.0097. It was approximately constant below 100 Mev, but decreased above that value. The decrease was due to a leveling off of the observed triplet cross section.

(b) The total pair-plus-triplet cross section was consistent with the upper and lower limits expected from the theory. The total triplet cross section was between the results of Borsellino[4] and Votruba[6] in the region above 40 Mev. The results are statistically consistent with the theory of Borsellino.

(c) If the contribution of the exchange terms and $\gamma - \bar{e}$ interaction is taken to be of the form $-B(\alpha r_0^2)(mc^2/k)\ln(2k/mc^2)$, then B is 2.4 ± 7.4.

(d) The partition function agreed with that of Wheeler and Lamb.[3]

(e) The recoil momentum distribution agreed substantially with that of Suh and Bethe.[5] However, the theoretical values are slightly too large in the region of large recoil momentum.

(f) The recoil angular distribution is triangular in shape, with a peak at approximately 50 degrees. Large recoil momenta (greater than 1 Mev/c) are predominantly on the small-angle side of the peak.

(g) No event was found which could be positively identified as a double pair. Approximately one event was expected.

Use of the lithium hydride column to remove low-energy quanta from the beam was essential to reduce the background of Compton electrons in the chamber. The thin entrance window was also important to the reduction of background tracks.

ACKNOWLEDGMENTS

The helpful advice and assistance of Dr. Robert W. Kenney during this experiment is sincerely appreciated. I am indebted to Professor A. C. Helmholz for his guidance and encouragement throughout my graduate work. Special mention is also due Mr. William Swanson, who collaborated closely throughout the experimental program. Dr. John Anderson, Dr. Thomas Jenkins, and Dr. Charles McDonald were very helpful in an early phase of the experiment.

There was complete cooperation and helpful assistance from the synchrotron crew under the direction of Mr. Rudin Johnson.

Thanks are due to Professor Luis Alvarez for the use of the bubble chamber and scanning equipment. Mr. Arnold Schwemin and Mr. Douglas Parmentier, Jr., provided valuable help with the chamber in earlier runs, Mr. Clyde Brown modified the chamber for us, and Mr. Donald McPherson gave us much help operating the chamber, as did many other members of our group.

Grateful acknowledgment goes to Dr. Graham Conroy, Mr. Lloyd Fisher, Mr. Gordon Hamilton, Mr. Donald Thompson, and Mr. Terry Zaccone for help in carrying out the arduous film analysis.

I would also like to express my appreciation to the many supporting groups of the Lawrence Radiation Laboratory whose efforts allowed the work to proceed smoothly to a conclusion, but whose members are too numerous to mention here.

This work was performed under the auspices of the U. S. Atomic Energy Commission.

REFERENCES

1. H. A. Bethe and W. Heitler, Proc. Roy. Soc. (London) A146, 83 (1934); H. A. Bethe, Proc. Cambridge Phil. Soc. 30, 524 (1934).
2. F. Perrin, Compt. rend. 197, 1100 (1933).
3. J. A. Wheeler and W. E. Lamb, Phys. Rev. 55, 858 (1939); Phys. Rev. 101, 1836 (1956).
4. A. Borsellino, Helv. Phys. Acta 20, 136 (1947); Nuovo cimento 4, 112 (1947); Rev. univ. nacl. Tucumán A6, 7 (1947).
5. K. S. Suh and H. A. Bethe, Bull. Am. Phys. Soc. (II) 4, 13 (1959); Phys. Rev. 115, 672 (1959).
6. Vaclav Votruba, Bull. intern. acad. Tcheque sci. 49, 19 (1948); Phys. Rev. 73, 1468 (1948).
7. J. Joseph and F. Rohrlich, Revs. Modern Phys. 30, 354 (1958). This paper contains a complete list of references to previous experimental and theoretical work on triplet production.
8. J. M. Jauch and F. Rohrlich, Theory of Photons and Electrons (Addison-Wesley Publishing Co., Inc., Cambridge, 1955).
9. K. Mitchell, Phil. Mag. 40, 351 (1949).
10. John D. Anderson, Robert W. Kenney, and Charles A. McDonald, Jr., Phys. Rev. 102, 1626 (1956); John D. Anderson, Robert W. Kenney, Charles A. McDonald, Jr., and Richard F. Post, Phys. Rev. 102, 1632 (1956).
11. J. Moffatt, J. J. Thresher, G. C. Weeks, and R. Wilson, Proc. Roy. Soc. (London) (A) 244, 245 (1958); J. Moffatt and G. C. Weeks, Proc. Phys. Soc. (London) 73, 114 (1959).
12. E. Malamud, Phys. Rev. 115, 687 (1959). This paper also contains many references relating to absorption measurements in other elements.
13. Rosemary T. McGinnies, "X-Ray Attenuation Coefficients from 10 Kev to 100 Mev," National Bureau of Standards, Supplement to NBS Circular 583, Oct. 30, 1959.

14. E. L. Hart, G. Cocconi, V. T. Cocconi, and J. M. Sellen, Phys. Rev. 115, 678 (1959).

15. The results from an early run of this experiment were reported as follows: John D. Anderson, Duane C. Gates, Thomas L. Jenkins, Robert W. Kenney, Charles A. McDonald, Jr., and William P. Swanson, Bull. Am. Phys. Soc. (II) 1, 376 (1956), abstract B5; Proceedings of the Second United Nations International Conference on the Peaceful Uses of Atomic Energy, Geneva, 1958 (United Nations, Geneva, 1958) 30, 250.

16. Douglas Parmentier and Arnold J. Schwemin, Rev. Sci. Instr. 26, 954 (1955).

17. Harry Cline Dittler and Thomas Frank Gerecke, "Liquid Hydrogen Bubble Chamber" (Master's Thesis), University of California Radiation Laboratory Report UCRL-2985, May 10, 1955.

18. Additional references on bubble chambers may be found in the following publications: Betty K. Ogden, "Bubble Chambers. A Bibliography," CERN Scientific Information Service, CERN Bibl. 2, 1959; Pierre Amiot and Betty K. Ogden, "Index to the UCRL Engineering Notes on Hydrogen Bubble Chambers and Data Analysis," CERN Scientific Information Service, CERN Bibl. 3, 1959.

19. The operation of the Alvarez 4-inch bubble chamber has also been described by Duane C. Gates, Robert W. Kenney, Donald A. McPherson, and William P. Swanson, Rev. Sci. Instr. 31, 565 (1960).

20. A description of this ionization chamber has been given in a Cornell University progress report: Corson, DeWire, McDaniel, and Wilson, "The Cornell 300-Mev Synchrotron," Office of Naval Research Report, July, 1953.

21. F. L. Loeffler, T. R. Palfrey, and G. W. Tautfest, Nuclear Instr. and Methods 5, 50 (1959).

22. J. W. DeWire (Laboratory of Nuclear Studies, Cornell University), private communication.

23. Robert W. Kenney, Absolute Photon Attenuation Cross Section for Non-Pair Processes in Beryllium at 300 Mev (Thesis), University of California Radiation Laboratory Report UCRL-1654, Feb. 1, 1952.

24. Charles Alexander McDonald, Jr., Pair Production in the Field of Orbital Electrons by a Total-Absorption Method at 300 Mev (Thesis), University of California Radiation Laboratory Report UCRL-2595, June 2, 1954.

25. Leland Kuns Neher, Meson Production by High-Energy Neutrons (Thesis), University of California Radiation Laboratory Report UCRL-2191, April 23, 1953.

26. Robert W. Kenney (Lawrence Radiation Laboratory), private communication.

27. W. Heitler, The Quantum Theory of Radiation, 3rd ed. (Oxford University Press, New York, 1954), p. 221, Eq. (45).

28. Hans A. Bethe and Julius Ashkin, "Passage of Radiations Through Matter," in Experimental Nuclear Physics, E. Segre, ed., Vol. I (John Wiley and Sons, Inc., New York, 1953), p. 252.

29. W. Heitler, op. cit., p. 254, Eq. (35).

30. Gladys White Grodstein, "X-Ray Attenuation Coefficients from 10 Kev to 100 Mev," National Bureau of Standards, NBS Circular 583, April 30, 1957. Atomic cross sections for energies less than 80 Mev were taken from this publication.

31. L. I. Schiff, Phys. Rev. 83, 252 (1951), Eq. (3).

32. W. Heitler, op. cit., p. 244.

33. E. Hisdal, Phys. Rev. 105, 1821 (1957), Table III.

34. H. A. Bethe and L. C. Maximon, Phys. Rev. 93, 768 (1954).

35. Wilson M. Powell, Walter Hartsough, and Milton Hill, Phys. Rev. 81, 213 (1951), Table II, column 2.

36. Richard Wilson, Proc. Phys. Soc. (London) A66, 638 (1953).

37. Walter H. Barkas and Arthur H. Rosenfeld, Data for Elementary-Particle Physics, University of California Radiation Laboratory Report, UCRL-8030, Mar. 20, 1958.

38. A. Borsellino, Phys. Rev. 89, 1023 (1953).

39. Ann T. Nelms, Energy Loss and Range of Electrons and Positrons, National Bureau of Standards, Supplement to NBS Circular 577, July 30, 1958.

40. W. Heitler, op. cit., p. 241, Eq. (31).

41. Leonard Reed and Robert Tripp, "Density of Hydrogen at Operation Conditions of 15-in. B.C.," University of California Radiation Laboratory Engineering Note No. 4320-01M2/UCID 506, October 30, 1958.

This report was prepared as an account of Government sponsored work. Neither the United States, nor the Commission, nor any person acting on behalf of the Commission:

A. Makes any warranty or representation, expressed or implied, with respect to the accuracy, completeness, or usefulness of the information contained in this report, or that the use of any information, apparatus, method, or process disclosed in this report may not infringe privately owned rights; or

B. Assumes any liabilities with respect to the use of, or for damages resulting from the use of any information, apparatus, method, or process disclosed in this report.

As used in the above, "person acting on behalf of the Commission" includes any employee or contractor of the Commission, or employee of such contractor, to the extent that such employee or contractor of the Commission, or employee of such contractor prepares, disseminates, or provides access to, any information pursuant to his employment or contract with the Commission, or his employment with such contractor.